Improvements in the registration of multimodal medical imaging: application to intensity inhomogeneity and partial volume corrections.

Thesis to obtain a PhD degree in Biomedical Engineering, RD/99

Universitat Politècnica de Catalunya

Author: Xavier Jiménez
e-mail: javijimenezg@gmail.com

Thesis advisor: PhD. Juan Domingo Gispert
Neuroimaging Unit, Fundació Pasqual Maragall
Carrer Wellington, 30
08005 Barcelona
e-mail: jdgispert@fpmaragall.org

Thesis advisor: PhD. Ferran Marques
Dept. Teoria Senyal i Comunicacions
Universitat Politècnica de Catalunya (UPC)
Edifici D5, Despatx 111
Carrer Jordi Girona, 1-3
08034 Barcelona
e-mail: ferran.marques@upc.edu

Barcelona, 2016

UNIVERSITAT POLITÈCNICA DE CATALUNYA
BARCELONATECH
Escola de Doctorat

Curs acadèmic: 2016-2017

Acta de qualificació de tesi doctoral

Nom i cognoms
XAVIER JIMENEZ GONZALEZ

Programa de doctorat
ENGINEYERIA BIOMEDICA

Unitat estructural responsable del programa
ENGINYERIA DE SISTEMES, AUTOMATICA I INFORMATICA INDUSTRIAL

Resolució del Tribunal

Reunit el Tribunal designat a l'efecte, el doctorand / la doctoranda exposa el tema de la seva tesi doctoral titulada

_____

_____.

Acabada la lectura i després de donar resposta a les qüestions formulades pels membres titulars del tribunal, aquest atorga la qualificació:

☐ NO APTE ☐ APROVAT ☐ NOTABLE ☐ EXCEL·LENT

(Nom, cognoms i signatura)	(Nom, cognoms i signatura)	
President/a	Secretari/ària	
(Nom, cognoms i signatura)	(Nom, cognoms i signatura)	(Nom, cognoms i signatura)
Vocal	Vocal	Vocal

_____, _____ d'/de _____ de _____

El resultat de l'escrutini dels vots emesos pels membres titulars del tribunal, efectuat per la Comissió Permanent de l'Escola de Doctorat, atorga la MENCIÓ CUM LAUDE:

☐ SÍ ☐ NO

(Nom, cognoms i signatura)	(Nom, cognoms i signatura)
President/a de la Comissió Permanent de l'Escola de Doctorat	Secretari/ària de la Comissió Permanent de l'Escola de Doctorat

Barcelona, _____ d'/de _____ de _____

Summary

Alignment or registration of medical images has a relevant role on clinical diagnostic and treatment decisions as well as in research settings. With the advent of new technologies for multimodal imaging, robust registration of functional and anatomical information is still a challenge, particularly in small-animal imaging given the lesser structural content of certain anatomical parts, such as the brain, than in humans. Besides, patient-dependent and acquisition artefacts affecting the images information content further complicate registration, as is the case of intensity inhomogeneities (IIH) showing in MRI and the partial volume effect (PVE) attached to PET imaging. Reference methods exist for accurate image registration but their performance is severely deteriorated in situations involving little images overlap. While several approaches to IIH and PVE correction exist these methods still do not guarantee or rely on robust registration. This Thesis focuses on overcoming current limitations of registration to enable novel IIH and PVE correction methods.

Key words: registration, small animal, brain, mutual information, intensity inhomogeneity, partial volume effect, non-overlapping field of view, entropy, mutual multiresolution analysis, discrete wavelet transform.

Preface

Image registration is the process of aligning structures appearing in different images and has manifold applications with particular relevance in the medical field. Most of the research devoted to medical analysis has focused on registration due to its relevant role on clinical diagnostic and treatment decisions as well as for being a key previous step to region segmentation and biological markers quantification in research. With the advent of new technologies for multimodal imaging, robust registration of functional and anatomical complementary information is still a challenge, particularly in small-animal imaging given the lesser structural content of certain anatomical parts, such as the brain, than in humans. Besides, patient-dependent and acquisition artefacts affecting the information content of the images further complicate registration. It is the case of the intensity inhomogeneities (IIH) showing in MRI and the partial volume effect (PVE) attached to PET imaging. Reference methods exist for accurate image registration but their performance is severely deteriorated in adverse situations involving little initial images overlap or a mismatched images field of view (FOV) not uncommon in clinical practice and research. While several approaches to IIH and PVE correction exist these methods still do not guarantee or rely on robust registration. The focus of this Thesis is on overcoming current limitations of registration to enable novel IIH and PVE correction methods. Publicly available brain human images and in-house brain mice datasets have been used. First, a novel rigid-registration method has been developed that enhances the capture range and FOV insensitivity with respect to reference automatic registration methods. Next, a novel method has been developed that jointly improves registration accuracy and IIH correction. Finally, a novel energy equalization approach dependent on accurate multimodal registration has been developed and implemented using a mutual multiresolution scheme for correction of PVE in PET images. The contribution of this thesis will allow a significant enhancement of the accuracy and precision in the quantification of medical imaging modalities, both in human and small-animal research applications.

Acknowledgements

My first and most sincere acknowledgement goes to my PhD directors Juan Domingo Gispert and Ferran Marques. They have been supportive all along the journey, which I started in Barcelona (Spain) as a Medical Image Engineer, continued in Cambridge (USA) as a Biomedical Engineer at the Massachusetts Institute of Technology, and culminated back at home as a reckless entrepreneur. I will always be greatful for their infinite patience, understanding, support and invaluable guidance, the fuel of my endeavours for the completion of this PhD Thesis. They are two references from whom I take their professionalism, rigour and practicality as model values to pursue. It is my fortune to have met JuanDo, besides my PhD Thesis co-director, my mentor and advisor.

There is no career accomplishment without personal stability, satisfaction and comfort. Thank you Andrea, my wife, companion and ally for your inconditional love and for giving me peace. Living life with you helps me putting things in perspective and addressing challenges in a calmer and more confident manner. With you by my side, I enjoy all aspects of life at the highest possible level and so I have the PhD.

There is a great deal of my mother and father in everything I do, for I am their son. They have set the basis of my character and shared with me their values, beliefs, and humanity. I find no better way to express the admiration I have for them than projecting those values to the environment through my relationships with people and my work. Therefore, this PhD Thesis has also the signature of Paco and Elena. And there is also part of me that has been shaped by my brother, Carlos. Because of him I have re-defined the term generosity, tolerance, and persistance in my dictionary, needless to say, vital for the particular accomplishment of this work. He also reminds me how important to face challenges with ingenuity and curiosity is, probably the seed of innovative ideas (and hopefully some of mine are!). I do not feel "law" suits them when I refer to my mother- and brother-in-law, Carme and Ferran. To them, Raquel and Vicenç, all my love and thankfulness for their generosity, which has been fundamental to focus on the completion of this manuscript and pursue my carrer objectives.

To my grandma, whom I think of very often, the rest of family and friends, thanks for being always there when I need you, for instance, for a break of my working on this Thesis.

Table of contents

Tables list

Figures list

Acronyms

AAL	Automatic Anatomical Labelling
CC	Correlation Coefficient
CSF	Cerebrospinal fluid
CT	Computerized Tomography
DWT	Discrete Wavelet Transform
EM	Expectation Maximization
FLE	Fiducial Localization Error
fMRI	Functional Magnetic Resonance Image
FRE	Fiducial Registration Error
FWHM	Full Width at Half Maximum
FOV	Field Of View
GM	Gray Matter
GTM	Geometric Transfer Matrix
IIH	Intensity Inhomogeneity
IRIS	Iterative Registration IIH correction Strategy
LOS	Line OF Response
MG	Müller-Gärtner
MI	Mutual Information
ML	Maximum Likelihood
MoM	Method of Moments
MR	Magnetic Resonance
MRI	Magnetic Resonance Image
MMA	Mutual Multiresolution Analysis
NMI	Normalized Mutual Information
PET	Positron Emission Tomography
PIU	Partitioned Image Uniformity
PSF	Point Spread Function
PVE	Partial Volume Effect
RC	Recovery Coefficien
RF	Radriofrequency
RIRE	Retrospective Image Registration Evaluation
RIU	Ratio Image Uniformity

RMS	Root Mean Square
ROI	Region Of Interest
RSF	Region Spread Function
SD	Standard Deviation
SMI	Stable Entropies Mutual Information
SNR	Signal to Noise Ratio
SPECT	Single-Photon Emission Computed Tomography
SPM	Statistical Parametric Mapping
SSD	Sum of Squares intensity Differences
TOF	Time Of Flight
TRE	Target Registration Error
U/S	Ultrasound
VOI	Volumetric Region of Interest
VOXEL	Volumetric Pixel
WM	White Matter

1. Introduction

1.1. Context

The field of this Thesis is on image registration with special focus on the medical application. Image registration is the process of spatially aligning two (or more) images of the same object(s) into a common coordinates space. As a key processing step in manifold applications, research on this topic has been very active for the past 35 years and other definitions have been proposed in (Brown 1992; Habib and Ai-Ruzouq 2005; Xiong and Zhang 2009) that are specific to each field.

Image registration finds its application in video surveillance where moving objects or persons are tracked for security purposes; in compression of video images to achieve higher transmission rates by reducing the amount of transmitted data through optimized coding of static and moving objects in neighbour frames; in remote sensing for weather forecasting; in computer vision for automatic quality control of manufactured products; and, in medical imaging, for example, to combine information obtained with different image modalities to monitor tumour growth in a cancer patient (Zitova 2003; Wyawahare et al. 2009; Oliveira & Tavares 2012). In the medical field, the imaged objects consist of whole or partial body parts of the human anatomy. Structural or anatomical information is acquired with computerized tomography (CT) or magnetic resonance imaging (MRI) whereas functional or biological information such as glucose uptake, oxygen consumption or changes in blood oxygen levels secondary to neurological activation is obtained from positron emission tomography (PET), single-photon emission computed tomography (SPECT) or functional magnetic resonance imaging (fMRI), respectively. **Multimodal imaging** refers to the use of two or more imaging techniques (or modalities).

Registration of medical images has attracted much of the work devoted to medical image analysis due to its impact and relevance in the clinical practice and in research (Fitzpatrick et al. 2000; Oliveira & Tavares 2012). In the clinical setting, registration is used to overlay or fuse images obtained at different time points of the same or different image modalities. As a result, physicians have diagnostic and complementary information available they can interpret to deliver non-invasive, fast, and quality care to patients (Fig. 1). Besides tumour growth monitoring in cancer patients, physicians can also plan cardiac, brain or other surgical interventions and treatment (Ballesteros-Zebadua et al. 2016; Gering et al. 1999; Huang et al. 2009; Hurvitz and Joskowicz 2008; King et al. 2010; Maurer et al. 1997; Staring et al. 2009) achieve accurate diagnosis and follow-up of cardiovascular diseases (Huang et al. 2009; Carvalho et al. 2014) and, effectively plan radiation therapy (Foskey et al. 2005; Lavely et al. 2004; Hauler et al. 2016).

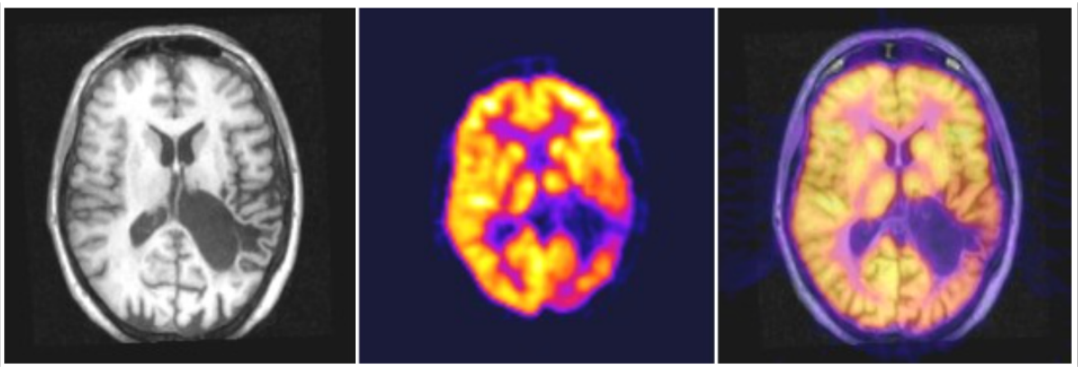

Figure 1. On the left, a axial slice of a brain MRI of a patient with periventricular leukomalacia. In the middle, an 18F-FDG PET image of the same subject is shown. Brighter intensities represent high glucose uptake. On the right, automatic registration of both images showing functional-to-anatomical correspondence between images.

In research, clinical interpretation of images alone is often not sufficient to draw clinically confident conclusions, and measurable and quantifiable data is needed. Particularly important is the research of biomarkers to understand disease behaviour and to discover new treatments. For instance, in the quest for finding a cure to Alzheimer's disease, several biomarkers (Fouquet et al. 2014) including tau protein (Meier et al. 2016), β amyloid (Aβ) plaque (Serrano-Pozo et al. 2016), and atrophy of the amygdala (Poulin et al. 2011) have been studied in large samples of volunteers and patients with functional and anatomical MRI and PET imaging. It is through the characterization of biomarkers intensity and spatial distribution changes that advances are made towards better understanding of diseases. To this purpose, regions of interest (ROI) may be delineated or segmented by means of binary masks preferably on anatomical images conveying higher structural information. Next, functional or anatomical images under study may be later registered to their segmented anatomical counterpart images to obtain regional biological or structural quantitative measurements. When matched or paired images of the same patient or subject are not available, pre-segmented templates or atlases in a standardized or reference spatial space may be used for automatic registration and quantification. Templates are average images computed from registered monomodal images of a target population sample, which is usually composed of healthy volunteers. In this context, registration is once again critical for quantification, accurate segmentation, and atlas building (Freeborough & Fox 1998; Ganser et al. 2004; Joshi et al. 2004; Leow et al. 2006; Wu et al. 2009; Collins & Evans 1997; Frangi et al. 2003; Dornheim et al. 2005; Martin et al. 2008; Isgum et al. 2009; Zhuang et al. 2010; Liu et al. 2015).

Nowadays, the pipelined process of monomodal or multimodal registration, segmentation and quantification can be fully automatized and results obtained in a fraction of time than if manually done by an army of operators. The advent of powerful and affordable processing computers since the 1980s undoubtedly propelled the growth and relevance of medical image processing and analysis. Several software packages such as FSL (Jenkinson et al. 2012), FreeSurfer (Fischl 2013), PMOD (PMOD Technologies, Zürich,

Switzerland), 3D Slicer (Pieper et al. 2004), or Elastix (Klein et al. 2010) are currently available and some of their applications are described in the review article by (Piotr J. Slomka & Baum 2009). In this thesis, version 8 of the widely-known and extensively-used Statistical Parametric Mapping (SPM) (Friston et al. 1995; Ashburner 2012) package written in Matlab code (The Mathworks, Inc., Natick, Massachusetts, USA) was used. Because the brain is mostly static, fix, and invariable (except in pathological cases such as after surgical resection) it has favoured the development of image processing methods that perform robustly across different subjects or patients and has led to the advent of numerous brain-specific processing methods that are now available in commonly open access software packages. In addition to software, open datasets are available for study purposes including MR datasets (BrainWeb project (Cocosco et al. 1997), MIRIAD Scan Database (Malone et al. 2013)), PET datasets (PET-SORTEO project (Reilhac et al. 2005)), or both (ADNI project (Mueller et al. 2005)). The availability of these datasets has resulted in a huge amount of work and advancement in the study of neurological diseases and has expedited the discovery of new neurological biomarkers. The medical imaging and pharmaceutical industries have taken leadership of such progress through huge economic investments that have leveraged the development of not only of human imaging but also of small animal or pre-clinical imaging, pivotal to test for safety and efficacy of new treatments. Many efforts are being devoted to translate imaging techniques and methods applied in humans to pre-clinical research yet not exempted of difficulties. As an example, the limited resolution and the larger artifact magnitudes attached to small-animal imaging systems commonly restrict the direct application of human registration and artifact correction methods to small-animal datasets. This being said, tremendous advances are being done including the development of hybrid systems combining CT-PET and, more recently, MR-PET and photo-acoustic imaging. With registration being integrated during the imaging process, such systems allow simultaneous structural and functional information acquisition, which reduces diagnostic time and patient discomfort as well as offers new research opportunities (Catana et al. 2008; Judenhofer et al. 2008; Riola-Parada et al. 2016). However, there are still important implementation challenges and controversy in the cost-benefit advantages and ultimate ubiquity of some of these systems (Barbosa et al. 2015). While the development of hybrid systems for specific applications will surely co-exist with software-based registration, only registration methods have the potential of robustly and accurately combine multiple and large image datasets, and multiple image modalities, resulting essential to accomplish quantification.

1.2. Registration methods

The aim of image registration is to find the geometrical transformation that puts information of an object conveyed in two or more images into spatial correspondence. This process requires selection of the image features to be aligned, a feature similarity metric that measures alignment quality, a geometric transformation type, and a search strategy for the transformation parameters that optimize the value of the similarity

measure. Due to the great diversity of images and clinical and research problems to be solved through registration, a universal combination of the above-mentioned sub-processes that accomplishes perfect registration for each case proves challenging. However, a great deal of methods has been devised to propose specific solutions to perform robustly against as many of these problems as possible. While several registration methods classifications have been published, the most widely referenced classification scheme in medical imaging is the one proposed by (Maintz & Viergever 1998). In their classification the authors define nine fundamental criteria where each criterion was further divided into one or more sub-criteria.

Medical image registration methods can be classified according to images dimensionality, images modalities, imaged subjects, imaged objects, degree of interaction during registration, registration basis, nature and domain of transformation, and optimization. In this thesis, special emphasis has been made on the registration basis classification criterion, as similarly done in (Fitzpatrick et al. 2000), because it allows a seamless introduction of the registration challenges addressed herein. Likewise, special attention has been paid to optimization methods, geometric transformation types, and registration accuracy assessment methods that relate to the proposed work of this Thesis.

Images dimensionality refers to the number of spatial dimensions of the image (2D, 3D, etc.). Commonly, medical images are volumetric or 3D images acquired with tomographic imaging scanners and are considered 4D when serial images are acquired to image dynamic processes. Although sometimes two-dimensional images are also used, these can always be considered in a 3D space.

Modalities refers to the means by which images are acquired (MR, PET, CT, U/S, etc.). Intra-modal or monomodal registration is given when images to be registered have been obtained with the same imaging modality, e.g. MR-MR. Conversely, inter-modal or multimodal registration results from registering images acquired with different imaging modalities, e.g. CT-PET. There are different possible sub-modalities in MR imaging depending on the imaging parameters used to obtain the information of interest, e.g. T1-weighted (T1w) MR, proton density (PD) MR, or functional MR (fMRI). Registration of such sub-modalities is usually classified as multi-modal.

Subject refers to whether images to be registered are obtained from the same or different subjects. The former case is classified as intra-subject registration, and the later as inter-subject registration. A third category is when images from one or more subjects are registered to an atlas. As introduced earlier, atlases are created from healthy volunteers belonging to the target population that will serve as control against the sample under study.

Object refers to the part of the human anatomy that is being imaged (brain, liver, heart, prostrate, etc.). The work of this thesis, as well as the bulk part of medical image registration methods, is focused on brain imaging.

Degree of interaction refers to the level of user/operator involvedness in the registration process. Manual registration implies the maximum level of involvedness with the operator autonomously finding best alignment between images. An intermediate level of interaction requiring the operator to select image features or to pre-align the images is typical of semi-automatic registration methods. Automatic registration requires no level of interaction in the registration process other than selecting the input images.

Nature and domain of transformation refers to whether the spatial transformation involves some object deformation to find alignment and whether the transformation space is 1D, 2D, or 3D. Although only 1D or 2D displacements are theoretically possible, this is a rare phenomenon because subjects move in a three-dimensional space. Rigid registrations involving no images deformation are appropriate for intra-subject bone and brain images and are the focus of this work. More elastic organs such as the liver or the heart require some anatomical deformation to find feature alignment (Ledesma-Carbayo et al. 2005; Grgic et al. 2009). We examine in more detail the types of geometrical transformation in *1.4. Geometric transformations*.

Registration basis refers to the image feature space used for registration. In other words, it refers to the data that is going to be used by the registration method to find alignment between images. Some methods use external markers or anatomical landmarks as target registration points that are visible in each of the involved image modalities. Such methods are called prospective because they use such markers with "*prospect*" for registration after image acquisition. When registration relies solely on the images information, we refer to retrospective registration. Some retrospective methods use segmented binary masks or surfaces of anatomical regions of interest to drive registration; other methods are based on finding maximum intensity correspondence between images and, sometimes, they may be combined. We describe some of these methods in section *1.5. Registration basis*.

Optimization refers to the process of finding the geometrical transformation parameters that minimize or maximize a similarity metric. A similarity metric can be understood as an alignment quality of the images computed as the distance between features of the images. It is therefore a function whose dimension depends on the number of transformation parameters. When applied to medical images, such function shows a global optimum and several optima. The challenge of the optimization algorithm is, therefore, to find the global optima among the local optima. This topic is further developed in the following section.

1.3. Optimization

Different types of optimization methods have been devised. The vast majority are iterative algorithms evaluating a similarity metric until its value is usually below a pre-determined threshold. Differing from other methods simultaneously searching all transformation parameters (Nelder & Mead 1965), Powell's method (Powell 1994) makes a sequential and one-dimensional search of the transformation parameters. Therefore, the algorithm starts finding a first transformation parameter that minimizes the similarity metric, it then updates the transformation parameters set with the new value, and continues the search for the next parameter. The sequence is restarted until the similarity metric is below a minimization threshold or else, after exceeding a pre-defined number of sequence iterations. As a result, the more complex the required geometrical transformation, i.e. the larger the number of transformation parameters, the more time-consuming will be the search. Because it is not necessary to take derivatives - it uses Brent's root-finding method (Brent 1973), Powell's method is useful in minimization of complex functions with multiple local optima typical in medical imaging. However, it is also susceptible of finding local optima. While this outcome may seem a downside, it proves very appropriate in medical imaging since true alignment commonly produces a local (not global) optima (Hill et al. 2001; Pascau 2006). The reason for this being that when the volume of the region of interest is small in relation to the rest of the image volume, features outside the target region drive minimization of the similarity metric value. In brain images, for instance, the brain usually occupies a smaller image volume than the background, i.e. air. That is why Powell's method shows superior robustness over other optimization strategies (Maes et al. 1999), such as the simplex downhill approach (Nelder & Mead 1965), and is the optimization method used herein for registration purposes. Despite of being computationally more efficient and addressing the minimization problem from a more global perspective, through simultaneous search of the transformation parameters, the Nelder and Mead method under-performs the Powell's method in clinical and pre-clinical image registration (Fitzpatrick et al. 2000; Pascau 2006). Other methods exist that have been used in the field of image registration such as the Gauss – Newton, the Levenberg-Marquardt, the gradient ascent or descent, the quasi-Newton, the stochastic algorithms, and evolutionary algorithms whose description can be found in (Press et al. 2007). It is worth mentioning that sometimes the minimization problem can be defined in the least squares sense and be solved directly, a process known as the Procrustes problem. It is the case of point-based registration methods with translations being obtained from the centroids of the point sets in both images, and rotations being obtained from single value decomposition (SVD) of the covariance matrix generated from the demeaned set of points (Maurer et al. 1995; Mandava et al. 1992).

In medical imaging, only one local optimum corresponds to true alignment. The rest of local optima are produced by moderate matching of image features as well as interpolation artefacts (Tsao 2003). To partly remove local optima from ill-smoothed similarity functions, the Powell's method is implemented in a

multiresolution framework where registration is performed in, at least, two steps (Oliveira & Tavares 2012). First, low-resolution versions of the images are registered achieving a coarse alignment. Then, optimization resumes with the original and high-resolution images to achieve fine and (hopefully) true alignment. This hierarchical approach has a two-fold advantage over previous strategies. On one side, the smoothing of the images reduces interpolation- and noise-related optima increasing thus the capture range of the method. On the other side, overall minimization time is reduced because the cumulative time of sequential convergence at each resolution level is less than one-step full-resolution optimization.

1.4. Geometric transformations

A geometric transformation is a mapping of the image voxels in a given coordinate space to the corresponding spatial locations in the coordinate space of another image. Rigid-body transformations preserve the anatomical distances of the moving image in the original space, whereas non-rigid or elastic transformations apply some deformation to the moving image to find feature alignment with the static or fix image. Therefore, the choice of the transformation depends on the problem we aim to solve. In the case of registration to an atlas, a combination of both rigid and non-rigid transformations is used. The rigid-body transformation accomplishes a coarse alignment of the anatomical features between the moving image and the atlas. And then, a non-rigid transformation modifies the shape and size of anatomical structures in the original image to match those of the atlas in a reference space. Transformed original images are then ready for automatic segmentation and quantification. In this thesis, we will only use rigid-body three-dimensional transformations. The classification made by (Fitzpatrick et al. 2000) is provided together with a graphical example of each geometric transformation (Fig. 2).

- **Rigid-body transformation:** the anatomical distances of the original image are preserved. The transformation consists of six parameters: three **translations** in and three **rotations** about each dimension. Multimodal MR-PET or CT-PET registrations use this type of transformation.

Non-rigid transformations

- **Scaling transformation:** voxels are dilated or contracted creating a zooming effect. This transformation type consists of nine parameters: six correspond to the rigid-body transformation and three more for a zooming factor in each dimension. This type of transformation is useful to compensate for calibration errors of MR gradient coils.
- **Affine transformation:** straightness of and parallelism between lines is preserved, and hence, so is the planarity of surfaces, but the angles are changed. This type of transformation corrects for skew, for example, in CT images when the gantry angle is incorrectly recorded. It is a general formulation for the

more specific scaling transformation. Here, twelve parameters are needed: nine for the scaling transformation and three more parameters to allow changes of the angles about each dimension.

- **Perspective transformation:** only straightness of lines is preserved, but not parallelism between them. Here, three more parameters are added totalling to 15. This type of transformation is observed in two-dimensional *perspective* images of human anatomy in x-ray, endoscopy, or laparoscopy imaging but is rarely used in registration of volumetric images.
- **Curved or elastic transformation:** this type of transformation allows breaking the parallelism between lines and, as opposed to the other types of transformations, the mapping function is defined as a set of piece-wise polynomials or transformation blocks. In particular, transformations are partitioned into planes with univariate polynomials being defined only over those planes. Ultimately, the resulting three-dimensional transformation corresponds to the product of these three univariate polynomials. Splines are univariate polynomials that accomplish smooth junctions between transformation blocks, where the corner of such blocks are called knots. In particular, splines of order three (or cubic splines) are widely used in medical imaging. Also widely used are elastic transformations with a cosine polynomial basis, known as the Discrete Cosine Transform (DCT), which is implemented in the SPM package. Thin-Plate Splines (TPS) transformation are also used in medical imaging because it allows an arbitrary placement of the knots, as opposed to the rectangular grid used in cubic splines, which favours accurate registration of specific regions of interest.

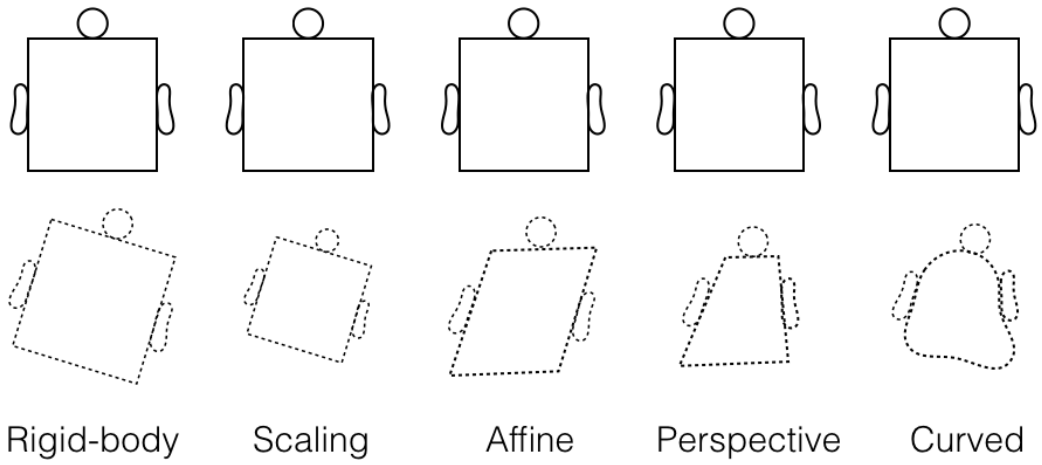

Figure 2. Types of geometric transformations used in medical image registration. Above, the original image is shown. The corresponding transformed image is shown below.

1.4.1. Rectification

Elastic transformations are used beyond registration purposes to correct for spatial distortions in MR imaging. Such type of correction is called *rectification*. Distortions may arise from non-uniform variations of the

gradient fields and/or static field due to imperfections of the scanner coils or induced by magnetization of anatomical regions. However they are generated, they can be corrected by means of a geometrical transformation that brings all points in the image to their corresponding position in the physical space (Fitzpatrick et al. 2000). For correction of field non-uniformities, this geometrical transformation may be then applied to patient images for an arbitrary short period of time before another calibration is needed. Field inhomogeneity and scale distortion may be corrected by means of imaging phantoms or stereotactic frames of known geometry. When it is gradient fields that originate distortions, a second image can be obtained with the reversed gradient direction. The corrected image is the result of the averaged two MR images acquired with reversed readout gradients (Chang & Fitzpatrick 1992; Maurer et al. 1996; Gelman et al. 2014).

1.5. Registration basis

There has been a gradual introduction of novel registration methods based on the image features used to accomplish alignment. Because registration aims at finding spatial correspondence between features, it is desirable that (the same) features are easily identified in all images and that these change little after spatially transformed. Conceptually, the use of control points in the images meets all of these requirements and hence, where firstly used for registration in late 1980s. The actual hurdles in the practical implementation of **point-based** methods gave rise to **surface-based** methods in early 1990s, which can be understood as an extension of point-based methods. The need of surface-based methods for segmentation of surfaces, rarely a trivial process and dependent on the image modality, and the advent of powerful computer processors led to the emergence of intensity-based methods, also in early 1990s. **Intensity-based** methods do not require segmentation as they rely on the intensity value of the image voxels. The ease of implementation and applicability to a wide range of registration problems has favoured the fast adoption of intensity-based methods for clinical use. Nowadays, reference medical registration methods rely on intensity-based methods, and when needed are complemented with point-based or surface-based methods, e.g. intra-operative image guidance.

1.5.1. Point-based registration

The use of a set of paired points located at the same physical position in the images implies that a transformation can be found that aligns the points. Because registration relies on such points, they are called fiducial points, or fiducials. Fiducials can be distinct anatomical landmarks or external markers attached to the anatomy. A distinct advantage of fiducials is that a direct or closed-form solution of the geometric transformation that minimizes the root mean square (RMS) distance of fiducials between images can be found (Aarun et al. 1987). A common anatomical landmark is the intersection of the central sulcus with the

midline of the brain (Fitzpatrick et al. 2000; Peelle et al. 2012). External markers can be invasive (stereotactic frames (Maurin et al. 2009; Fitzpatrick 2010), implanted gold markers (Budiharto et al. 2009), etc.) or can be attached to the surface of the anatomy. They are designed to be visible in multimodal imaging and, importantly, are independent of anatomy. However, the invasiveness of some of these markers, the fact that non-invasive markers may move or detach from skin, their elevated cost, the need for planning registration, and that in either case they result uncomfortable or painful to the patient limits their use to radiation therapy and brain surgery. In radiation therapy or surgery, pre-operative images, e.g. MR or CT, are used to delimit the affected region. Then, intra-operative registration of pre-operative images to anatomical images obtained with fast-acquisition modalities, e.g. X-ray or ultrasound, is used to effectively deliver treatment or operate (King et al. 2010).

1.5.1.a. Registration accuracy assessment

Registration accuracy depends on the degree of correspondence between fiducials, whichever their type. In either case, there is an inevitable displacement between the fiducial localization and the intended or true location that is known as the fiducial localization error (**FLE**). In landmark-based registration, this displacement can be attributed to the operator locating the fiducials. In marker-based registration, fiducial localization can be obtained through algorithmic computation of the marker centroid (Wang et al. 1996). FLE is caused here by image noise and the discrete nature of images instead, that challenge accurate computation of markers centroid. Note that, in the extreme case when the fiducial is smaller than the image voxel, FLE will be below the voxel dimensions. Understanding FLE as an independent random variable uniformly distributed around the true position, the overall FLE in the image reduces with increasing number of points (noise is reduced/cancelled), larger fiducial size (centroid calculation accuracy is increased) and larger image marker intensity (signal-to-noise ratio also improves centroid calculation accuracy). While FLE is a measure of local fiducial displacement, a global measure that provides the effective FLE for the entire image is the RMS error. When the RMS is computed for the images fiducial pairs, it also becomes a measure of misalignment and is called fiducial registration error (**FRE**):

$$FRE^2 = \frac{1}{N}\sum_{i=1}^{N} |p_i^{'} - p_i|^2 \quad (1)$$

With *pi* and *pi*', the localization of a fiducial *i* in the reference image and the equivalent fiducial in the moving image after registration, and *N* the total number of fiducials. The relationship of the expected FRE and FLE for a given image is provided by the following approximation:

$$FRE^2 \approx (1 - \frac{2}{N}) \times FLE^2 \quad (2)$$

Therefore, when FRE is used to measure rigid-body fiducial-based misalignment between images (Fig. 3), overall registration FRE must account for FLE in both images. In this context, if the FRE is calculated for one (target) point of interest (not a fiducial), we refer to the target registration error (**TRE**).

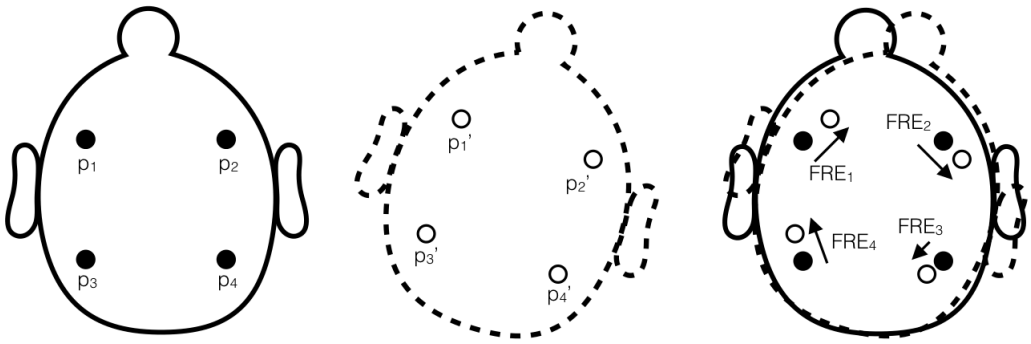

Figure 3. Schematic representation of the Fiducial Registration Error. On the left, four markers implanted on the head bone are shown in the reference image. In the middle, a misaligned image of the same patient is shown. On the right, the arrows represent the FRE magnitude for each marker as the distance from the marker centroid in the reference image to the marker centroid in the transformed image.

Distinctly, TRE is sensitive to the location of the fiducial, as opposed to FRE. Take, for example, an approximate circular configuration of markers in a stereotactic head frame. Target points located near the centroid of the fiducials set will have associated smaller TRE than target points located at the periphery of the brain surface, closer to the fiducials. For a given spatial transformation with a given rotational component R, the spatial displacement of points located in outer positions in the image is larger than points located near the centre of the image. This statement does not hold for purely translational transformations, unlikely in medical image registration problems. Therefore, TRE does depend on target position and fiducial configuration, and its value can be approximated relative to the (three) principal axes of the fiducial configuration:

$$TRE^2 \approx \frac{1}{N}\left(1 + \frac{1}{3}\sum_{k=1}^{3}\frac{d_k^2}{f_k^2}\right) FLE^2 \qquad (3)$$

Where d_k is the distance of the target from principal axis k, and f_k is the RMS of the fiducials distance from the same axis (Fitzpatrick et al. 1998). As a result, FRE and TRE can be complementarily used in fiducial-based registration to obtain both an overall estimation of image registration accuracy or robustness (by means of FRE), and an estimation of the regional accuracy and precision of the method (by means of TRE).

TRE is used in the Vanderbilt Retrospective Image Registration Evaluation (RIRE) Project (West, J. M. Fitzpatrick, et al. 1997) to compare retrospective rigid-based registration methods of brain CT-MR and PET-MR images of patients who would eventually undergo brain surgery. Gold-standard registration was accomplished through point-based alignment (Aarun et al. 1987) of implanted markers in the head bone or cranium. Then, markers were digitally removed and images were made available in the RIRE website (Fitzpatrick 2006), where registration results can be electronically submitted and the registration error retrieved. In order to provide clinically meaningful TRE values, ROI of relevant brain areas where defined in the images and the centroid of the images was used as target points (Fig. 4). Finally, the registration error was calculated as the median and maximum TRE of the VOIs (West, J. M. Fitzpatrick, et al. 1997). The RIRE database was used in this Thesis to assess the accuracy and robustness of the proposed registration method.

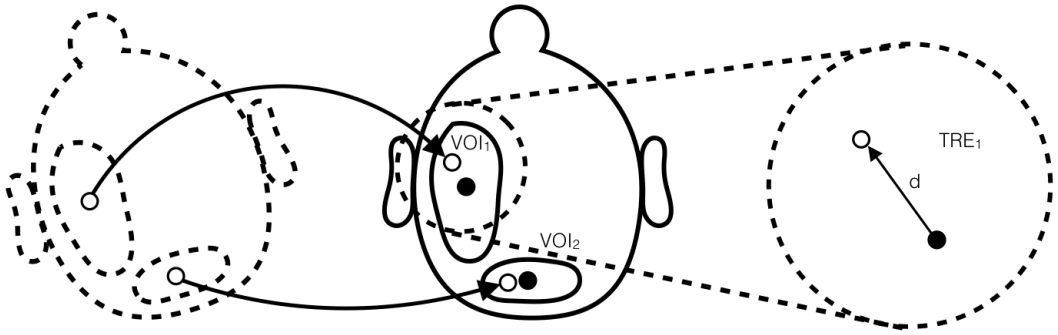

Figure 4. Schematic representation of TRE determination in the Retrospective Image Registration Evaluation (RIRE) project. On the left, the misaligned image is shown in dashed lines. Two volumes of interests (VOIs) are delineated in relevant brain areas and their centroids shown as white circles. In the middle, the transformed VOI centroids are overlapped onto the reference image, drawn in solid lines. It can be observed that the registration error between VOI centroids is different for each VOI. In the RIRE project, the TRE of a VOI is determined as the Euclidean distance between centroids of the same VOI after rigid-body registration.

1.5.2. Surface-based registration

Similarly to the use of anatomical landmarks in point-based registration methods, anatomical boundaries or surfaces are salient image features that are used in surface-based registration methods. However, not all surfaces are easily segmented in all images modalities. Surface extraction of skin-air and bone-skin interfaces are nowadays an automated and robust procedure in multiple image modalities such as MR or CT. More challenging is the extraction of soft tissue interfaces due to the lower contrast between soft tissues obtained with these techniques.

Surfaces can be represented by either a point set or collection of surface points, a faceted surface where points are connected between them, or parametric surfaces described by polynomial functions, e.g. B-splines.

Intuitively, surface-based methods can be regarded as an extension of point-based methods, yet a major distinction between them must be considered. In surface-based methods there is no exact correspondence between surface points of structures to be registered. This causes surface-based methods to depend on an iterative search for the transformation parameters that minimize some sort of distance between surfaces, as opposed to rigid-base point-based registrations where a direct solution of the geometric transformation may be found (Maurer et al. 1995; Mandava et al. 1992).

Surface-based methods can be classified based on the distance metric between surfaces points used for registration. Minimization of the Euclidean and Hausdorff distances (or disparity functions) were used first, but their performance is hindered in cases where there is little or no overlap between surfaces, a common situation in medical image registration. In order to palliate this effect, non-overlapping points can be given a lower weight than overlapping regions involving the information of interest. Similarly, weighting can be also used to increase the sensitivity of the disparity function to areas of high curvature that may become more important to the registration than those points in planar regions (Fitzpatrick et al. 2000). The *head* and *hat* algorithm (Pelizzari et al. 1989) was the first surface-based method used for medical image registration of CT, MR, and PET images of the head, precisely. As it name insinuates, the conceptual idea is to fit the *hat* into the *head*. The *head* is typically the surface of the highest-resolution image covering the larger object volume. Surface fitting is accomplished by pulling the *hat* surface points towards the centroid of the segmented *head* image. Optimal registration is achieved through minimization of the distance between *hat* surface points and *head* points lying in the intersection of the *head* surface and an imaginary line crossing the *head* image centroid. This definition of distance did not prove very successful since it required good initial transformations and significant user interaction. (Besl & McKay 1992) proposed an algorithm based on minimizing the distance between the point and the closest point on the surface. This algorithm is known as the Iterative Closest Point (ICP) method and its extended version including weighting (Weighted Geometric Feature, WGF) are being still used in recent studies (Ji et al. 2008; Farnia et al. 2012).

1.5.3. Considerations of point-based and surface-based methods

Point-based and surface-based registrations have the main drawback of requiring either intensive user interaction or accurate tissue segmentation. Although the usage of a subsample of the images data (points or surfaces) speeds up the registration process, this advantage is diluted by the larger time needed for fiducials localization or segmentation (West, J. M. Fitzpatrick, et al. 1997). This being said, these methods do still have a relevant role in medical image registration. On one side, the use of fiducials enables drawing a quantitative error of registration as explained in section *1.5.1.a. Registration accuracy assessment*. Besides, marker-based registration is useful when registering images with low background-to-object contrast as well

as for real-time registration in neurosurgical operations (Ji et al. 2008; Farnia et al. 2012). On the other side and when accurate segmentation is possible, non-rigid surface-based registration can accomplish very accurate structures alignment (error<1 mm) needed, for instance, for the study of cortical atrophy (Li et al. 2015). Without losing sight of the advantages offered by point-based and surface-based methods, intensity-based approaches require much less or no user interaction or segmentation. Such advantage over previous approaches has favoured significant advancement in the development of intensity-based methods that have found applicability in a wide variety of intra-/inter-subject multimodal studies. As a result, the use of intensity-based methods prevails today in the clinical context (Oliveira & Tavares 2012), although they may also be complemented with point-based (Rueckert et al. 2003) and surface-based (Greve & Fischl 2009; Cizek et al. 2004; Rusu et al. 2014) methods.

1.5.4. Intensity-based registration

Intensity-based registration relies solely on the voxel intensity values of images to minimize a given similarity metric. Because the use of only a subsample of the data speeds up computation, intensity-based methods unanimously use similarity metrics that are computed over the images overlapping region. Broadly, the aim is to find the geometric transformation that maximizes the voxel-wise correspondence between images. This is a more general approach to registration than that proposed in point-based and surface-based methods. Now, image features such as fiducial points or surfaces do not need to be previously identified. Besides, registration accuracy is no longer based on the degree of alignment of these structures but on an overall similarity metric including all voxels (within the overlapping region). Consequently, intensity-based methods can be used to register images of the same or different dimensionality, modality, or patient. Unlike rigid-body point-based methods, intensity-based methods use iterative searching of the transformation parameters and are generally implemented in a multiresolution framework, described in section *1.3. Optimization*. First, intensity-based methods were intended for monomodal image registration. It was not until mid 1990s that a group of researchers at Leuven (Belgium) (Maes et al. 1997) and at MIT (USA) (Wells et al. 1996) proposed information-based measures that proved to be generally applicable and became the gold standard of medical image registration. A description of the more remarkable intensity-based methods is provided next.

First, some notation is introduced. The images to be registered are A and B. $B'=T(B)$ refers to image B after successive estimations of the registration transform T. And $\wp = A \cap B'$ is the overlapping domain between images A and B' with total number of voxels N. Consequently, $\wp$ will change during the search of T.

1.5.4.a. Sum of Squares of Intensity Differences (SSD)

In general, images of the same patient obtained at two or more different time points should look very similar. At true registration, co-localized voxel intensity differences between images should be very small, approaching image noise level. At misalignment, co-localized voxels intensity differences between images should otherwise increase. The sum of squares of intensity differences (SSD) becomes a useful similarity metric of serial monomodal images. For images *A* and *B*' with voxels *i*, the SSD is expressed as follows:

$$SSD = \frac{1}{N}\sum_i^N |A(i) - B'(i)|^2 \qquad \forall i \in \wp \tag{4}$$

As observed, the squaring of the intensity differences largely penalizes dissimilarities between co-localized voxels intensities. In MR studies the scalp may fall at the verge of the scanner field of view (FOV) where the static field starts losing homogeneity. This field inhomogeneity distorts and corrupts the intensity levels of the outer area of the image (West, J. Fitzpatrick, et al. 1997). For SSD to produce satisfactory output, segmentation or correction of distorted parts is desirable prior to registration.

1.5.4.b. Correlation Coefficient (CC)

Alternatively to the SSD, the correlation coefficient (CC) was intended to overcome any global intensity bias between images. The CC is useful as long as there is a linear relationship between the images intensity values. Evidently, its application is limited to monomodal registrations. The CC is expressed as

$$CC = \frac{\sum_i (A(i)-\bar{A}) \times (B'(i)-\overline{B'})}{\sqrt{\sum_i (A(i)-\bar{A})^2 \times \sum_i (B'(i)-\overline{B'})^2}} \qquad \forall i \in \wp \tag{5}$$

with $\bar{A}$ and $\overline{B'}$ being the intensity mean of voxels in the overlapping region of images A and B', respectively.

1.5.4.c. Ratio-Image Uniformity (RIU)

The rationale behind the ratio-image uniformity (RIU) lies on the fact that the ratio of co-localized voxel intensities between perfectly aligned identical images should produce a uniform image of value one in all voxels. Hence, the intensity uniformity of the ratio image *R* worsens with misalignment. This approach is conceptually equivalent to SSD explained above in section *1.5.4.a. Sum of Squares of Intensity Differences*

(SSD). Actually, RIU is the name given to the coefficient of variation (CV) of the ratio-image intensities, which can be calculated as

$$RIU = \frac{\sigma_R}{\mu_R} \tag{6}$$

With σ_R and μ_R being the standard deviation and mean of the ratio-image intensities, respectively, and are calculated as:

$$\sigma_R = \frac{1}{N}\sum_i (R(i) - \mu_R)^2 \tag{7}$$

$$\mu_R = \frac{1}{N}\sum_i R(i) \tag{8}$$

$$R(i) = \frac{B'(i)}{A(i)} \qquad \forall i \in \wp \tag{9}$$

Woods (Woods et al. 1992) originally proposed this method for brain registration of PET images, which tends to fail without previous segmentation of non-brain regions, i.e. bone, skin and background.

1.5.4.d. Partitioned Intensity Uniformity (PIU)

Shortly after, (Woods et al. 1992) also proposed an extension of the RIU method to work on brain PET-MR images. Because the biological meaning conveyed by the voxel intensities of images is different between modalities, the linear relationship of voxel intensities is lost in multimodal image registrations. However, there still exists a correspondence of the intensity values between images that is highest when images are perfectly aligned. In other words, voxels with intensity *a* in image *A* belonging to a given tissue will correspond to voxels with intensity *b* in image *B*' belonging to the same tissue. This intensity correspondences can be plotted in a histogram for each intensity value *a* in image *A*. Such histogram will show the intensity distribution of voxels in *B*' that are co-localized with intensity value *a* in image *A*. Implicitly, the total number of histograms will correspond to the total number of intensity values in image *A*. At true alignment, the number of intensity correspondences between images will be maximal for those voxels belonging to the same tissue. In addition, these correspondences will be distributed within a narrow range of intensities in image *B* belonging to a given tissue represented by intensity value *a* in image *A* (Fig. 5). At misalignment, voxels belonging to a given tissue in image *A* will overlap voxels belonging partly to the same tissue in image *B* and partly to other tissues, as well. In this case, image *A* voxels with intensity *a* will co-occur with a wider range of intensity values of voxels representing the overlapping tissues in image *B*. Therefore, histograms will show sharper and larger modes the more accurate the alignment and, multiple and

broader modes the larger the misalignment. PIU aims at minimizing the CV calculated over those histograms. Such CV is though weighted by the number of voxels in image *A* associated to each histogram. PIU is calculated as:

$$PIU = \sum_{a=1}^{N} \frac{n_A(a)}{N} \frac{\sigma_{B'}(a)}{\mu_{B'}(a)} \qquad \forall a \in \wp \tag{10}$$

This method fails when the correspondence of intensity *a* in image A generates a histogram where the intensity distribution of voxels co-located with intensity *a* generates two (or more) modes. As explained above this situation may occur when one tissue in image *A* represented by the intensity value *a* co-occurs with two tissues represented by different intensities in image B. In this situation, minimization of PIU leads to an erroneous registration and outputs a spatial transform that produces the sharpest and largest two (or more) histogram modes. Here again, removal of regions reduces the likelihood of bi- or tri-modal histograms.

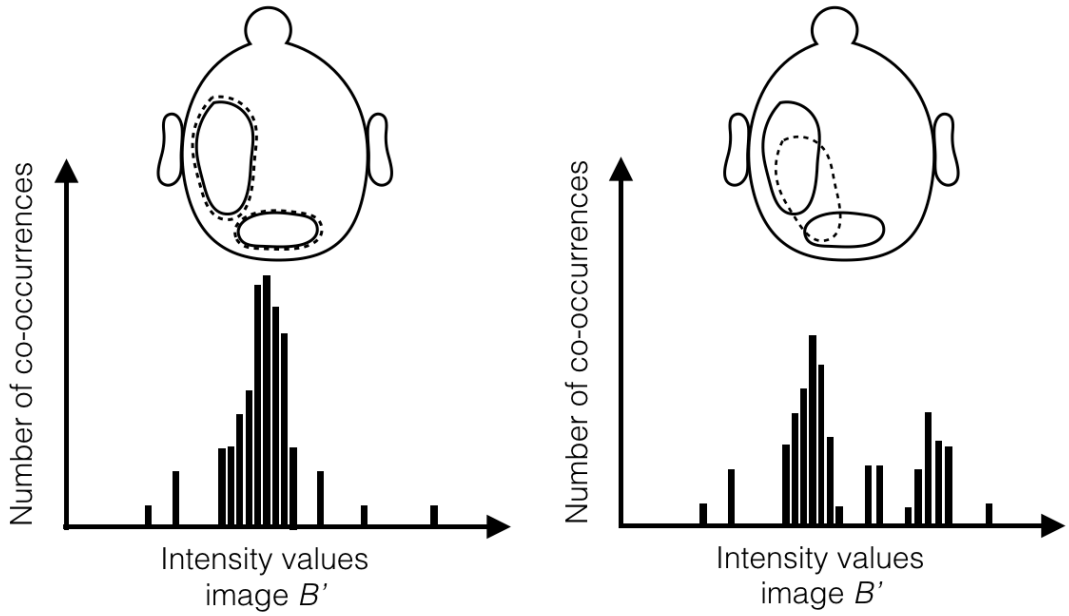

Figure 5. Schematic representation of the histogram intensity distribution of voxel co-occurrences in the transformed image *B'* with a given tissue intensity value in the reference image *A*. On the left, under tissue alignment the intensity correspondence between tissues is highest and a large monomodal peak is observed in the histogram. On the right, misalignment causes the tissue intensity value in the reference image to co-occur with intensity values of the same and a different tissue in the transformed image. Intensity correspondences between tissues at misalignment produce a more dispersed histogram, a smaller peak of the mode given at true alignment, and secondary peaks stemming from the intensity correspondences of one tissue in the reference image with other tissues in the moving image.

1.5.4.e. Information measures

The PIU approach revealed the usefulness of joint histograms as compact and visual representations of the intensity correspondences between images. As mentioned above, a histogram of image *B*' voxels co-localized with voxels in image *A* with a given intensity can be calculated for each of the intensity values in image *A*. If all histograms are orderly stacked according to intensity in image *A*, this results in a two-dimensional joint histogram of the intensity correspondences between images. The y-axis of the joint histogram will represent the intensity values in image *A* and the x-axis will represent the intensity values in image *B*'. The information conveyed in the joint histogram is the number of voxel co-occurrences of intensity pairs (a, b). Because in practice tissues are not represented solely by a single intensity value but for a range of values, and the number of intensity levels in medical images can be as high as 2^{16}=65.536, the dynamic range of image intensities is grouped in intensity partitions or levels. The notation $n_A(a)$ refers to the number of voxels in image *A* with intensity partition or level a, $n_B(b)$ being its analogous for image *B*. The most common number of levels *N* used is 256, leading to joint histograms of N_A x N_B = 256 x 256 cells. However, this number could be optimized for each registration problem, as suggested in (Hahn et al. 2010).

At true misalignment, the number of voxels with intensity levels pertaining to a given tissue in image *A* that overlap voxels with intensity levels pertaining to the same tissue in image *B* is highest. Such voxel intensity co-occurrences form a cluster of bright points over a dark background, i.e. low or no co-occurrences, in the joint histogram (Fig. 6). The number of clusters is, therefore, dependent on the number of tissues and their intensity contrasts. The rest of cells in the joint histogram where intensity co-occurrences are low or are not given at perfect alignment take values close to zero or zero. With increased misalignment the number of co-localized voxels pertaining to the same tissue in both images declines. This lost of co-occurrence results in a dispersion of the clusters with some of these counts being spilled out to the background area of the joint histogram. Alignment quality is therefore related to clusters' density or dispersion. By normalizing the joint histogram to the total number of overlapping voxels, an estimation of the joint probability distribution function (PDF) of the intensity co-occurrences between the images is obtained. In communication theory, the PDF of an information source describes the rate (how often) at which the expected messages (or symbols) are transmitted. And the Entropy (11) is used to characterize that information source as an average measurement of such rate distribution:

$$H(X) = \sum_{x=1}^{N_X} p(x) log_2 \frac{1}{p(x)} \qquad \forall x \in X \tag{11}$$

With *X* being the source (*image*) *x* the message (*intensity*), and N_x the number of possible transmitted messages (*intensities*) by *X*. Flat PDFs with equal rates for each possible message lead to high Entropy values

because the uncertainty of what message will be sent among the range of possible messages is highest. Conversely, sharp PDFs are typical of sources that send a reduced set of messages at a higher rate and a wide range of messages very sparsely. In this situation the Entropy is low since the messages are little informative to the receiver, which already expects to receive that reduced set of messages from that particular source. Notice that Entropy is an information measure sensitive to the dispersion of the messages probabilities conforming the PDFs of a source. In a joint histogram plotting the voxel intensity co-occurrences of two medical images, the joint Entropy can be understood as an estimation of the average dispersion of images intensities co-occurrences. Intuitively, registration is accomplished through minimization of the joint Entropy of the images.

$$H(A,B) = \sum_{a=1,b=1}^{N_A,N_B} p(a,b) log_2 \frac{1}{p(a,b)} \quad \forall a,b \in \wp \tag{12}$$

Entropy becomes a powerful estimator of image alignment quality because it overcomes PIU limitations in terms of handling multiple histogram modes and the need for pre-segmentation is much reduced. Such advantages are of utmost relevance in automated medical image registration. It is worth further justifying the appropriateness of the joint Entropy as an excellent estimator of image alignment. Take the case of two identical images that are perfectly aligned. All tissue voxels have the same intensity value in both images. Consequently, intensity co-occurrences are distributed along the symmetry axis in the joint histogram (Fig. 6, row *a*, first column). Therefore, the PDF of the joint histogram is exactly the same as the PDF of any of the images. By extension, the joint Entropy is the same as the entropy of any of the two identical images, which means that there is no added uncertainty in the "*registration*" system. Preserving the integrity of the images, only misalignment could add uncertainty to the system and increase the overall joint Entropy. The same reasoning holds for multi-modal images.

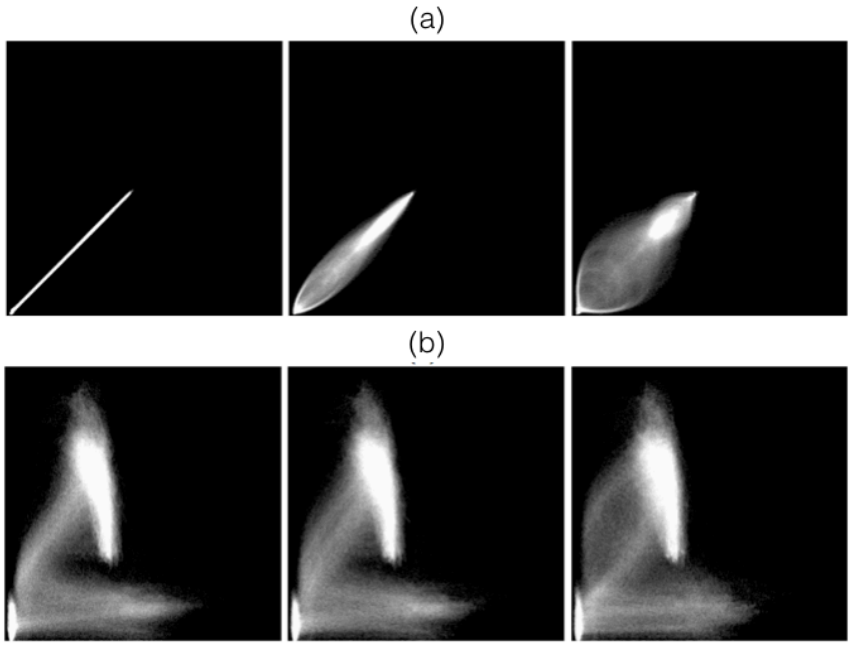

Figure 6. Intensities from the reference image are plotted along the horizontal axis, and those from the moving image on the vertical axis. In row (a), reference and moving images are identical MR images of the head. In row (b), the reference image is an MR image of the head, and the moving image a PET image of the head. For all modality combinations, the histograms are calculated for three different transformations: the identity (left), a lateral translation of 2 mm (centre) and a lateral translation of 5 mm (right) (Fitzpatrick et al. 2000)**.**

Despite marking a turning point in multimodal imaging, the joint Entropy underperforms when the background-to-object FOV of the images is large. Under these circumstances a global minima of the joint Entropy occurs in alignments with highly overlapped backgrounds. When image background occupies a larger volume in the images FOV than the objects of interest, background co-occurrences have a larger weight on the calculation of the joint Entropy. Background-to-background coincidence weighting was tested in (Hahn et al. 2010) on the RIRE dataset and better accuracies, but only in combination with other parameter adjustments and for a subset of imaging modalities.

(Studholme, D. L. G. Hill, et al. 1999; Wells et al. 1996; Maes et al. 1997) came to a slightly different explanation of the joint Entropy's Achilles' heel. These authors reasoned that *since the joint Entropy is estimated from the voxels falling in the overlapping images field of view*, minimization is accomplished when the spatial transform produces an overlap of the images containing the least information, not necessarily the most corresponding information. This statement would explain that a common registration outcome of the joint Entropy is the alignment of image background portions, producing a joint histogram with the least possible information, i.e all voxel intensity co-occurrences congregated in one cell. To overcome this limitation (Maes et al. 1997; Wells et al. 1996) proposed to maximize the mutual information (MI) between the images, instead. The MI can be expressed as:

$$MI(A,B) = H(A) + H(B) - H(A,B) \quad (12)$$

And, it can be understood as the amount of shared information between images. MI formulation implies that the joint Entropy variability associated to varying FOV between images during the optimization process is counteracted by the variability of the image marginal Entropies, also calculated from the overlapping FOV. Furthermore, the MI also compensates entropy variability associated to images interpolation during optimization process. Its superior results and wide applicability, established MI as the gold standard of multimodal registration. In spite of this, when the incremental variation of marginal entropies exceeds the reduction of the joint Entropy, MI may converge to a wrong solution. Other authors (Studholme, D. L. G. Hill, et al. 1999) observed that an alternative equation to counteract the variability of the Entropies involved in the MI calculation was to normalize the overall variation of the marginal Entropies by the joint Entropy.

$$NMI(A,B) = \frac{H(A)+H(B)}{H(A,B)} \quad (13)$$

This heuristic approach can be more generally applied than MI (Fitzpatrick et al. 2000), but the wide variety of medical registration problems explains that both methods are used.

1.6. Limitations

An overview of the most relevant registration methods has been laid out with special emphasis on rigid-body registrations of multimodal images of the brain. Since early 1990s, the vast majority of work accomplished in medical image registration has been to improve robustness. Recall that sub-voxel registration accuracy was accomplished with early point-based methods and that both surface-based and intensity-based methods emerged to expand the applicability of automatic registration while minimizing the need for user interaction. Intensity-based methods and, in particular reference information-based methods, are presented in the literature as accurate and robust methods for image registration. However, their performance is challenged when there is reduced overlap between the images and when applied to small-animal brain imaging associated to limited resolution systems and larger magnitude IIH and PVE artifacts, as further developed below.

1.6.1. Capture range

Certainly, intensity-based methods accomplish sub-voxel accuracies (West, J. M. Fitzpatrick, et al. 1997; Hahn et al. 2010) but their capture range or maximum admitted translational and rotational misalignment is restricted to 40 mm and 20º, respectively, for human brain images (Knops et al. 2006; Liu & Tian 2007;

Yokoi et al. 2004). This capture range is still unsatisfactory if it is considered that on one side, 40 mm misalignment is approximately a 12,5% of the typical adult head image sagittal and coronal dimensions (West, J. M. Fitzpatrick, et al. 1997); and on the other side, the adult average brain width and length are about 150 mm, four times the capture range of gold standard information-based methods. Not surprisingly, initial images misalignment in clinical and research applications easily exceeds MI and NMI capture ranges. Because MI and NMI are calculated over the images FOV intersection, calculations rely only on a few voxels at misalignment ultimately producing poor entropy and spatial transformation estimates. This problem was not unnoticed by the medical imaging community and principal component analysis (PCA) (Arata et al. 1995; Dhawan et al. 2002) or the method of moments (MoM) (Faber & Stokely 1998) were proposed as pre-registration methods. The aim of these methods is to produce an initial spatial transformation estimate that maximizes the overlapping volume between images. Both methods estimate the principal axes of the image intensities as the eigenvectors of the image intensities covariance matrix. Registration is accomplished by aligning the (three) principal axes between the images. While these methods secure some overlap between images, such overlap does not necessarily dispose the images within the capture range of MI or NMI for two reasons. One, principal axes directions of the intensities corresponding to the images regions of interest may be shifted by the effect introduced by artefacted image regions. It is the case of MR intensity artifacts affecting the skull due to loss of static field homegeneity at the edges of the image FOV. As a result, axes alignment does not necessarily imply anatomical structures alignment. Second, these approaches are highly sensitive to the images FOV. Paradoxically, performance of these methods is sub-optimal provided the objects to be aligned fall within the overlapping images FOV (Hill et al. 2001). These reasons explain why pre-segmentation is usually necessary for these methods to produce acceptable results (Maintz & Viergever 1998). Therefore, it seems reasonable to conclude that **there is a void of registration methods that effectively and accurately align medical images with partial FOV overlap between them**, a common problem in clinical and research applications.

1.6.2. Acquisition artefacts

Besides the capture range limitations of gold standard NMI, intensity artifacts inherent to the imaging technique may also affect registration. In this Thesis, special attention is given to the intensity inhomogeneities observed in small-animal brain MRI and the partial volume effect (PVE) in brain PET imaging.

1.6.2.a. MR intensity inhomogeneity in small animal imaging

IIH distortion was previously introduced in section *1.4.1. Rectification* in regard of the use of non-rigid intensity maps to correct for the spatial displacement of some part of the image caused by the artefact. IIH

inhomogeneities discussed here appear like a shadowing effect on the anatomy with no spatial displacement involved. Special focus is given here to its detrimental effects in small-animal brain MR-PET registration. As a clarifying note, PET imaging is free from this kind of intensity distortion.

MRI physics: sources of intensity inhomogeneity artefact

The basic principles underlying (nuclear) MR imaging physics consist in (eq. 1) delivering radiofrequency energy to the body, (2) that will be absorbed by atomic nuclei composing body tissues, (3) to partly re-emit such energy sensed by the MR coils through signals with time and frequency signature characteristic of the tissues being imaged.

Matter is composed by atoms arranged in molecular configurations that ultimately compose macro structures, like human body tissues. Protons are positive charges confined in the atom nucleus that spin on their axis due to thermal energy of the medium, originating a magnetic moment μ [J/T] (Fig. 7). In atoms having an odd number of protons, the resulting magnetic moment of the atom experiences a tilt, inducing an angular momentum J [J/Hz]. The ratio J/μ is known as the gyromagnetic ratio γ [Hz/T], is particular of every nucleus and a fundamental property to enable MR imaging.

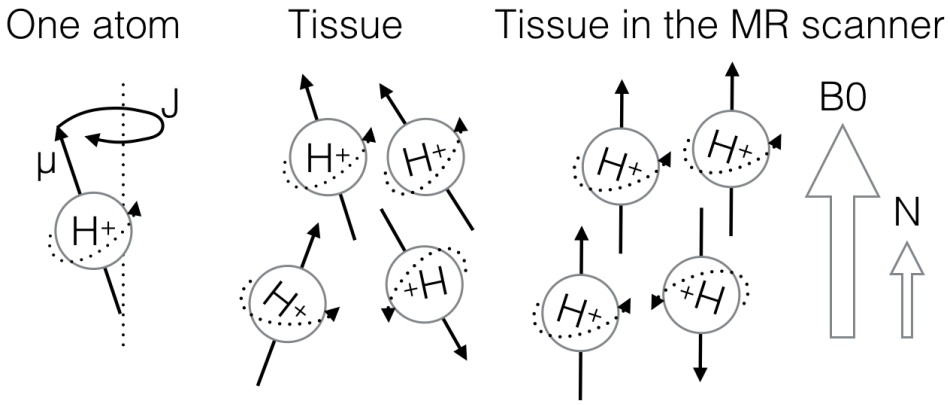

Figure 7. (Left) Magnetic and angular moment of a hydrogen spin. (Middle) Random distribution of spins in normal conditions. (Right) Magnetic alignment of spins with externally applied static field.

Because the direction of μ can be considered a uniformly distributed random variable, the net magnetization (M [J/T]) of all spins is negligible. However, when subjected to an external field B0, spins align with and agains the direction of B0 generating non-negligible M (Fig. 7). The larger B0's magnitude the more spins will align with the direction of B0 and the larger M (Zeeman effect, (Zeeman 1897)). The external magnetization of the system, i.e. tissues, induces a change in the spin velocity or rotational frequency that follows the relation:

$$\omega_L = \gamma \times B0 \tag{14}$$

Consequently, the larger B0 the faster the rotational frequency of the spin (ω_L, [Hz]), named Larmor frequency after Joseph Larmor. Due to its abundance in the body, MR scanners are designed to target hydrogen spins and produce high-SNR images, i.e. high M. Current clinical MR scanners work at 1.5T or 3T inducing a Larmor frequency to hydrogren spins (γ = 42.58 MHz/T) of 63.87 MHz or 127.74 MHz, respectively.

Once spins are aligned with B0, a radiofrequency signal (RF) is sent to the body and abosorbed by the spins, which tilt from the B0 axis at an angle that depends on the excitation time and RF frequency. At this point, spins also rotate about the B0 axis and also at the Larmor frequency, a phenomenon known as precession. When the pulse emission ceases, spins gradually release the absorb energy in the form of an oscillating signal at the Larmor frequency. At 90º tilt, the emitted signal is maximal and decays at a rate that depends on the degree of interaction between tissue spins. This signal is termed free induction decay (FID) and the time constant that determines the rate of decay is called T2 (Fig. 8).

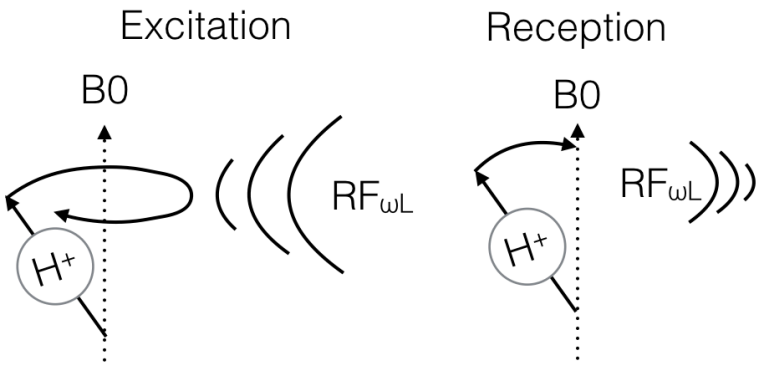

Figure 8. (Left) RF excitation at the Larmor frequency implying precession in the excited spin. (Right) Relaxation or energy status recovery of the spin by means of RF emission also at the Larmor frequency.

However and because precession, the recovery of the spin alignment with B0 can be deaggregated into a transversal (T2) and a longitudinal (T1) component. Tissues with low spin-to-spin interaction, such as cerebrospinal fluid, have have long decay times and appear bright and dark in T2-weighted and T1-weighted images, respectively (Fig. 9). Tissues with high spin-to-spin interaction, such as bone, have short decay times and, therefore, show bright and dark in T1-weigthed and T2-weighted images, respectively. Gray and white matter have intermediate spin-to-spin interaction and show gray with less contrast between them in either modalities.

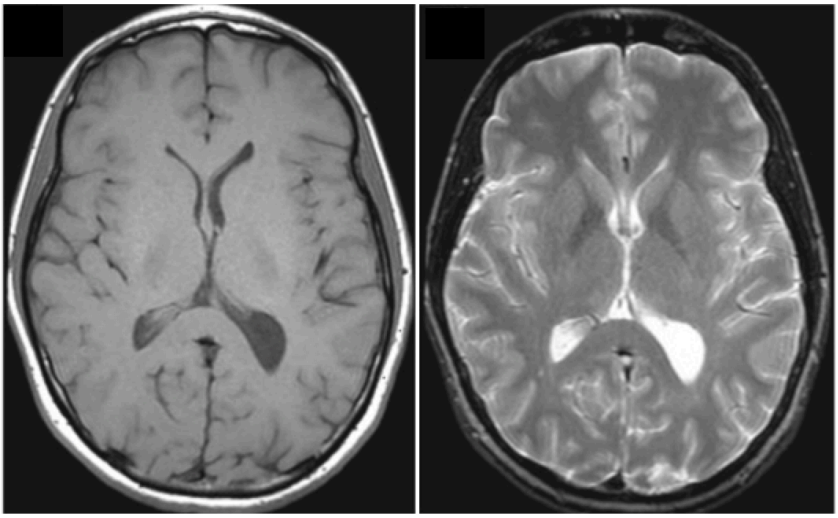

Figure 9. T1- (left) and T2-weighted (right) images of the adult brain.

Because the FID generated by all tissue spins has the same Larmor frequency, the spatial localization of spins belonging to different tissues to conform an image is not yet possible. Spatial localization of tissue spins is accomplished by coding their Larmor frequency with respect to their physical position. Gradient coils are used to linearly increase or decrease B0 along the three-volume axis and, as a result, change the Larmor frequency of spin "packets" throughout the imaged FOV. Only those spins rotating at the frequency (spatially coded) emitted by the RF field will *resonate* and precess. After rastering the entire FOV the system has recorded (in the *k*-space) the received energy from each spatial location. Finally, the image can be recostructed by inverse-Fourier transforming the data.

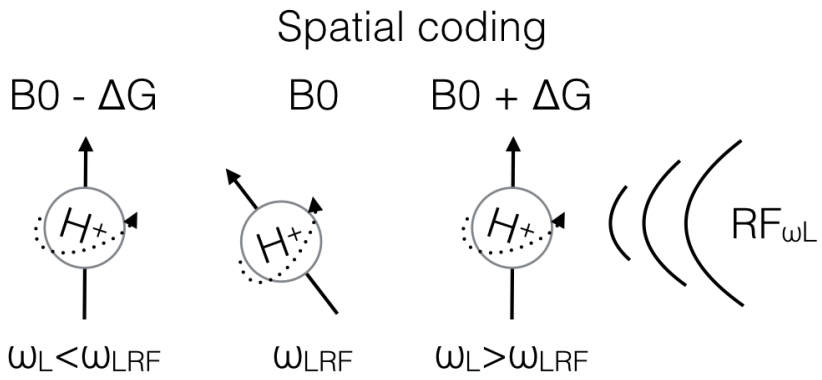

Figure 10. Spatial encoding by means of gradient coils slightly increasing and decreasing the Larmor frequency of neighbour spins. Only spins precessing at the Larmor frequency will resonate to the RF signal.

$$\omega_L = \gamma \times (B0 + \Delta G) \tag{15}$$

Sources of intensity inhomogeneity

Accurate magnetization of the imaged FOV is key to spatially locate spins precessing at coded and known Larmor frequencies. When deviations in the coded magnetization map occur, spins located in non-targetted neighbour positions may be excited, precess, and contribute to the FID that would be attributed only to the targeted position. Such deviations or intensity inhomogeneity may be caused by (Collins et al. 2005; Vovk et al. 2007; Sled & Pike 1998; Lewis & Fox 2004):

- Inhomogeneity of the static field B0
- Non-uniform RF field excitation
- Non-linearity of the gradient coils
- Non-uniform sensitivity of the receiving coils

As well as by:

- Patient/subject/animal loading or disruption of the MR induced magnetization

Impact of intensity inhomogeneities in small-animal brain MRI

Though IIH usually does not interfere with diagnostic procedures, it may seriously hamper research studies where quantification pre-processing steps, e.g. segmentation and registration, which rely on the intensity distribution of the image, are routinely done. MRI inhomogeneity correction is thus necessary for accurate quantification of the human brain. A more challenging scenario is found in pre-clinical studies working with small animals, e.g. rats or mice. In this context, the inhomogeneity correction results far from trivial for two reasons: One, the field magnitude of small animal MR scanners (1.5 to 14 Tesla) is noticeably larger than that of human MRI scanners (0.5 to 3 Tesla). As a result, field inhomogeneities drift away more disruptively tissue intensity values in the image (Fig. 11). And two, the amount of structural information, i.e. tissue folding, of a mouse brain image is considerably lower than in the human brain, what means that lower spatial information is available for registration purposes. This fact can be observed in the larger number of histogram intensity modes of human than small-animal MR images (Fig. 11, bottom row). In other words, the intensity distortion introduced by a given artefact magnitude results more detrimental in the rat or mouse case. Unfortunately, IIH correction methods for human brain MRI are not directly applicable to small-animal brain MRI, where the artefact is more pronounced. In this Thesis, the widely used IIH correction method proposed by (Likar et al. 2001) for human brain MRI is incorporated in an iterative correction-registration approach to extend its applicability to small-animal brain MRI.

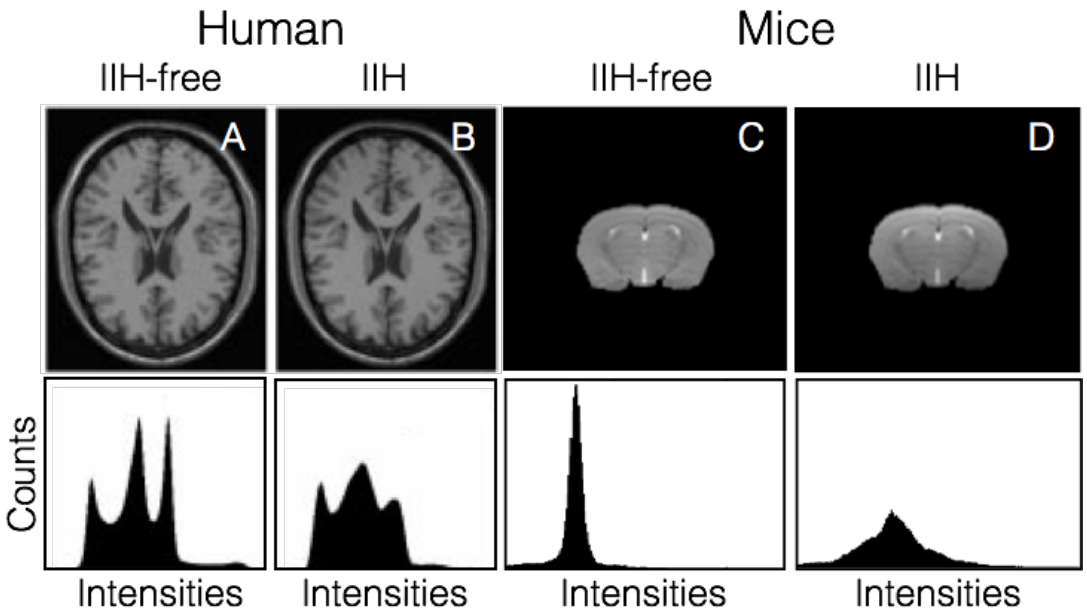

Figure 11. Impact of MR intensity inhomogeneities in human and mice brain images. On the top row human brain IIH-free (A) and IIH-affected (B) MR images, and mice brain IIH-free (C) and IIH-affected (D) MR images are shown. On the bottom row, their respectives intensity histograms are shown. For mice images, background pixels are not included in the histogram.

1.6.2.b. Partial Volume Effect in PET

PET is a type of nuclear imaging technique that is extremely sensitive to biological processes occurring in concentrations as low as 10^{-11} - 10^{-12} moles per litre, several orders of magnitude more sensitive than MRI (10^{-3} - 10^{-5} mol/L). However, PET resolution is much reduced by the nature of the nuclear and acquisition processes attached to the technique.

PET imaging consists on measuring the amount of electromagnetic radiation produced by a radioactive compound, i.e. a radiotracer, which has been intravenously inserted into the patient. The radioactive compound, radioisotope or radionuclide is designed to attach onto a molecule of interest and to trace the behaviour of this molecule under certain conditions. Radioisotopes used in PET are energy-unstable compounds whose atoms release excess of energy in the form of positrons and neutrinos until nuclear and electrostatic atomic forces reach balance and stabilize.

Neutrinos are massless and chargeless and are useless for PET imaging. It is *positrons emitted* by the radioisotope that originate the cascade of processes that enables imaging. After emission, positrons travel 2-3 millimetres from the nucleus and necessarily interact with electrons of neighbour atoms changing this their direction and slowing them down. The distance a positron travels from the nucleus to the point it looses

(almost) all of its kinetic energy is known as the positron range. At this point, the positron collapses with an electron of another atom in a process known as annihilation (Fig. 12).

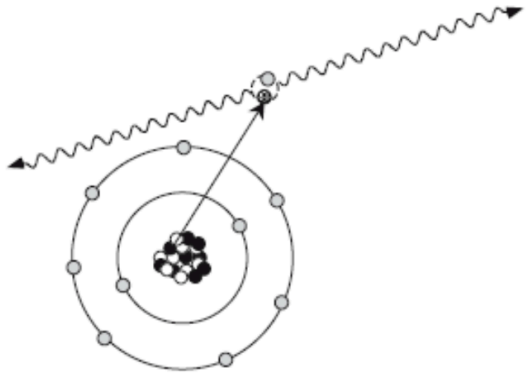

Figure 12. Schematic representation of the positron range and the annihilation process.

In the annihilation process, the mass of either particles is converted, by means of Einstein's equation $E = m \times c^2$, into electromagnetic energy. This energy takes the form of two 511 keV photons (gamma energy band) that are colinearly released in opposite directions from the annihilation point. Actually, if the proton has not lost all of its kinetic energy, annihilation does meet colinearity, and photons might be launched in different directions. The longer the path (or line of sight, LOS) to the scanner detectors, the larger the divergence is from the expected co-linear path. Importantly, it is these two photons that are captured by PET detectors (Fig. 13) and not the emitted positrons. Then, captured LOS can be back projected to reconstruct the image.

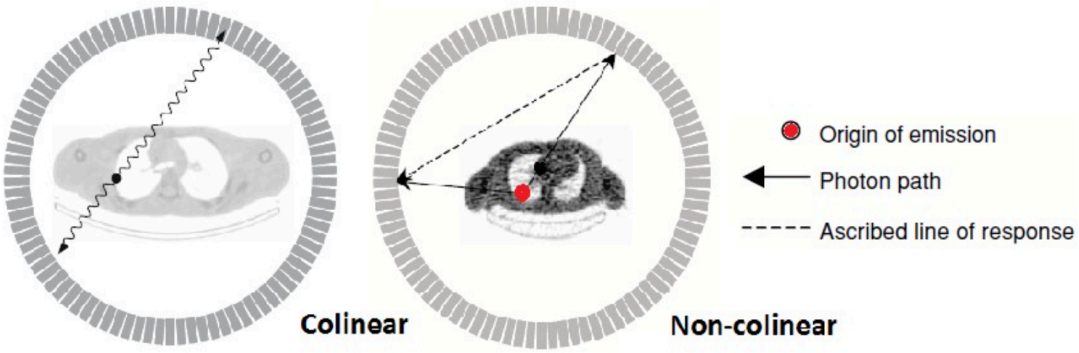

Figure 13. On the left, the expected linear annihilation response is shown. On the right, non-colinearity occurs when the positron kinetic energy has not been completely lost before annihilation to an electron.

Photons non-colinearity and the positron range are clearly the two main factors affecting image resolution. On one side, non-colinear LOS, usually 4-6 mm from the true annihilation point, will misplace biological

information introducing a blurring effect in the neighbourhood of the annihilation point. On the other side, the positron range will also generate a LOS (co-linear or non-colinear) occurring 2-3 mm from the true annihilation position, spilling out biological information to neighbouring regions. As a result, the biological information originated in a given tissue *volume* is *partially* attached to neighbouring tissues giving name to *the partial volume effect* (PVE). Current PET systems have an overall resolution close to 5 mm (Vandenberghe et al. 2016). The most determining factor in human PET PVE is highly determined by the non-colinearity effect due to the larger paths photons need to travel to reach the gantry (or ring) detectors (Fig. 13). In small animal imaging (Fig. 14), it is the positron range that most hinders image resolution, about 1 mm in current systems (Marcinkowski et al. 2016). As opposed to previous solutions requiring pre-segmentation of the images and information of the PET scanner resolution specifications, approaches based on Mutual multiresolution analysis (MMA) have been recently proposed offering an alternative and promising framework (Boussion et al. 2005). MMA principally relies on the structural information of previously registered anatomical images to correct for PET PVE, although currently proposed solutions still rely on PET scanner specifications and are highly parameterized (Kim et al. 2013; Shidahara et al. 2009). In this Thesis, MMA is explored and a novel simple and purely data-driven PVE correction method relying on a multimodal energy equalization analysis is presented.

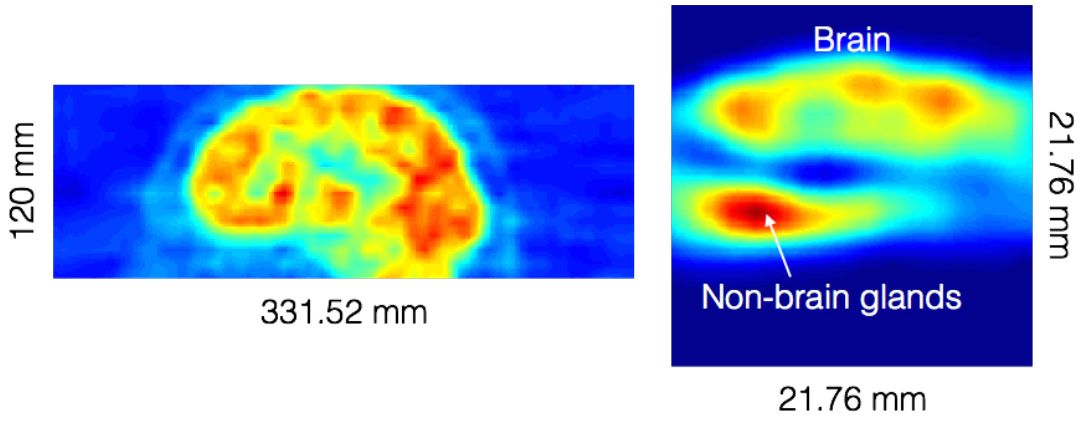

Figure 14. Resolution comparison between human and mice brain 18F-FDG PET images.

2. Motivation and objectives

2.1. Motivation

Much of the work that I personally conducted in the pre-clinical image analysis department of a molecular imaging centre was associated to quantification and, by extension, to accurately registration of rat and mice brain images of different modalities, mostly PET and MR. One of my objectives was to automate the quantification process as much as feasible to achieve highly reproduceable and efficient ROI delineation on highly diffused mice brain PET images. Apart from timing considerations, automatic quantification reduces user/operator errors and makes quantification accessible also to non-imaging experts. The key process to automate is registration because after image alignment the necessary ROIs can be manually drawn only once on the averaged or template image in the absence of an atlas including the target ROI under study. However, registration robustness is very much dependent on the degree of overlap between images. The current reference method for multi-modal human and small-animal brain registrations is the NMI but fails in case of partial FOV overlap and requires either time-consuming manual pre-registration or automatic pre-registration not always providing satisfactory results and not easily implementable for the clinical or inexpert user. Since conception of the NMI in 1999 (Studholme, D. L. G. Hill, et al. 1999), a great amount of work has been produced oriented to either increase its accuracy by introducing anatomical information into the calculation (Gan et al. 2008; Liu & Tian 2007) or to optimize other processes involved in the registration algorithm, such as image interpolation (Hahn et al. 2010; Tsao 2003), histogram binning (Knops et al. 2006; Hahn et al. 2010), or the searching algorithm (Maes et al. 1999; Das & Bhattacharya 2010). However, the surveyed literature shows that little advances have been made that truly improve NMI's capture range. The basis of this thesis relies on the exploitiation of the images information to improve, particularly, registration robustness but also as a framework to develop novel methods that correct for imaging-dependent artifacts that challenge accurate registration. **In this Thesis, it is proposed to exploit the non-overlapping FOV of the images to improve the capture range of gold standard NMI of multimodal human and mice brain image datasets. It is also proposed to use such improvement and further exploit the shared images information for the development of novel correction methods of MR IIH and PET PVE arteficts**.

2.2. Objective

The main objective of this Thesis is **to improve the robustness of the reference registration method, the NMI, against reduced FOV overlap of multimodal human and mice brain images through exploitation of the non-overlapping FOV information of the images**. It is also the purpose of this Thesis to apply such exploitation of the images information to propose novel methods for correction of MR IIH and PET PVE. The specific objectives attached to the main goal of the Thesis are listed below:

1. Implementation of the novel registration method including the non-overlapping FOV images information into the calculation of the NMI and evaluation of its performance on multimodal human and mice brain as compared to gold standard NMI.
2. Implementation of an iterative IIH-correction - registration method of mice brain MR images that exploits the joint images information to ultimately produce more accurate registration and quantification results as compared to the standard strategy.
3. Implementation of a PVE correction method for PET images that utilizes the high frequency content of an anatomical registered image pair and that is independent of its imaging modality.

2.3. Document structure

An introduction to medical image registration focusing on multimodal brain imaging has been presented in chapter 1. The most relevant registration methods have been explained paying special attention to concepts, e.g. multiresolution optimization strategy or MR rectification, which will be addressed from chapters 3. The chapter closes with the presentation of NMI as the gold standard registration method and its limitations.

Chapter 2 opens with the motivation underlying the present work and continues with specific definition of the objectives to be accomplished.

A novel registration method that overcomes the limitations explained earlier is presented in chapter 3. Background on information measures used for medical image registration is provided and next, the evaluation datasets are described as well as the evaluation methods. Superior results are observed with the novel method in terms of capture range for all registration problems for both human and mice brain datasets.

Chapter 4 introduces a novel MR intensity inhomegeneity correction method based on iterative multimodal registration. It follows describing the limitations of human brain MRI IIH correction methods to find application in small-animal brain MR datasets. Next, the theoretical background of the proposed method relying on the exploitation of image information introduced in Chapter 3 is justified. Comparative results between methods show improvement in both registration and quantification accuracy for an MR-PET mice brain dataset.

Following, chapter 5 addresses the PVE inherent in PET imaging and gives an overview of the state-of-the-art correction methods. A novel method utilizing a mutual multiresolution analysis that relies on accurate image alignment is described. The human and mice brain data used for evaluation is listed and next,

qualitative and quantitative results are presented and discussed. It is concluded that the novel method offers ample opportunities for improvement and exploration of other alternatives for PVE correction.

The conclusions of this Thesis are included in chapter 6, followed by future research work in chapter 7, and publications derived from the actual work in chapter 8.

3. Registration of multi-modal neuroimaging datasets by considering the non-overlapping field of view into the NMI calculation

3.1. Introduction

Fundamentally, NMI relies on a significant initial overlap between the image pairs. This requirement has compelled many authors to use complementary processes of rough alignment before running an NMI co-registration, for the NMI cannot guarantee a successful registration for reduced overlap between the images. Fiducial registration overcomes such limitation and produce highly accurate results but they also need advanced registration planning, intensive user interaction, can be invasive, and are attached to significant procedural time. For these reasons, the use of these methods is largely limited to neurosurgery where intra-operative images, such as U/S, are registered to pre-operative images, e.g. MR, to guide surgery (Ji et al. 2008; Farnia et al. 2012). The method of moments (Faber & Stokely 1998) is also used for pre-registration purposes. These methods rely on the images intensity covariance matrix to obtain the principal axes of intesity variation, which are then used to align the images. Nevertheless, their results are commonly unsatisfactory due to their sensitivity to intensity artifacts and field of view of the images (Hill et al. 2001), and do not guarantee alignments within the capture range of NMI.

In this work, we propose an alternative algorithmic approach (SMI) that includes the non-overlapping field of view (FOV) of the images into the NMI estimation. By doing this, we overcome the high variability of the NMI estimations even in cases of little overlap between the images. Since all information in the images is exploited, we obtain a more stable and smoothly convergent NMI estimation that yields superior performance to the conventional NMI estimation in terms of robustness, capture range and prevention of local minima trapping. We have evaluated the performance of our approach in terms of success rate, capture range, FOV sensitivity – response to varying FOV of the images – and registration accuracy in two distinct datasets. On one hand, we have used the "Retrospective Image Registration Evaluation (RIRE) project" dataset consisting of 69 MR/CT and 36 MR/PET human image pairs. This dataset provides a ground truth for estimating the final co-registration accuracy, which is calculated based on bone-implanted markers that were digitally removed prior to images distribution (West, J. Fitzpatrick, et al. 1997). On the other hand, we have used a small animal dataset consisting of 11 18F-FDG PET-MR mice image pairs. We have compared the performance of SMI against the standard implementation of the NMI in the Statistical Parametric Mapping (SPM) software, which is a well-known and widely-used package for statistical analysis of neuroimaging data including PET, SPECT, MRI and fMRI (Ashburner 2012). SMI outperformed NMI on success rate, capture range and robustness to varying FOV of the human and mice datasets. NMI produced more accurate results for PET-MR registrations and SMI for CT-MR registrations.

3.2. Estimation of information measures

Information-based registration methods (Studholme, D. Hill, et al. 1999; Collignon et al. 1995) have traditionally relied solely on the overlapping FOV $\wp = A \cap B$ to calculate images A, B shared information (Fig. 15). Because this overlap varies during the search of the translations and rotations that maximize the value of the information measure, so does the value of the image entropies. A major downside of these measures is that when the amount of overlap is reduced, image and joint entropies are not representative of the images information content. As a result, these measures produce an unstable and unpredictable behavior during the optimization process. For this reason, this strategy is bound to be trapped into local minima if images do not share enough information at initial misalignment. The performance of NMI has traditionally been evaluated with significantly overlapping images. In (Studholme, D. Hill, et al. 1999) a 30 mm translational and 30º rotational misalignment range was explored. Somewhat larger ranges (60 mm, 60º) were explored by (Pluim et al. 2004) in a complete comparison of mutual information-derived measures. In (Liu & Tian 2007) and (Yokoi et al. 2004) misalignments up to 20 mm and 40 mm were applied, respectively. However, the need of subjecting the NMI to a not uncommon wider misalignment range had not been satisfied yet (Yokoi et al. 2004; Itou et al. 2011). This is a relevant subject in clinical and preclinical image quantification and analysis of (large) medical datasets, which are often acquired from different scanners and therefore, with different spatial coordinate systems. If standard image processing tools cannot straightforwardly find alignment between the images, which is not rare, this process can turn very time consuming with manual alignment being usually required.

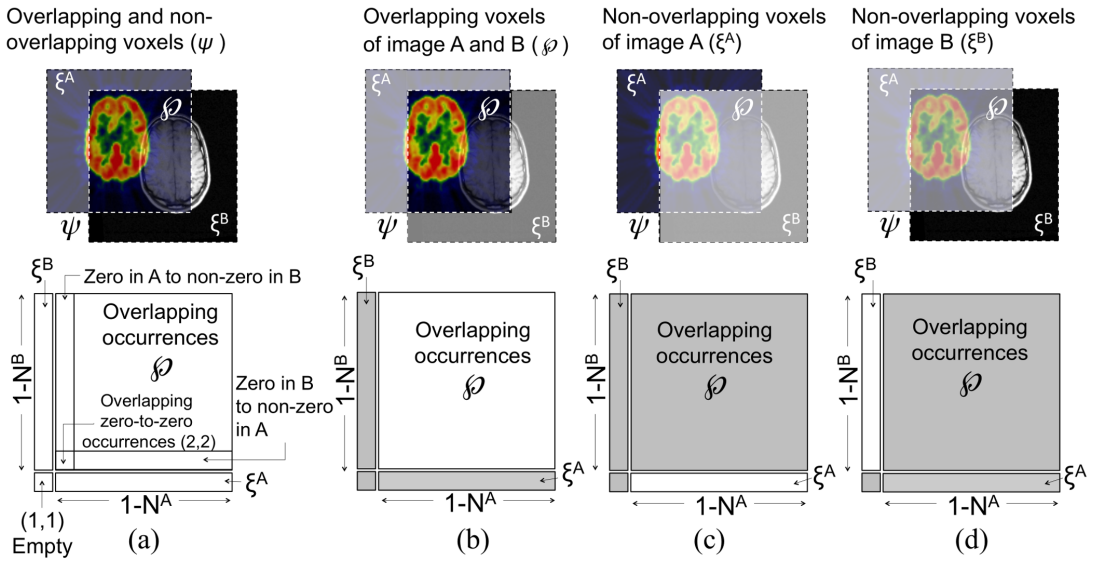

Figure 15. (a) On the top row, a classification of the overlapping and non-overlapping information in the image space provided by two misaligned images is provided. On the bottom row, the proposed modified version of the joint histogram including the overlapping and non-overlapping images information is shown. (b) Overlapping occurrences are highlighted in the image space and in the joint histogram. Non-overlapping voxels appear transparent in the image space and occupy grey areas in the joint histogram. (c) Non-overlapping voxels of image A (PET) are highlighted in the image domain and in the joint histogram. (d) Non-overlapping voxels of image B (MRI) are highlighted in the image domain and in the joint histogram.

To overcome such limitations, we propose to also include the information contained in the images non-overlapping space ξ and fully exploit the information contained in the images (Fig. 15). By doing so, the amount of information used for entropy calculations is constant through the iterative process. As a result, we hypothesize that more stable entropy estimations can be achieved independently of the degree of overlap. In addition, the information in ξ might provide a valuable indication of the degree of misalignment potentially leading to more robust registrations in cases of reduced images overlap.

Traditionally, the joint histogram used to register the image intensity coincidences (a,b) has been built from the overlapping domain ℘ (Skerl et al. 2006; Maes et al. 2003) (Fig. 15). In order to take into account the information contained in ξ the joint histogram can be extended with an additional row and column. Notice that this fact does not change the discrete intensity levels of the images (N_A, N_B), but increases its dimensions to (N_A+1) x (N_B+1) (Fig. 15a-d). Now the non-overlapping information in image A (ξ^A) and B (ξ^B) occupy the first row and column of the histogram, respectively. Therefore, cell (1,1) lacks of meaning since no co-occurrences are given for non-overlapping image regions and therefore, this cell is always empty (Fig. 15a). Intuitively, the histogram region binning overlapping occurrences spans from cell (2,2) to (N_A+1, N_B+1), with row (column) two registering all non-zero voxels in image A (B) that coincide with voxels in image B (A) of value zero. Finally, zero-to-zero co-occurrences are registered in cell (2,2).

The extended joint histogram can be implemented as follows: 1) First, the intensity co-occurrences in $\wp$ are binned from cell (2,2) to (N_A+1, N_B+1) (Fig. 11b). 2) Next, image A and B non-overlapping voxels – ξ^A and ξ^B– are binned into the first row and column, respectively (Fig 15c-d). At this point, the joint histogram registers all overlapping and non-overlapping intensity occurrences for the given images alignment. 3) Finally, the joint probabilities *p(a,b)* are estimated by normalizing the joint histogram to the sum of overlapping and non-overlapping occurrences.

3.2.1. Stable Entropies and NMI

Therefore, the information contained in our proposed implementation of the joint histogram is no longer that of the domain of the images intersection, $\wp$, but that of their union, $\psi = A \cup B$. Implicitly, the total amount of images information will not vary though the iterative optimization of the NMI. To differentiate conventional from proposed estimations, we have defined marginal and joint Stable Entropy (SH) estimators to ultimately calculate the Stable Entropies NMI (SMI), as this extended conception of the well-known and widely-used NMI.

Distinctly, our proposed version of the marginal Entropy excludes the first histogram bin from the marginal Entropy calculation, corresponding now to the non-overlapping voxel intensities of the counterpart image (Fig. 16). Image A and B stable entropies – SH(A) and SH(B) – can be formulated as

$$SH(A) = \sum_{a=2}^{N_A+1} p_A(a) log_2 \frac{1}{p_A(a)} \qquad \forall a \in A \tag{14}$$

$$SH(B) = \sum_{b=2}^{N_B+1} p_B(b) log_2 \frac{1}{p_B(b)} \qquad \forall b \in B \tag{15}$$

Likewise, the Stable Joint Entropy SH(A,B) is calculated as in (10) yet considering the new domain ψ:

$$SH(A,B) = \sum_{a=2,b=2}^{N_A+1,N_B+1} p(a,b) log_2 \frac{1}{p(a,b)} \qquad \forall a,b \in \psi \tag{16}$$

Next, an optimization scheme is used to find the spatial transformation that maximizes SMI:

$$SMI(A,B) = \frac{SH(A)+SH(B)}{SH(A,B)} \tag{17}$$

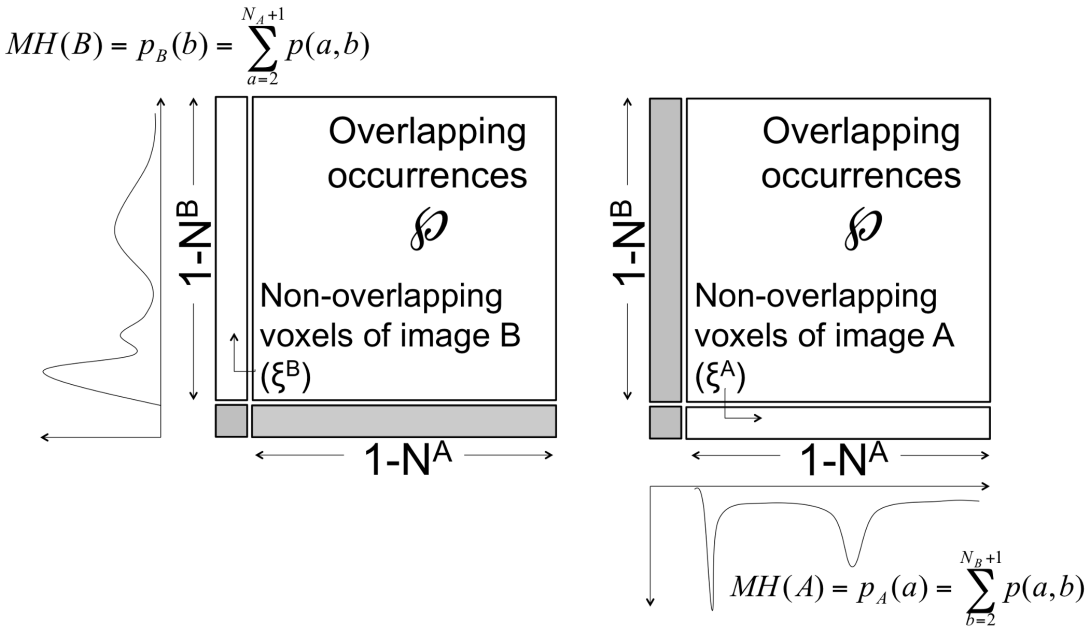

Figure 16. Image A (left) and B (right) histograms as calculated for SMI optimization. Because the first column and row contain non-overlapping voxels of image A and B, respectively, these should not be included in the histogram of their counterpart image. Hence, rows and columns two and beyond are summed to build the histograms of image A and B, respectively, leaving empty the first bin of both image histograms.

3.2.2. Entropy computation in a multiresolution framework

As introduced in section *1.3. Optimization*, medical image registration methods are usually implemented in a multiresolution framework to extend the capture range and speed of the registration method. For instance, two-step resolution registrations are implemented in SPM. Such registration strategy best combines the advantages offered by our proposed solution and those offered by the conventional NMI. By using SMI at the low-resolution level (Fig. 17), a solution producing high images overlap can be secured. At the high-resolution level, finer alignment should be accomplished by relying solely on voxels within regions of interest located in the images FOV intersection ($\wp$) excluding, thus, confounding and peripheral regions. While the joint Entropy is calculated from the joint images FOV in SMI at the high-resolution level, images entropies are still estimated from the full FOV of the images to reduce the effect of image entropy variations due to interpolation in the final solution. If the joint Entropy were to be estimated using the full images FOV at the high-resolution level, SMI optimization would find global optima where SH(*A*,*B*) would be minimum, but not necessarily implying true alignment, as discussed in section *1.5.4.e. Information measures* when pinpointing the limitations of Joint Entropy registrations.

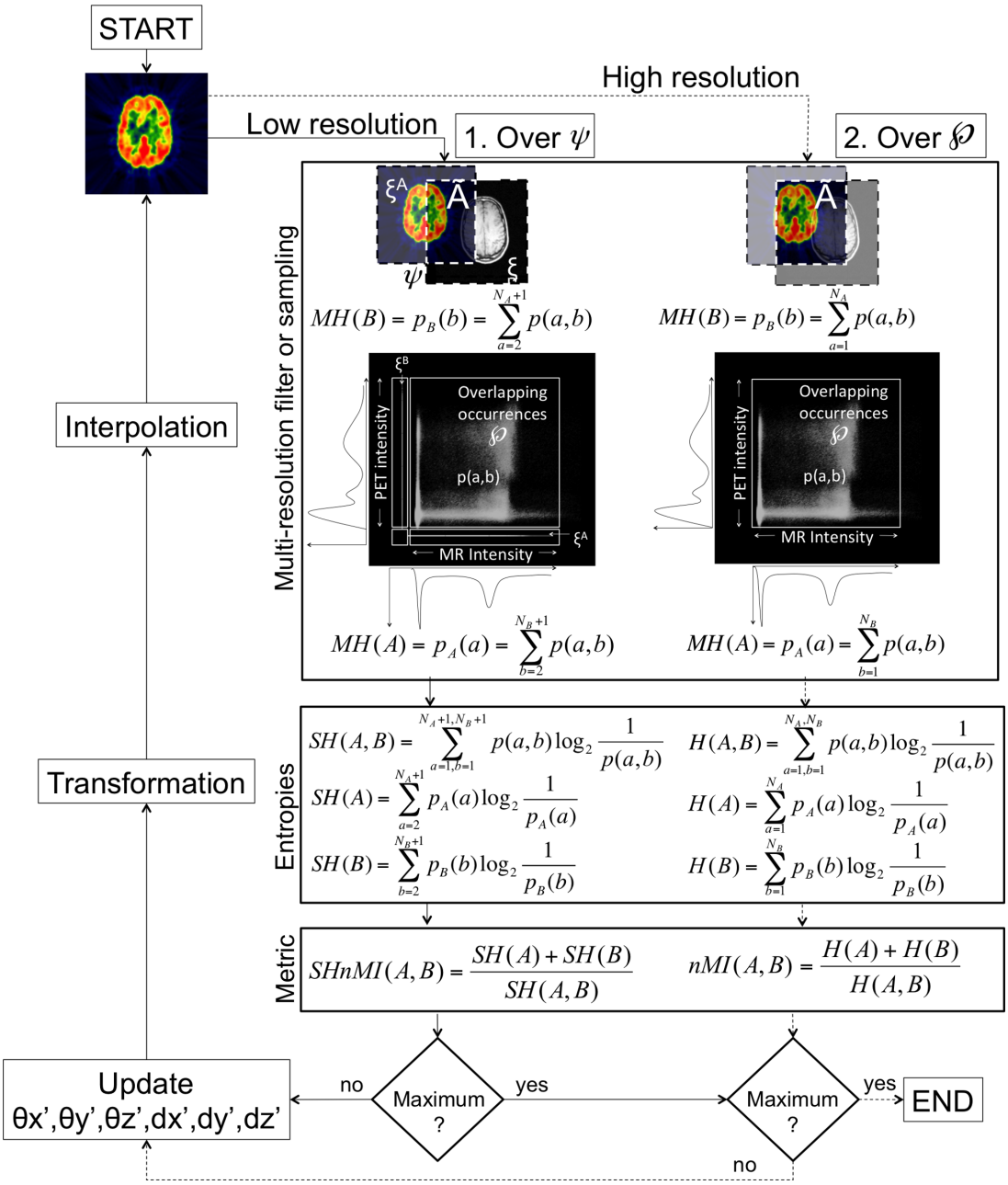

Figure 17. Registration steps within a multi-resolution framework. First, low-resolution version of the images (left branch of the multi-resolution filter stage) is used to accomplish coarse alignment. The algorithm is iterated until SMI reaches a maximum. Second, a higher sampling rate is used to obtain higher resolution images and accomplish fine alignment. In this stage, SMI is calculated by using only voxels in the overlapping area. Consequently, SMI calculation is equivalent to that of NMI. When NMI reaches a maximum, registration is complete.

3.3. Evaluation

3.3.1. Datasets

3.3.1.a. Human

In this study 42 MR/CT and 21 MR/PET image pairs of the RIRE human brain dataset were used. 20 of the MR (T1, T2, PD) images were corrected (or rectified, refer to section *1.4.1. Rectification*) for scanner-dependent geometric distortions and were tagged with the letter r. Ground truth registration was not publicly disclosed and obtained by means of fiducial markers alignment, which were digitally erased from the images previous to the distribution of the dataset. This dataset can be freely downloaded from the "Retrospective Image Registration Evaluation (RIRE) project" website (http://www.insight-journal.org/rire/). Registration errors are automatically calculated in the RIRE server after submission of a rigid transformation.

CT images present a voxel size of 0.65 x 0.65 x 4.0 mm with a matrix size of 512 x 512 in-plane pixels and between 28 and 34 slices. PET images have a voxel size of 2.6 x 2.6 x 8.0 mm (but for subject 005: 1.94 x 1.94 mm) with 128 x 128 x 15 matrix size. MR data had a nominal voxel size of around 1.25 mm with 256 x 256 in-plane pixels with 20 to 26 4 mm-thick slices (West, J. M. Fitzpatrick, et al. 1997). All patients had brain lesions occupying significant volumes of space, which were visible in one or more image modalities.

3.3.1.b. Mice

Animals (N=11) underwent MRI scanning in a Bruker BioSpin (Bruker BioSpin Corporation, 15 Fortune Dr, Billerica, MA, United States) device with a surface coil using a spoiled gradient-echo sequence (Echo Time = 8 ms; Repetition Time = 1500 ms), which provided T2-weighted images with a matrix size of 128 x 128 x 128 voxels of 0.17 x 0.17 x 0.17 mm in size.

Mice were scanned for 10 minutes in a microPET R4 scanner (Siemens Medical Solutions, Knoxville, TN, USA) after being injected with approximately 300 μCi 18F-FDG and after 45 minutes for tracer uptake. An OSEM 3D reconstruction (12 subsets, 2 iterations) was applied to the acquired data. The resulting FOV was of 1.8 cm and its spatial resolution of about 1.9 mm Full Width at Half Maximum (FWHM) (Popota et al. 2009). Images had a matrix size of 256 x 256 x 63, 8-bit quantization, 1.21 mm slice thickness and 0.42 mm in-plane pixel size.

Ground truth registration of the mice dataset consisted in manual alignment of all PET images to their respective MR pair.

3.3.2. Performance criteria

The performance of SMI against NMI as implemented in SPM was evaluated and compared. The performance of both registration algorithms was evaluated for the human and mice datasets in terms of success rate, capture range, sensitivity to reduced FOV and accuracy.

3.3.2.a. Success rate

Success rate reflects the effectiveness in achieving 'satisfactory' results for a set of initial misalignments. Successful registrations were considered those producing registration errors below the size of a voxel diagonal, i.e. $\Omega = \sqrt{v_x^2 + v_y^2 + v_z^2}$, of the image with poorest resolution, as proposed in (Ji et al. 2008). Thus, for the human dataset this threshold (Ω) was set to 4.37 mm and 8.80 mm for CT and PET registrations, respectively. Ω was of 1.35 mm for the mice PET dataset.

3.3.2.b. Capture range

Capture range is the maximum initial misalignment that produces a certain successful registration rate. Capture range has been set to 80%, as similarly proposed in (Ji et al. 2008), for all the evaluation datasets.

3.3.2.c. Accuracy

Accuracy was defined as the exactitude of the method to accomplish a successful registration. Registration error for the human dataset was externally computed in the RIRE server after submission of the estimated rigid transformation for a given image pair. This error was defined as the median target registration error (mTRE) or median Euclidean distance after registration between the centroids of a set of volume of interest (VOI) delineated both in CT/PET and MR images (West, J. M. Fitzpatrick, et al. 1997). Gold standard registration consisted of point-based registration of bone-implanted markers that were digitally removed from the images before their distribution for evaluation. For the mice dataset, gold standard registration was manually determined and following the approach described in (Knops et al. 2006), explained in the following section.

3.3.3. Performance evaluation

For success rate, capture range, and accuracy experiments offset transformations were applied to original RIRE CT and PET images to increase the initial misalignment between the images. 85 translational and rotational offset transformations were applied to each image pair resulting in 170 different starting positions for each MR image, and totalling 10,710 for the whole dataset. Translational offsets ranged from -340 to +340 mm in 4.0 mm steps, i.e. slice thickness of the MR as the image with the highest resolution, exceeding

the maximum in-plane images dimensions (332.8 mm). Rotational offsets ranged from 0 to +/- 180º in 2.12º steps.

For the mice dataset, manually PET images were resliced to the FOV and pixel resolution of the MR images. Then the methodology in (Knops et al. 2006) was implemented. Briefly, for each manually registered PET-T2 image pair, a sphere consisting of 1,000 digital coordinates was placed in the centre of the images. These digital coordinates were scattered out within the images perimeter (10 mm) and constituted the gold standard positions. Next, PET images as well as digital coordinates were misaligned using 100 random translational and rotational transformations. Translational offsets ranged from -24 to +24 mm in 0.24 mm steps and rotational offsets from -180 to 180º in 1.8º steps. For each point, the Euclidean distance between the original position (gold standard) and the position after registration was computed. The median of these distances defined the registration error. Figs. 18-19 and Figs. 20-21 show some examples of the applied translational and rotational misalignment magnitude to the human and mice image datasets, respectively.

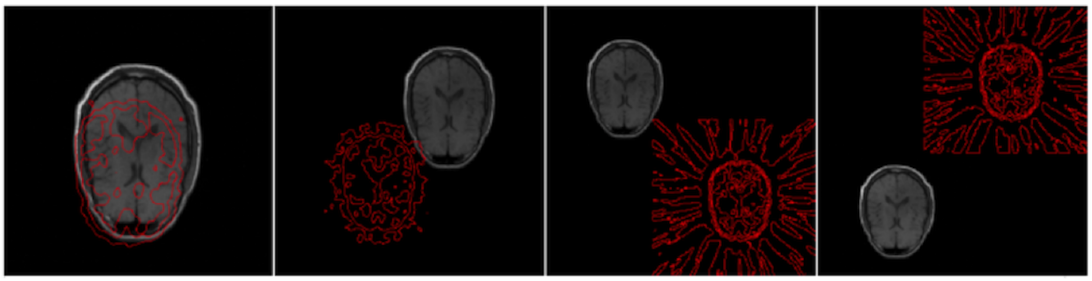

Figure 18. CT-MR in-plane translational misalignments. An axial plane view of a PET contour plot overlaid onto its T1 pair is shown. From left to right, overall misalignment (Euclidean distance of applied misalignment in each dimension) was: 37.94, 186.6, 329.2 and 359.2 mm. PET background noise is enhanced in the two most misaligned cases (on the right) to clearly define volume limits.

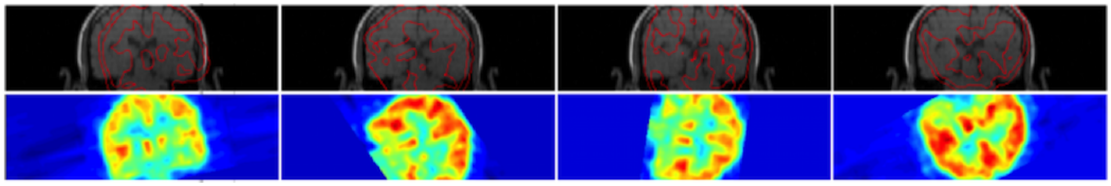

Figure 19. PET-MR in-plane rotational misalignments. On the top row, the contour of a PET coronal plane view overlaid onto its T1 pair is shown for each misalignment. On the bottom row, the PET image is displayed to ease interpretation. From left to right, overall misalignment (Euclidean distance of applied misalignment in each dimension) was: 13.3º, 57.56º, 88.98º and 162.2º.

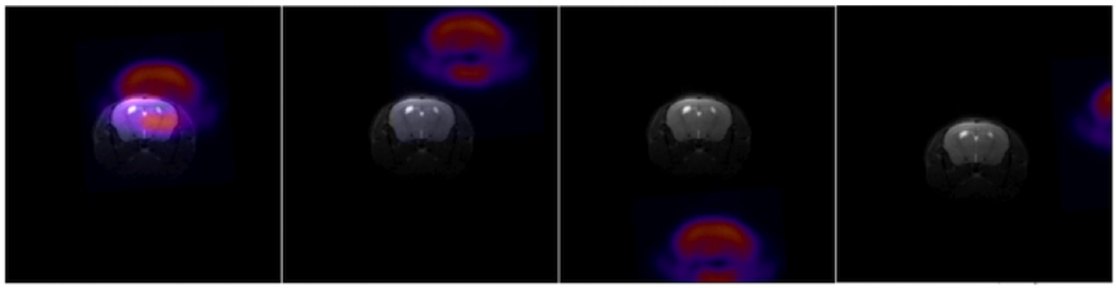

Figure 20. In-plane translational misalignments of a PET/T2 mice brain image pair. Axial planes are shown. From left to right, overall misalignment (Euclidean distance of applied misalignment in each dimension) was: 6.06 mm, 12.12 mm, 18.42 mm and 23.76 mm.

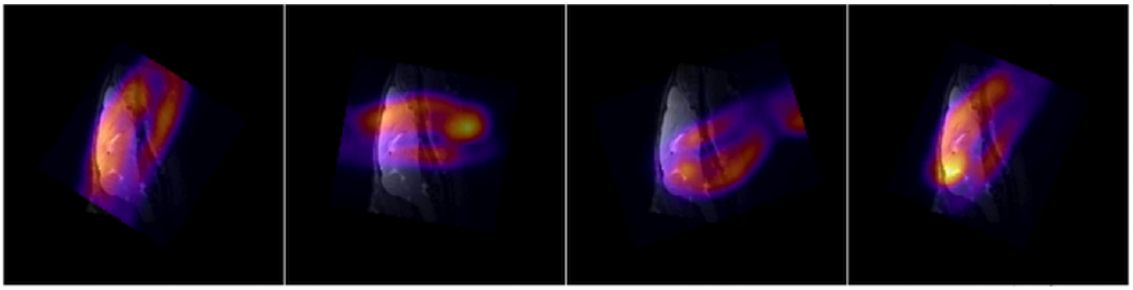

Figure 21. In-plane rotational misalignments of a PET-T2 mice brain image pair. Sagittal planes are shown. From left to right, overall misalignment (Euclidean distance of applied misalignment in each dimension) was: 47.27º, 89.09º, 152.72º and 180º.

FOV sensitivity was evaluated as described in (Studholme, D. L. G. Hill, et al. 1999). CT-MR and PET-MR image pairs of RIRE patient 5 were in-plane truncated to generate three FOV-reduced image versions (FOV1-original, FOV2 and FOV3). To each set of images three sets of 50 random rigid transformations (combining translational and rotational offsets) ranging from -10 to 10 mm and -10 to 10º (TF1), from -20 to 20 mm and -20 to 20º (TF2), and from -30 to 30 mm and -30 to 30º were applied.

3.4. Results

3.4.1. Success rate

3.4.1.a. Human dataset

For some CT-MR images and even at small perturbations, NMI and SMI registration errors systematically fell between Ω and 2Ω. Because the focus was to assess the capability of the methods to align images at varying degrees of overlap, the CT-MR registration success criterion was relaxed to 2Ω (8.74 mm). Success rate as a function of initial misalignment is shown in Fig. 22. SMI and NMI performed almost identically for CT-MR misalignments below 50 mm and 15º. For PET-MR registrations, SMI showed slight improvement (around 5 %) over NMI for translational and rotational misalignments below 50 mm and 5º, respectively. It was beyond these ranges that SMI showed remarkable higher success rates than NMI. CT-MR NMI and SMI

registrations produced overall success rate of 36.65 % and 46.46 % (increase of 9.81 %), respectively, for translational misalignments. NMI and SMI produced success rates of 53.67 % and 69.16 % (increase of 15.49 %), respectively, for rational misalignments. Greater improvements were observed for PET-MR registrations: 38.82 % with NMI and 78.53 % with SMI (increase of 39.71 %), for translational misalignments, and 16.32 % with NMI and 67.35 % with SMI (increase of 51.03 %), for rotational misalignments. It could also be observed that SMI reached a plateau at smaller misalignments than NMI, showing a higher insensitivity to increasing misalignments.

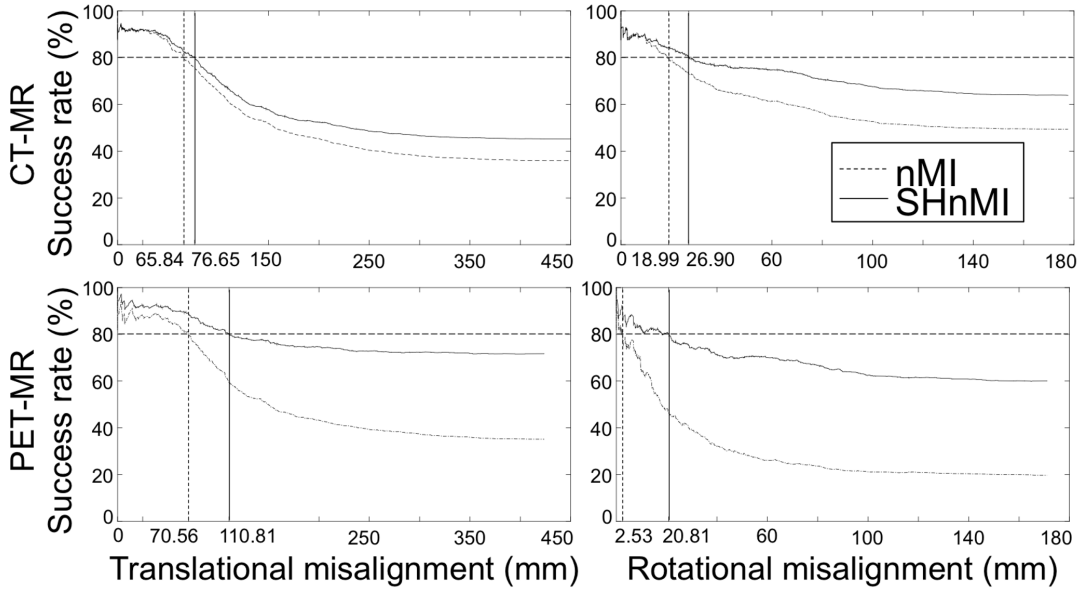

Figure 22. Success rate and capture range results for the RIRE dataset. Overall success rate is given in relation to initial misalignment. Translational and rotational misalignments are given as the Euclidean distance of the translations or rotations applied to each axis, i.e. $\sqrt{t_x^2 + t_y^2 + t_z^2}$ and $\sqrt{\theta_x^2 + \theta_y^2 + \theta_z^2}$, respectively. Top left: CT-MR translational; bottom left: PET-MR translational; top right: CT-MR rotational; bottom right: PET-MR rotational. Vertical dashed and solid lines indicate capture range values for NMI and SMI, respectively, determined by the intersection with the horizontal dashed line placed at 80% success rate.

Table 1 and 2 show NMI and SMI success rates for translational and rotational CT/PET-MR registrations, respectively. It was remarkable the fact that SMI maintained a consistent success rate close to 70 % for all CT-MR registrations and for rotational misalignments. Conversely, prominent success rate drops to about 35 % were observed with NMI for MR rectified images. This effect was still more pronounced in NMI PET-MR registrations for rotational misalignments, especially for T1-, T2- and PD-PET registrations.

Table 1. Success rate (%) for translational misalignments, mean (SD)

Floating image	Method	Reference image					
		T1	T2	PD	T1r	T2r	PDr
CT	nMI	34.1 (2.56)	21.3 (3.89)	34.1 (4.30)	44.3 (1.77)	42.7 (2.86)	43.3 (3.60)
	SHnMI	43.0 (2.95)	26.9 (4.94)	41.2 (4.61)	55.7 (11.7)	53.9 (11.7)	58.0 (13.5)
PET	nMI	32.9*	40.0*	38.8*	40.6 (1.52)	42.1 (4.34)	38.5 (2.01)
	SHnMI	72.9*	81.2*	80.0*	80.3 (5.29)	80.0 (6.00)	76.8 (3.09)

*Among all patients tested, only one had PET-MR images with no rectified MR versions. Therefore, N=1 for this case.

Table 2. Success rate (%) for rotational misalignments, mean (SD)

Floating image	Method	Reference image					
		T1	T2	PD	T1r	T2r	PDr
CT	nMI	72.4 (2.64)	75.1 (3.75)	70.6 (2.35)	32.5 (16.3)	34.3 (14.0)	37.1 (14.9)
	SHnMI	70.2 (3.67)	70.25 (4.74)	70.6 (1.66)	65.5 (9.43)	70.6 (10.8)	67.8 (8.11)
PET	nMI	2.35*	7.06*	9.41*	25.0 (25.3)	28.5 (27.4)	25.6 (26.5)
	SHnMI	61.2*	72.9*	69.4*	65.9 (9.46)	64.7 (6.93)	70.0 (6.11)

*Among all patients tested, only one had PET-MR images with no rectified MR versions. Therefore, N=1 for this case.

3.4.1.b. Mice dataset

As in the RIRE dataset, some images consistently produced NMI and SMI registration errors falling between Ω and 2Ω. Consequently, the success criterion was also set to 2Ω to provide a more explanatory interpretation of the results. Success rate results for the mice dataset are shown in Fig. 23. Overall SMI success rate was 89.92 %, outperforming NMI's 38.36 % (increase of 51.45 %). For rotational misalignments, NMI produced an overall success rate of 59.27 %, a 3.36 % increase with respect to SMI (55.91 %).

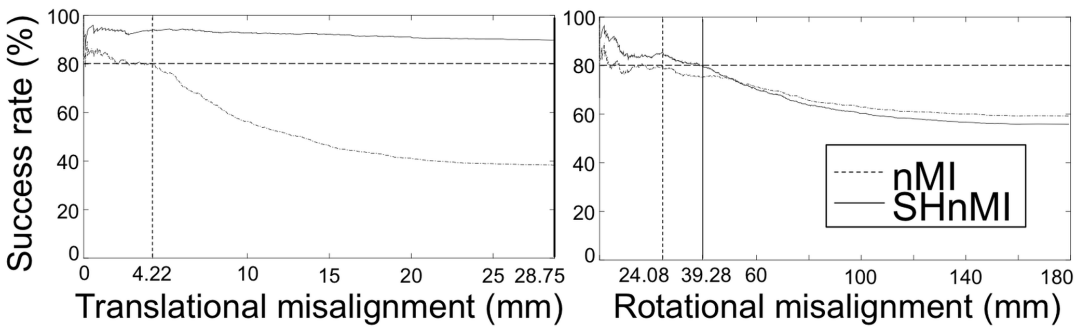

Figure 23. Success rate for PET-T2 mice dataset. Overall results are presented for translations (left) and rotations (right). Vertical dashed and solid lines indicate capture range values for NMI and SMI, respectively, determined by the intersection with the horizontal dashed line placed at 80% success rate.

3.4.2. Capture range

3.4.2.a. Human dataset

Fig. 18 also shows capture range values as determined by the intersection between an 80 % success rate and the degree of misalignment as marked by vertical dashed and solid lines, for NMI and SMI, respectively. SMI was more robust to reduced overlap and showed remarkable superiority for PET-MR images. NMI and SMI capture ranges for CT-MR images were of 65.84 mm and 76.65 mm (increase of 10.81 mm), respectively, for translational misalignments; and of 18.99º and 26.90º (increase of 7.91º), for rotational misalignments. NMI and SMI capture ranges for PET-MR images were of 70.56 mm and 110.81 mm (increase of 40.25 mm), respectively, for translational misalignments; and 2.53º and 20.81º (increase of 18.28º), for rotational misalignments.

The capture range of a registration method is highly dependent on the smoothness of its cost function for a given pair of images. Fig. 24 shows NMI and SMI cost functions for RIRE patient 1 CT-T1 and PET-T1 images. In-plane translations were applied in 1 mm steps till no overlap was given. NMI cost function revealed prominent local optima for large misalignments, whereas SMI showed a smoothed convergence to global optima for the entire misalignment range that would explain its superior performance in terms of capture range.

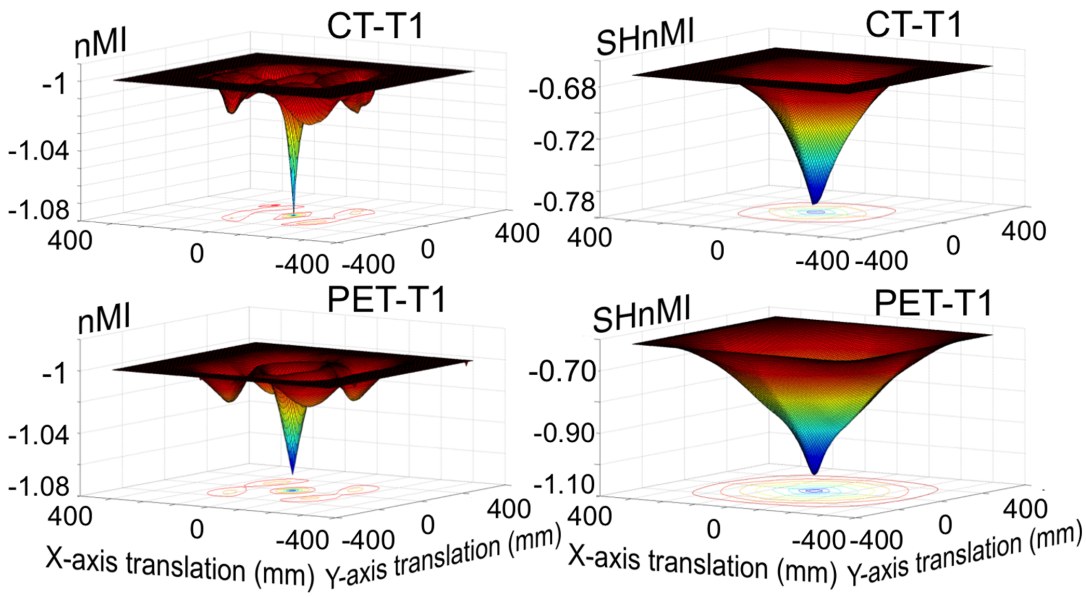

Figure 24. Cost Function based on either NMI (left) or SMI (right) for patient 1's CT-T1 and PET-T1 images. Negative cost function values are presented for a better visualization. A smoother convergence is observed for SMI while several local maxima are found with NMI. Translations range goes from -340 to 340 mm in a 1 mm step.

3.4.2.b. Mice dataset

Fig. 23 also shows capture range results for the mice dataset. For initial translational misalignments, NMI and SMI capture ranges of 4.22 mm and 28.75 mm (increase of 24.53 mm) were obtained, respectively. These results were particularly noticeable given that the capture range observed for SMI responded to the maximum translational misalignment applied to the entire dataset. These results imply that as long as there was minimal overlap between mice brain PET-T2 images, SMI was capable of aligning them together. As for rotational misalignments, SMI (39.28º) surpassed by 15.20º the capture range of NMI (24.08º).

3.4.3. FOV sensitivity

3.4.3.a. Human dataset

Table 3 shows results of registration sensitivity to varying FOV for RIRE patient 5 images. Success rate is presented for each FOV and transformation range. SMI was insensitive to varying FOV for all tested misalignment ranges. Poor NMI success rates were observed only for the most severely truncated (TF3) CT-MR registrations. Also for the most truncated CT-MR images, degree of misalignment correlated with a decreasing success rate. For TF1 and TF2 CT-MR registrations and all PET-MR registrations, NMI produced almost always 100 % success rate.

Table 3. Success rate (%) for varying fov, mean (SD)

Pair modality	Method	10 mm 10º			20 mm 20º			30 mm 30º		
		TF1	TF2	TF3	TF1	TF2	TF3	TF1	TF2	TF3
MR-CT	nMI	100	100	50.7	99.3	98.7	40.7	94.7	88.0	25.3
	SHnMI	100	100	100	99.3	100	98	95.3	100	98.7
MR-PET	nMI	100	100	100	100	100	98.7	100	100	92.0
	SHnMI	100	100	100	100	98.7	100	100	100	99.3

FOV results (for patient 5) are provided by the success rate in relation to the range of misalignment and in-plane FOV reduction of the images (TF1: original, TF2: about 30% reduction; TF3: about 60% reduction).

3.4.4. Accuracy

3.4.4.a. Human dataset

No significant differences between NMI and SMI registrations were observed for translational and rotational misalignments (0.42 mm absolute average difference). Table 4 shows averaged accuracy results for each method and image modality pair and including both registrations of translational and rotational misaligned images. Best results for each method are highlighted in bold. SMI produced more accurate CT-MR

registrations than NMI, performing best in CT-PDr pairs. However, NMI achieved more accurate PET-MR registrations than SMI, especially for PET-PDr images.

Table 4. Accuracy results given as the mean TRE (mm) for the totality of translational and rotational misalignments, mean (SD).

Floating image	Method	Reference image					
		T1	T2	PD	T1r	T2r	PDr
CT	nMI	**3.52 (0.65)**	3.84 (0.40)	4.06 (0.58)	3.81 (1.47)	3.97 (1.55)	3.74 (1.64)
	SHnMI	2.75 (1.53)	2.35 (0.40)	3.38 (1.05)	2.40 (1.58)	3.29 (1.74)	**2.23 (1.80)**
PET	nMI	4.66 (0.14)	2.91 (0.09)	4.37 (0.33)	2.64 (0.93)	3.70 (0.68)	**2.52 (1.17)**
	SHnMI	6.53 (0.07)	4.24 (0.27)	5.46 (0.39)	**4.03 (0.74)**	5.08 (0.24)	5.09 (0.87)

Accuracy results are provided as the mean TRE (Target Registration Error) in mm for CT- and PET-MR registrations.

3.4.4.b. Mice dataset

NMI produced more accurate registrations for translational misalignments than SMI – 0.38 mm vs 0.90 mm, respectively. NMI and SMI results for rotational misalignments were very similar – 0.59 mm vs 0.56 mm, respectively.

3.5. Discussion

In this study, a new strategy (SMI) to compute NMI was presented that improves its registration success rate, capture range and field-of-view (FOV) insensitivity while preserving its accuracy. As a major novelty, SMI includes the non-overlapping FOV of the images into the NMI calculation. The method was compared to the widely-used and well-known implementation of the standard NMI registration algorithm in the SPM8 package. Both strategies were tested on two real datasets: the open access human brain RIRE dataset, which is specific and widely accepted for evaluation of rigid-body registration methods, and a mice brain dataset available in our lab.

It was observed that, when implemented within a multiresolution optimization strategy, SMI noticeably extended the capture range of NMI, its success rate, and its insensitivity to varying FOV between images while preserving its accuracy at and average comparable computational cost (NMI: 17.36s, SMI: 29.42s). At the low-resolution level, SMI uses the combined images FOV producing accurate and stable estimates of marginal and joint entropies. Because all images information is used, marginal entropies variability is due only to interpolation. As a result, the Joint Entropy of the combined images FOV mostly drives registration at

this resolution level. As explained in section *1.5.4.e. Information measures*, the joint entropy may find global optima for maximum backgrounds overlap, which explains the outstanding results accomplished by SMI registrations (89.92 % overall success rate) of translationally misaligned mice data with greater background-to-object ratio than the RIRE dataset. While securing high degree of overlap, the global optima produced by the Joint Entropy, and by extension SMI, may not necessarily imply true alignment. To accomplish fine true alignment, including solely the overlapping FOV in the high-resolution optimization step is best and, therefore, the NMI should be used. By doing so, the image areas that drive fine alignment are the regions of interest with registration not being influenced by the non-overlapping information, commonly of little relevance in medical images. Only when SMI produces global optima in the low-resolution level that fall within the global optima basin of NMI in the low-resolution level, are true alignments achieved. This explains why translational capture ranges of the proposed method are not larger, and the similar success rates and accuracy results between the methods for both datasets at small misalignments (Fig. 22-23). Unsuccessful registrations occurred when despite of securing large volume of overlap between the images, SMI produced results where images were flipped with respect to each other. This effect was particularly noticed for largely rotated images and especially for the mice dataset with larger background regions driving alignment at the low-resolution level. At the high-resolution optimization step, the algorithm would be trapped in a local minimum explaining the equivalent results obtained between methods for rotational misalignments of mice images (Fig. 23).

SMI also outperformed NMI insensitivity to FOV. In this paper we replicated the experiment described in (Studholme, D. L. G. Hill, et al. 1999) to evaluate FOV insensitivity of the methods. The authors established an interactive threshold to select the overlapping voxels between the images and the mean voxel displacement with respect to the ground truth alignment would be used to determine registration success. As we lacked of information to implement the same evaluation method, the registration error retrieved from the RIRE server to calculate success was used. Although PET-MR results agree with those obtained in (Studholme, D. L. G. Hill, et al. 1999), CT-MR NMI registrations perform worse with reduced FOV and increased misalignment. As the FOV is reduced, so is the overlapping region between the images. Consequently, entropies calculations include fewer and fewer voxels leading to highly changing and unstable entropies. Because SMI includes non-overlapping occurrences in the entropies calculation, this effect is to some extent counterbalanced.

Accuracy depends not only on the cost function but also on the optimization algorithm and the image interpolation used after mapping the floating image (CT or PET) into the space of the reference image (MR). This explains that, although NMI and SMI are equivalent in the high resolution step of the optimization algorithm, slightly different results were observed. Overall, NMI showed better accuracy for CT-T1 and PET-

PDr pairs while SMI was more accurate for CT-PDr and PET-T1r pairs. For the mice dataset SMI outperformed NMI only for translational misalignments while producing almost identical results for rotational perturbations. Nonetheless, for all modalities average registration errors of successful registrations, i.e. mTRE < 2Ω, produced average subvoxel (Ω) errors. Thus, in spite of the observed differences in accuracy, these are of no practical consequences.

In spite of the superior capture range of SMI, our method is not expected to converge for completely non-overlapping volumes. To address this problem, other approaches have been devised and can be found elsewhere (Reuter et al. 2010; Ji et al. 2008). Some of our results compare well with those obtained in literature. Accuracy values for PET-T2 images of the RIRE dataset with NMI in (Skerl et al. 2006) are close to the ones presented here (3.1 mm vs. 2.9 mm, respectively). FOV insensitivity results for PET-MR registrations also agree with those obtained in (Studholme, D. L. G. Hill, et al. 1999). Other authors have shown that other information measures provide more accurate results for the RIRE dataset (Pluim et al. 2004) or that local image information allows finer registration of structures of interest (Greve & Fischl 2009) at the expense of a reduced capture range and increased computation cost. Future work inlcudes implementing SMI in other information-based measures, such as MI, and to evaluate its efficiency with medical datasets of other organs and modalities. To facilitate comparability between methods, the code is currently available through email to anyone who should request it, as a more accessible platform is explored for easier access. It is strongly encouraged to use publicly available datasets like RIRE that allow for objective assessment of registration accuracy and comparability of the results.

3.6. Conclusions

A new multi-modal registration strategy (SMI) based on the standard normalized mutual information (NMI) was presented. SMI fully exploits the non-overlapping FOV of the images. The methods were evaluated with human (RIRE dataset) and mice (own data) images of the brain. We observed an overall improvement of SMI performance with respect to NMI in terms of success rate, capture range and FOV sensitivity for both datasets. Accuracy is comparable to that of the standard method.

4. Simultaneous registration and IIH correction of small brain MRI and PET

4.1. Introduction

The causes that originate the IIH artefact are two-fold. On one hand, those attached to the MR scanner including static and RF field inhomogeneities or eddy currents, induced by gradient fields switching(Vovk et al. 2007). And second, those introduced by the loading effect of the subject (Sled & Pike 1998), whose impact is larger the higher the magnitude of the magnetic fields. Accordingly, correction methods addressing IIH can be classified in two distinct grops. Prospective methods focus on solving solely machine-induced inhomogeneities. These methods may make use of the known geometry of phantoms, imaged with multiple coils, or use special excitation sequences to estimate the intensity shadowing associated to coils imperfections (Sosnovik et al. 2007; Lewis & Fox 2004; Wang et al. 2005). Retrospective methods, on the other hand, deal with little or none a priori information, make no distinction between artefact sources and, therefore, can be more generally applied (Van de Moortele et al. 2009; Salvado & Wilson 2007).

Much work has been done in the retrospective field so far and comprehensive reviews can be found in (Belaroussi et al. 2006; Hou 2006; Vovk et al. 2007). Low pass filtering was suggested first to remove the high-frequency content attached to IIH (Axel et al. 1987; Lim & Pfefferbaum 1989). However, these methods provided only partial correction of IIH, with its spectral signature commonly overlapping that of the imaged object. More sophisticated approaches involving tissue segmentation aimed at providing more comprehensive solutions, but the ultimate performance of these methods is heavily dependent on segmentation results. Increased complexity, time consumption, and an atlas is required by joint segmentation-correction-non-rigid registration methods (Ashburner & Friston 2005; Young Kim & Johnson 2013; Daga et al. 2014). Frequently, these methods implement a Finite Gaussian Mixture (FGM) model of main brain tissues and non-tissue areas (Guillemaud & Brady 1997; Young Kim & Johnson 2013), represented as multi-modal normal intensity probability distributions. The maximum likelihood (ML) and the maximum a posteriori criteria are then used to find the optimal FGM parameters to produce segmented brain tissues and IIH-free images (Bansal et al. 2004; Gispert et al. 2003; Gispert et al. 2004). Probabilistic approaches are commonly framed in an expectation-maximization (EM) algorithm that iteratively interleaves correction and segmentation. Alternatively, surface-fitting methods have also been proposed for joint tissue segmentation and correction but often need selection of representative points (Dawant et al. 1993). Fully automatic intensity-based solutions were proposed later by (Likar et al. 2001; Mangin 2000) relying on minimization of the image entropy to reduce intensity inhomogeneity in human brain MR datasets. An entropy-minimization approach was further developed to include spatial information (Vovk et al. 2004), who built a 2D image intensity-gradient histogram that included the image second derivatives. This spatial information was also used to

obtain a smooth estimation of the bias correction field. The algorithm aimed at minimizing the combined entropy measure. Similarly, (Manjón et al. 2007) estimated image entropy as the Kronecker delta product of the original and gradient image to find the best coefficients of a B-spline polynomial basis. The order of the polynomials was iteratively increased until no change in the image entropy was observed, as suggested in (Likar et al. 2001). Finally, a mathematical appreciation was pinpointed in (Ashburner & Friston 2005; Thacker et al. 2002). Because the inhomogeneity artefact is commonly modelled as a multiplicative polynomial, the log of this scaling factor biases the estimation of the corrected image entropy. Hence, in the intensity space the corrected image entropy estimation does not strictly correspond to the sum of the image and field entropies. Instead, the authors proposed to minimize the entropy of the log-transformed image intensities and model the correction field as an additive effect in the log-space. As a result, image and field entropies can be independently calculated. Since then, correction in the log-space has been an unanimously adopted measure in later implementations and new developments of information-based methods.

While these methods yield satisfactory results for human brain MRI, their application to small-animal brain MRI is not straightforward (Rangarajan et al. 2011; Lin et al. 2013). Notwithstanding the increasing field strenghts of modern MRI scanners, small-animal MRI systems operate at still higher field magnitudes to produce high resolution images of, for instance, the mice brain, about 10 mm long. Because of the increased frequency of spinning nuclei under larger field magnitudes, the effect of RF standing waves and penetration and ultimately, the magnitude of the intensity inhomogeneity, is larger in small-animal MRI systems. Also critical is the fact that the structural content of the mice brain is significantly lower than that of humans. As an example, the folding pattern of the human brain cortex, i.e. the sulci and gyri, is barely present in the mice brain. Inevitably, IIH disrupts more detrimentally small-brain MRIs and challenges accurate registration and segmentation.

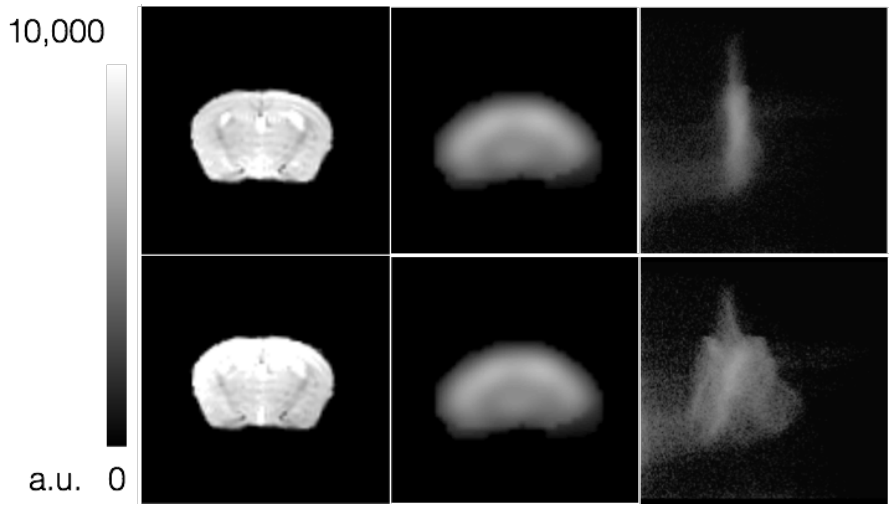

Figure 25. Effect of MR intensity inhomogeneity in the joint histogram. On the top row, the joint histogram of a manually registered PET-MR pair shows a compact cluster formed by a large number of intensity co-occurrences. On the bottom row, a less compact cluster is observed in the joint histogram when the MRI is affected with even low magnitude IIH.

Understanding that automated segmentation can be accomplished through registration to a template, a reasonable ultimate aim of IIH correction should be to secure robust and accurate registration (Knops et al. 2006). To this purpose, (Rangarajan et al. 2011) demonstrated the impact of IIH in registration accuracy in a study with mice brain MRI of the mice brain. The authors used the entropy-minimization method (Likar et al. 2001) for correction and maximization of mutual information (Maes et al. 2003) for registration. However, because information-based correction methods address IIH correction and registration independently, the level of correction quality accomplished remains undetermined and does not necessarily secure successful registration. To overcome such limitation, it is proposed here to exploit the shared information between the images to iteratively correct and register IIH MR images of the mice brain until no further correction is possible at a given and hopefully accurate registration. To this purpose, the iterative IIH correction-registration strategy (IRIS) unites the correction and registration cost function to ultimately accomplish more accurate registrations and finer IIH corrections.

The 18F-FDG PET – MR dataset presented in section *3.3.1.b. Mice* used to evaluate the performance of the novel registration method (SMI) was also used here, given that the MR data was severely affected by IIH. The widely-used correction method proposed in (Likar et al. 2001) was applied to IIH-corrupted images either to minimize MR images entropy or to maximize MR-PET NMI or SMI, as the correction-registration optimization cost function. Then, iterative correction-registration was compared to separate correction and registration by means of NMI or SMI maximization (section *3. Registration of multi-modal neuroimaging datasets by considering the non-overlapping field of view into the NMI calculation*).

4.2. Materials and Methods

4.2.1 Rationale

NMI maximization is accomplished through maximization of the intensity co-occurrences between images. As extensively developed in earlier sections, such maximization is an indicator of the degree of spatial alignment between images, which is highest the lower their joint Entropy *H(A,B)*. In addition, *H(A,B)* is also minimized the lower IIH dispersion of the MRI pair for a given spatial alignment (Fig. 25). Then, it is reasonable to conclude that more accurate IIH corrections result in more accurate registrations and viceversa. In this Thesis an iterative two-step strategy is presented and its performance evaluated as a function of NMI or SMI as the unified optimization parameter for IIH correction and multimodal registration. The correction phase prepares the biased image to push the registration algorithm to a closer-to-maxima NMI/SMI solution and the procedure is iterated until the NMI/SMI is no longer maximized. The strategy has been baptized IRIS, as the acronym of Iterative Registration IIH correction Strategy.

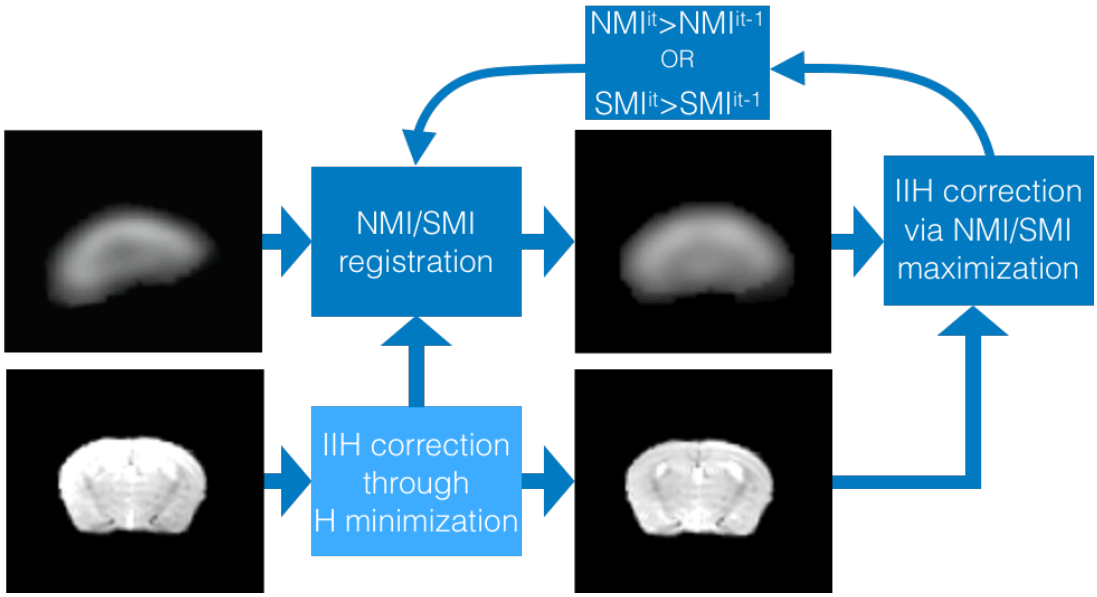

Figure 26. Iterative Registration IIH correction Strategy (IRIS) scheme.

4.2.2 Correction Method

The widely-used retrospective information-based method proposed in (Likar et al. 2001) was implemented for IIH correction. This method is based on the assumption that since the induced intensity inhomogeneity is spatially different from the natural intensity variations in the true image, the information content of the degraded image is higher than the information of the true image.

The amount of image information can be measured from the image histogram as the Shanon entropy (eq. 11). As a result, an information increase due to IIH also implies an increase of the image Entropy. IIH disuption is observed in the image histogram as a broadening and shifting of the tissue modes, and an overall flattening of the histogram. In the image, the artifact disperses the intensity values and shifts the overall mean intensity. To remove the artifact, the method aims at minimizing the image entropy to recover true tissue contrasts while maintaining the global image mean, which lacks of biological importance in structural MRIs. Importantly, the correction approach proposed by Likar et al. does not corrupt bias-free images (Likar et al. 2001). The method describes the intensity degradation with a linear model, consisting of a multiplicative or additive component that can be expressed as a combination of smoothing varying linear polynomials. According to the authors, a better correction is obtained in T2-weighted images when only the multiplicative factor is considered and the order of the polynomials is set to four. As suggested in (Thacker et al. 2002; Ashburner & Friston 2005), the log-transformed images was used to properly estimate the entropy reduction accomplished by the multiplicative correction field after each iteration. In this work, a heuristic approach described in section *4.2.4 Implementation* was followed to apply specific parameter tuning of the method to achieve effective reduction of the high magnitude artefact observed in our small-animal brain MRI dataset.

4.2.3 Optimization Parameter

Two unified optimization parameters for correction and registration stages are compared, the NMI (eq. 13) and the SMI (eq 17). For clarity, the iterative process is described for NMI but is the same for SMI. In the registration stage, the NMI of the images is maximized mostly by means of H(A,B) minimization, in the denominator. The interpolation effects of the moving PET image (A) during registration affecting H(A,B) and H(A) are counteracted by placing H(A) in the numerator. The MRI is used as the image reference and remains unchanged as so does its entropy H(B). In the correction stage, the aim is also to maximize NMI yet through minimization of H(A). Clearly, H(A,B) is minimized with H(A) minimization, however, NMI will only increase when the joint entropy reduction is relatively higher than the MR image entropy reduction. With the PET image being unchanged, correction is virtually accomplished through maximization of the ratio between the *H(B)* and *H(A,B)*, conditioned to *H(B)* minimization. To prevent the optimization algorithm to find a solution that maximized NMI by increasing the *H(B)* relatively more than the joint entropy *H(A,B)* the following condition was imposed:

$$NMI^{it} = \frac{H(A)+H(B)^{it}}{H(A,B)^{it}} \quad only\ if \quad H(B)^{it-1} > H(B)^{it} \tag{18}$$

Being $H(B)^{it-1}$ the marginal entropy of the MR image and *it* the iteration number. Intuitively, $H(B)^{0}$ corresponds to the entropy-corrected image with Likar's method. Essentially, NMI (or SMI) correction aims

at finding the minimum MR image entropy that minimizes the joint entropy of the images to be registered or, equivalently, to increase their joint intensity co-occurrences.

4.2.4 Implementation

Correction and registration methods were implemented in Matlab 8p4 (The Mathworks, Natick, MA, USA). Likar's entropy minimization method was implemented as described in (Likar et al. 2001). SPM8 Matlab package (Ashburner 2012) functions were used for registration and estimation of joint and image entropies, calculated from the images joint hitogram for IRIS correction. The implementation of the 2D joint histogram in SPM8 slightly differs from the 1D histogram described in (Likar et al. 2001). In particular, the authors used a triangular window to smooth the image histogram compared to the decaying exponential window implemented in SPM. The width of such windows is estimated in SPM from the reference image resolution, i.e. the MRI, but it was fixed to 5 as detailed in (Likar et al. 2001). Finally, the image sampling rate to compute the joint histogram was adjusted to the submillimiter voxel dimensions of the mouse brain MRI. Because SPM registration is implementd within a two-level multiresolution framework (see section *1.3. Optimization*), the sampling step was set to 4 and 2 voxels for each dimension in the lowest and highest resolution levels, respectively. Similar parameters adjustments were applied to the SPM registration implemenation in a study using a mouse brain 18F-FDG dataset in (Pascau et al. 2008).

Briefly, SMI is implemented in a two-level resolution. At the low-resolution level and differing from conventional NMI, the full images FOV is used in the calculation of the NMI. At this stage, the non-overlapping information provides valuable information of the degree of misalignment between the images, which can be used to secure coarse alignment between them. At the high-resolution level, the joint entropy is calculated from the voxels inlcuded only in the overlapping FOV, as NMI does. Image entropies are calculated from the full FOV for both the low and the high-resolution level, producing stable estimates throughout the optimization process. Relying exclusively on overlapping voxels increases the sensitivity of the joint entropy to finer alignment of structures of interest located within the FOV. Because NMI uses solely overlapping voxels, its highly accurate results are conditioned to significant overlap between the images.

4.2.5 Methods comparison

IIH correction by means of H minimization (Likar et al. 2001), and iterative NMI and SMI maximization through IRIS was compared. IRIS registration results were compared to NMI (Studholme, D. L. G. Hill, et al. 1999) and SMI registration methods with and without IIH correction. The following coding will be used to refer to the evaluated correction-registration combinations: O-NMI (original MRI registered with NMI), O-SMI (original MRI registered with SMI), H-NMI (H-corrected MRI registered with NMI), H-SMI (H-

corrected MRI registered with SMI), IRIS-NMI (iterative correction-registration with NMI as the joint optimization parameter), and IRIS-SMI (iterative correction-registration with SMI as the joint optimization parameter).

4.2.6 Validation studies

4.2.6.a. Simulated data

The open access three-dimensional atlas C57BL/6J of the mouse brain developed in the Brookhaven National Laboratory (Ma et al. 2008) was used. The atlas was constructed from T2-weighted 3D magnetic resonance microscopy (MRM) images acquired on a 17.6 T scanner and it is intended to integrate structural data variability not present in traditional histology-based atlases. The atlas was of 192 x 96 x 256 with an isotropic voxel resolution of 0.10 mm and 16-bit quantization, but it was resized to 128 x 128 x 128 and isotropic voxel dimensions of 0.17 mm to match the field of view of our real MRI dataset. The atlas comes with a total of 20 brain structures segmentations, which were grouped in gray matter (GM), white matter (WM) and cerebro-spinal fluid (CSF). From this three major tissues, the method proposed in (Desco et al. 2005) was used to simulate a 18F-FDG PET image (Fig. 27). Poisson noise was introduced into the image prior to smoothing with a gaussian kernel of 2.5 mm full width-half maximum to produce an image qualitatively as similar as possile to our real data. Finally, simulated PET images were resampled to a matrix size of 256 x 256 x 63 with an in-plane resolution of 0.42 mm and axial resolution of 1.2115 mm, to match that of the original PET dataset.

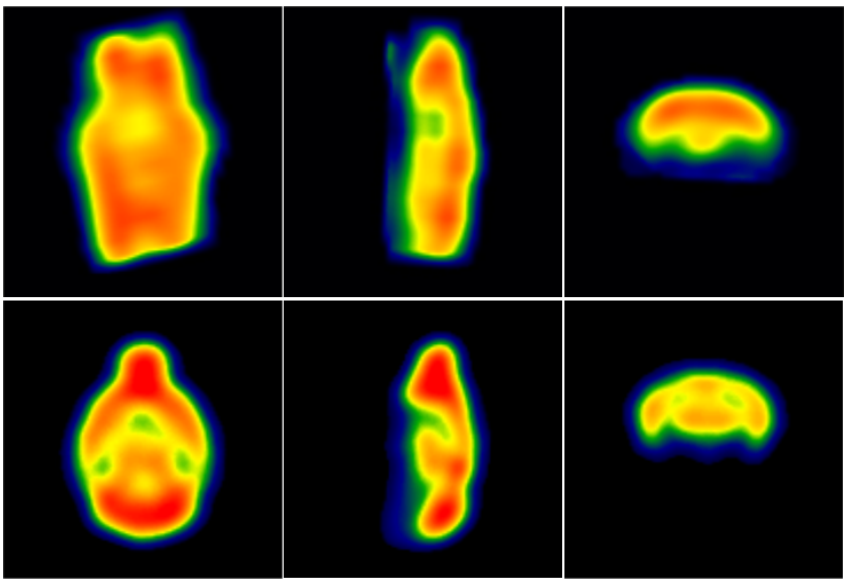

Figure 27. Real (top) and simulated (bottom) 18F-FDG PET image of the mouse brain. Coronal, saggital, and axial 2D planes are shown from left to right, respectively. Notice that Harderian glands could not be simulated from magnetic resonance images.

4.2.6.b. Real data

A total of 11 wild-type (WT) mice underwent MRI scanning in a 7-Tesla Bruker BioSpin device with a surface coil using a spoiled gradient-echo sequence (Echo Time = 8 ms; Repetition Time = 1500 ms) which provided T2-weighted images with a matrix size of 128 x 128 x 128 voxels of 0.17 x 0.17 x 0.17 mm in size. Images suffered from IIH during the acquisition process.

The same mice were scanned during 10 minutes in a microPET R4 scanner of Concorde Microsystems after being injected with 285 μCi 18F-FDG and 45 minutes of tracer's uptake. The FOV was of 1.8 cm and its spatial resolution of about 1.9 mm Full Width at Half Maximum (Popota et al. 2009). An OSEM 3D reconstruction (12 subsets, 2 iterations) was applied to the acquired data. Reconstructed images had a matrix size of 256 x 256 x 63, 8-bit quantization, 1.2115-mm slice thickness and 0.42 x 0.42-mm in-plane resolution.

4.2.7. Image pre-processing

4.2.7.a. Simulated data

Extra-cranial brain tissue was masked in the MRI atlas by means of a whole brain mask included in the database. This image also presented an IIH artifact, which was reduced after applying the Likar's method (Likar et al. 2001) and taking, in this case, all brain image voxels in the entropy calculation to achieve maximal correction. Because the simulated PET image was perfectly aligned to the atlas, a slightly larger version of the MRI whole-brain mask was used to remove background noise while preserving the smoothed brain contours in the PET image. Next, simulated PET images were resliced to match the pixel size of the MR image data.

4.2.7.b. Real data

Mice brain were manually masked in real MRI and PET images. In PET images, whole-brain masks also included Harderian glands intensities, whose hyperintensity spills out in the frontal cortex challenging accurate brain segmentation. MRI brain masking is actually advised to avoid background noise having any influence on the estimated correction field (Likar et al. 2001). Next, 18F-FDG PET images were manually registered and resliced to the FOV and pixel size of their MR image pair. This manual alignment constituted our gold-standard registration.

4.2.8. Evaluation

4.2.8.a. IIH Correction

Correction and registration were visually and quantitatively assessed. MRI artifact suppression was visually inspected and the joint histogram displayed after correction at the last iteration to assess the improved compactness of histogram clusters. Quantitative evaluation was accomplished as in (Likar et al. 2001; Belaroussi et al. 2006; Gispert et al. 2004; Manjón et al. 2007; Vovk et al. 2007) by means of computing the coefficient of variation CV of brain tissue (T) :

$$CV(T) = \frac{STD(T)}{MEAN(T)} \tag{18}$$

A set of three simulated inhomogeneity fields were generated from a combination of cosine basis functions to produce image inhomogeneities of magnitude 10%, 20% and 30% (Fig. 28). *CV* in the range 10%-20% magnitudes are common in IIH-artifacted human brain MRI (Mangin 2000; Dawant et al. 1993; Sled & Pike 1998). The real mice brain MRI dataset used herein was affected by intensity inhomogeneities with magnitudes close to 30%. Next, the artificial field was applied multiplicatively to the atlas image. In Fig. 28 bottom row the histograms of the logarithmic image intensities shows the broadening effect of the applied IIH field.

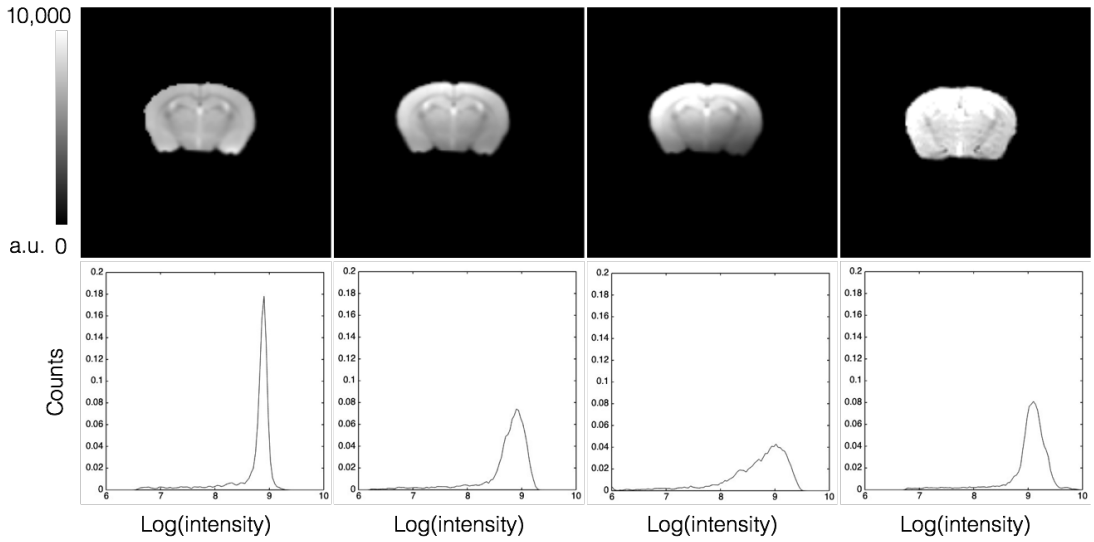

Figure 28. On the top row and from left to right, MRI mouse brain atlas with a 9.47%, 17.76% and 32.42% intensity inhomogeneity, and an original mouse brain MRI with 30.28% intensity inhomogeneity. On the bottom row, image histograms of corresponding synthetic and real MR images on the top row. The real image shows brighter intensities because its average mean is higher as shown by the position of the histogram mode in relation to simulated data.

Because no GM, WM, CSF tissue segmentation was available for the real dataset, *CV* was computed over all brain tissue in both simulated and real data. For artifact-free images lower *CV* values were expected indicating higher brain tissue homogeneity.

4.2.7.b. Registration

Registration was visually assessed to confirm successful image alignment. Quantitative validation was accomplished following the point-based method proposed in (Casteels et al. 2006). Three pairs of anatomical landmarks were digitally placed on peripheral and distinct locations of the mouse brain MR image along the three main axes of the image volume (Fig. 29, left and middle images). Since PET and MR images were manually registered the position of landmarks corresponded to the same location in both images for the entire dataset. A total of 100 known and random rigid-body transformations (T) were applied to PET images within the range +/-10 mm and +/-40 degrees in 0.1 mm and 0.4 degrees steps, respectively. The explored misalignment range here and common in pre-clinical imaging is larger than that evaluated in (Casteels et al. 2006; Rangarajan et al. 2011), 5 mm and 20 degrees, for NMI small-animal brain MR-PET registrations. In a previous study separately evaluating its translational and rotational capture range (see section *3. Registration of multi-modal neuroimaging datasets by considering the non-overlapping field of view into the NMI calculation*), SMI showed insensitivity to translational misalignments as long as there was some amount of overlap between the images, and about 40 degrees capture range for initial rotational misalignment, twice the explored misalignment found in literature. The tested misalignment range was exceeded here to guarantee that presumable differences in registration performance between SMI and IRIS would be observed. A total of 300 registrations (100 initializations x 3 field magnitudes) were applied to the synthetic dataset and 1,200 to the real dataset (100 initializations x 12 animals). Next, MRIs were corrected by means of entropy minimization and inputted into IRIS. The (fiducial) registration error (FRE) was calculated as the mean Euclidean distance of the landmark points set after registration (q') to their gold standard position (q) (see section *1.5.1.a. Registration accuracy assessment*):

$$FRE = \frac{1}{N}\sum_{i=1}^{N=6}(q_i - T\times C\times q_i')^2 \quad (19)$$

With C the inverse of the estimated spatial transform and N the number of landmarks. Registration was deemed successful if produced an FRE lower than the voxel diagonal of the less resolutive image pair (Ω), i.e. 1.35 mm for the PET image. Finally, registration accuracy was measured as the average FRE of only successful registrations.

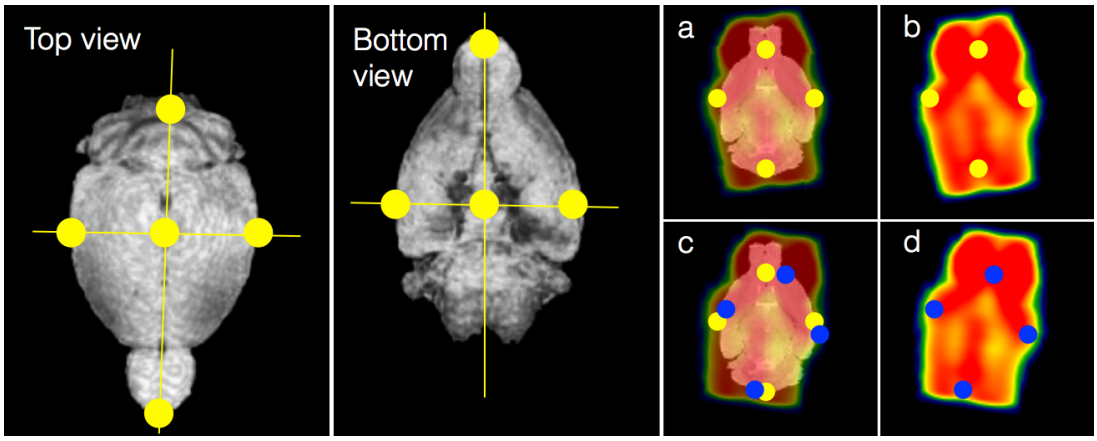

Figure 29. The set of anatomical landmarks were placed in the junction of distinct peripheral locations and the main axes of the mouse brain, shown as a 3D rendering of the masked mouse brain MRI (top and bottom view). (Right) A. Coronal view of a manually registered PET-MRI pair and landmarks. B. Coronal view of the masked brain PET of a mouse and landmarks. C. Misalignment between a PET-MRI pair and between landmarks. The distance between landmarks is used for registration error quantification (FRE). D. Visualization of landmarks on the misaligned PET image.

4.7.2.c. Quantification

The impact of registration accuracy into quantification of whole brain activity was evaluated for the real 18F-FDG PET dataset. Masks of the mice brain MRI were used to estimate the mean activity (in nCi/cc) from manually and automatically registered PET images. Mean activity values from manually registered PET images constituted the gold standard measurements. Next, the quantification error (QE) of each method (NMI, SMI, IRIS) could be calculated from the relative mean activity difference between manually-registered PET images and PET images registered to original, H-corrected, and IRIS-corrected MR images as:

$$QE_{Method} = \frac{(MEAN(PET_{Method}) - MEAN(PET_{Manual}))}{MEAN(PET_{Manual})},$$
$$Method: O-NMI,\ O-SMI, H-NMI, H-SMI, IRIS-NMI, IRIS-SMI \quad (20)$$

4.3. Results

4.3.1. Inhomogeneity correction

For the synthetic and real dataset, H-correction produced considerable artifact reduction in all MR images even at 30% IIH levels (Figs. 30-31). Visual inspection of simulated data and joint histograms at perfect alignment showed unnoticeable differences between H-corrected and IRIS-corrected images for all the field magnitudes. Iterative correction with IRIS produced either similar or improved corrections than Likar's H minimization method for both synthetic and real data. In Fig. 31 an area of the cortex (white rectangle) shows a more pronounced remaining of the IIH in the real H-corrected image than in IRIS-corrected images.

Inhomogeneity correction could also be clearly visualized when comparing the joint histogram of original and corrected MR images and their PET image pair. Highest co-occurrences, i.e. more compacted and brighter joint histograms, could be observed for H- and IRIS-corrected images (Fig. 31, arrows in the bottom row), with small differences between them.

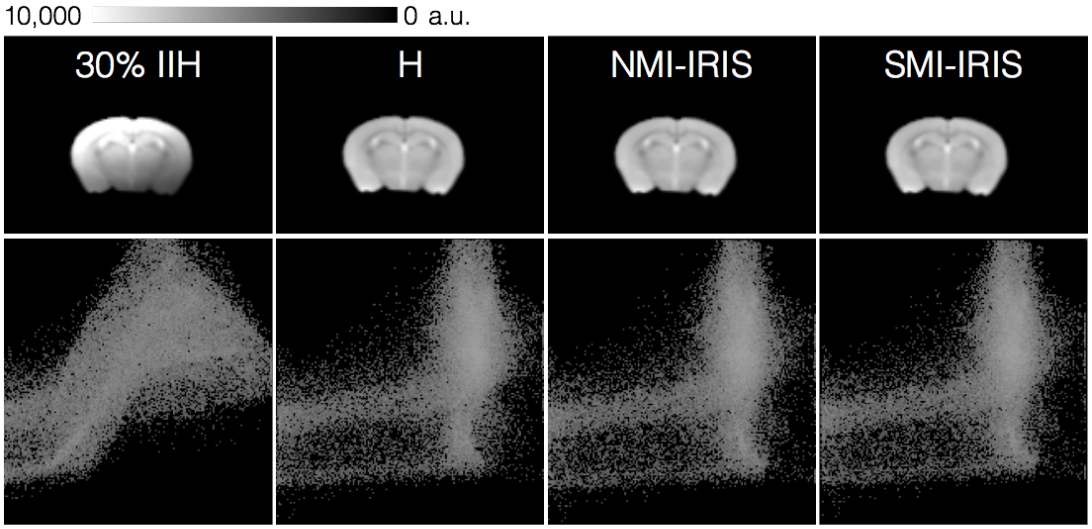

Figure 30. (Top row) Axial planes of 30% IIH and corrected images and (bottom row) correspoding joint histograms at perfect alignment with the simulated PET image.

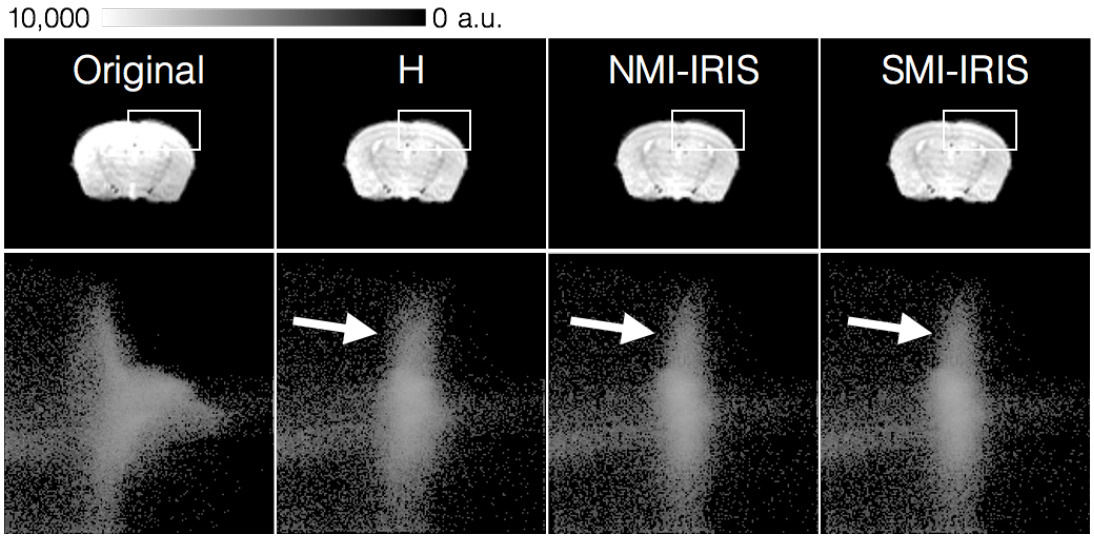

Figure 31. On the top row, axial planes of original IIH-corrupted MRI and corrected images are shown. A white box is placed on an area of the cortex where IIH remains after H minimization correction, but is less apparent after IRIS correction. The bottom row shows correspoding joint histograms at gold standard alignment with their manually registered PET image pair. White arrows show areas of higher intensity correspondences in IRIS-corrected images than in the H-corrected image.

Lower whole brain CVs resulted from both entropy and iterative corrections. Table 5 shows brain intensity CV of the MRI atlas with approximate 10%, 20% and 30% itensity inhomogeneity, and Table 6 of all the animals in the real dataset. For the iterative methods, the average of the 100 registration results obtained for each MR image is shown. H minimization practically restored Entropy and CV values for the simulated dataset with corrections exceeding 95% of original values. Similarly, H minimization coped with most of the correction for the real dataset bringing CV values from an average 30.82% down to 24.94%. Entropy and CV changes below 1% between H-corrected and iteratively corrected images were observed both in simulated and real datasets. None of the methods introduced IIH distortion in artifact-free images of the synthetic or real dataset.

Table 5. Coefficient of variation (CV) of simulated data. The average CV is shown for the iterative methods (IRIS-NMI and IRIS-SMI).

Method	CV (%)			Entropy		
	Intensity inhomogeneity (%)			Intensity inhomogeneity (%)		
	10	20	30	10	20	30
Original	9.47	17.76	32.42	4.20	4.92	5.63
H	9.47	9.96	9.80	4.20	4.27	4.26
IRIS-NMI	9.47	9.86	9.77	4.20	4.26	4.25
IRIS-SMI	9.47	9.88	9.78	4.20	4.26	4.25

Table 6. Coefficient of variation (CV) of real data. The average CV is shown for the iterative methods (IRIS-NMI and IRIS-SMI).

Method	Real data (animal #)										
	1	2	3	4	5	6	7	8	9	10	11
Original	30.28	31.08	31.99	31.05	35.29	30.33	28.26	28.95	35.74	31.17	24.85
H	28.22	23.74	25.65	26.52	24.29	23.25	23.21	25.01	24.77	26.31	23.35
IRIS-NMI	25.66	23.74	25.34	24.51	24.29	23.24	23.21	25.00	24.77	26.30	23.34
IRIS-SMI	25.66	23.74	25.35	24.52	24.29	23.24	23.21	25.00	24.59	26.31	23.34

4.3.2. Registration

Registration results with NMI worsened with increased IIH magnitude (O-NMI) for the simulated data (Table 7). After IIH correction through H minimization, registration performance was preserved when using NMI

(H-NMI) with success rates slightly increasing from 50% to 58% for corrected data. The iterative strategy using NMI as the correction-registration optimization cost function (IRIS-NMI) yielded registration improvements ranging from 26% to 62% and secured 76%-78% of successful registrations for the explored misalignment range. SMI registrations were sensitive to 30% IIH, which led to a 16% reduction of success rate, but the method was insensitive to lower IIH magnitudes with 100% of cases successfully registered. After correction by means of H minimization, SMI recovered the registration success rate of less or no artifacted images. The itereative method (IRIS-SMI) did not worsen the registration performance of H-SMI and yielded a consistent 100% success rate for all registrations and IIH magnitudes.

Table 7. Successful registration rates of simulated data without and with IIH correction through entropy minimization and IRIS.

Method	Intensity inhomogeneity (%)		
	10	**20**	**30**
O-NMI	50.00	48.00	16.00
O-SMI	100.00	100.00	84.00
H-NMI	50.00	54.00	58.00
H-SMI	98.00	98.00	98.00
IRIS-NMI	76.00	78.00	78.00
IRIS-SMI	100.00	100.00	100.00

For some real images and even at small perturbations, NMI, SMI and IRIS registration errors systematically fell between Ω and 2Ω. Such registrations produced stasisfactory alignment after visual inspection and did not produce quantification errors exceeding 10%. Consequently and to provide a more accurate interpretation of the results, the registration success criterion was relaxed to 2Ω (2.70 mm) for the real dataset.

Registration results of O-NMI, H-NMI, and IRIS-NMI (Table 8) were similar to those observed with 30% IIH simulated data. Similarly, the combination of iterative correction and SMI registration led to registration success rates close to 100% for all cases but one (animal one). Notwithstanding the general poorer results produced by O-SMI and H-SMI with real data compared to those observed with simulated data, O-SMI still overperformed O-NMI and increased its average registration success of the real dataset from 30.55% to 34.64%. SMI also leveraged the average success rate of NMI registrations of IIH corrected images from 45.27% (H-NMI) to 51.81% (H-SMI). Finally, superior results were obtained from iterative correction-

registrations with SMI as the joint optimization cost function than with NMI, with average 95.36% and 61.27% success rate, respectively.

Table 8. Successful registration rates of real data without and with IIH correction through entropy minimization and IRIS.

Method	Real data (animal #)										
	1	**2**	**3**	**4**	**5**	**6**	**7**	**8**	**9**	**10**	**11**
O-NMI	23.00	24.00	42.00	63.00	22.00	22.00	38.00	23.00	31.00	25.00	23.00
O-SMI	36.00	20.00	48.00	77.00	26.00	23.00	34.00	40.00	15.00	29.00	33.00
H-NMI	31.00	29.00	74.00	79.00	58.00	1.00	69.00	41.00	15.00	37.00	64.00
H-SMI	31.00	42.00	79.00	100.00	28.95	1.00	68.00	78.00	17.00	28.00	97.00
IRIS-NMI	47.00	73.00	34.00	79.00	28.00	63.00	75.00	62.00	56.00	78.00	79.00
IRIS-SMI	66.00	94.00	100.00	100.00	95.00	96.00	100.00	100.00	99.00	100.00	99.00

Registration accuracy was poorest with IIH-artifacted images and NMI leading to an average error of 2.22 mm for the entire dataset. After correction by means of H minimization, the average NMI registration error was reduced to 2.08 mm and further improved through IRIS (2.04 mm). Poorest accuracy results with SMI were also obtained from registrations of IIH-artifacted images (2.09 mm) but were superior to O-NMI and close (+0.01 mm) to H-NMI. After H-minimization correction, H-SMI accuracy improved and generated an average 2.00 mm registration error for the entire dataset. IRIS-SMI was the strategy yielding the most accurate results, with 1.94 mm average registration error. Visual inspection of successfully registered image pairs confirmed the finer alignment obtained with SMI and the iterative strategy compared to separate IIH correction and registration. It was observed that accuracy differences between methods were mainly caused by rotational shifts as observed in Fig. 32.

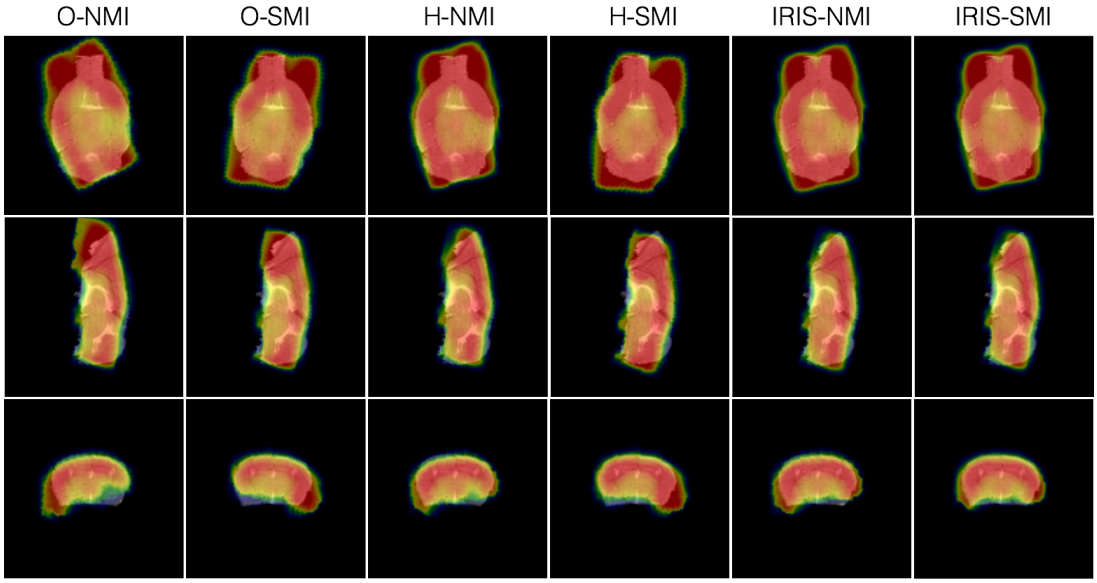

Figure 32. (Top row) Coronal, (middle row) saggital, and (bottom row) axial 2D planes of MR-PET registrations of the same animal and initial misalignment with the different methods. The registration error of each registration was: 2.55 mm (O-NMI), 3.17 mm (O-SMI), 1.67 mm (H-NMI), 2.63 mm (H-SMI), 1.42 mm (IRIS-NMI), and 0.48 mm (IRIS-SMI).

4.3.3. Quantification

Scatter plots are shown in Fig. 33 to assess the impact of registration error in whole brain 18F-FDG PET quantification of the real dataset. Registrations of uncorrected data yielded a wide span of registration and quantification errors. However and after correction with either method, registrations generally produced either accurately aligned or completely non-overlapping brain volumes. In particular, results showed that up to 5 mm, quantification errors below 10% were obtained with all methods after. Beyond this point quantification errors produced with NMI for both IIH-artifacted and IIH-corrected images rapidly increased up to 100%. These registrations found an NMI optimum with images background alignment and no overlap whatsoever of brain areas. A small subset of cases was observed for O-NMI (<0.01% - 1/1,100), O-SMI (<0.01% - 1/1,100), H-NMI (1.64% - 18/1,100) and IRIS-NMI (2.18% - 24/1,100) where large registration errors, i.e. greater than 10 mm, generated small quantification errors close or even below 5%. Such cases corresponded majorly to rotational errors implying large FRE but otherwise low quantification errors of whole brain tissue. In two cases, registration led to a complete flip of the images in one of the axis (registration error ~20 mm). Errors between 6 and 10 mm corresponded to registrations being trapped in local optima and specifically for one animal (number one). After excluding these cases, for those registrations associated to quantification errors below 5% iterative methods IRIS-NMI and IRIS-SMI generated maximum registration errors of 3.34 and 2.80, respectively, compared to H-NMI (5.36 mm) and H-SMI (4.88 mm).

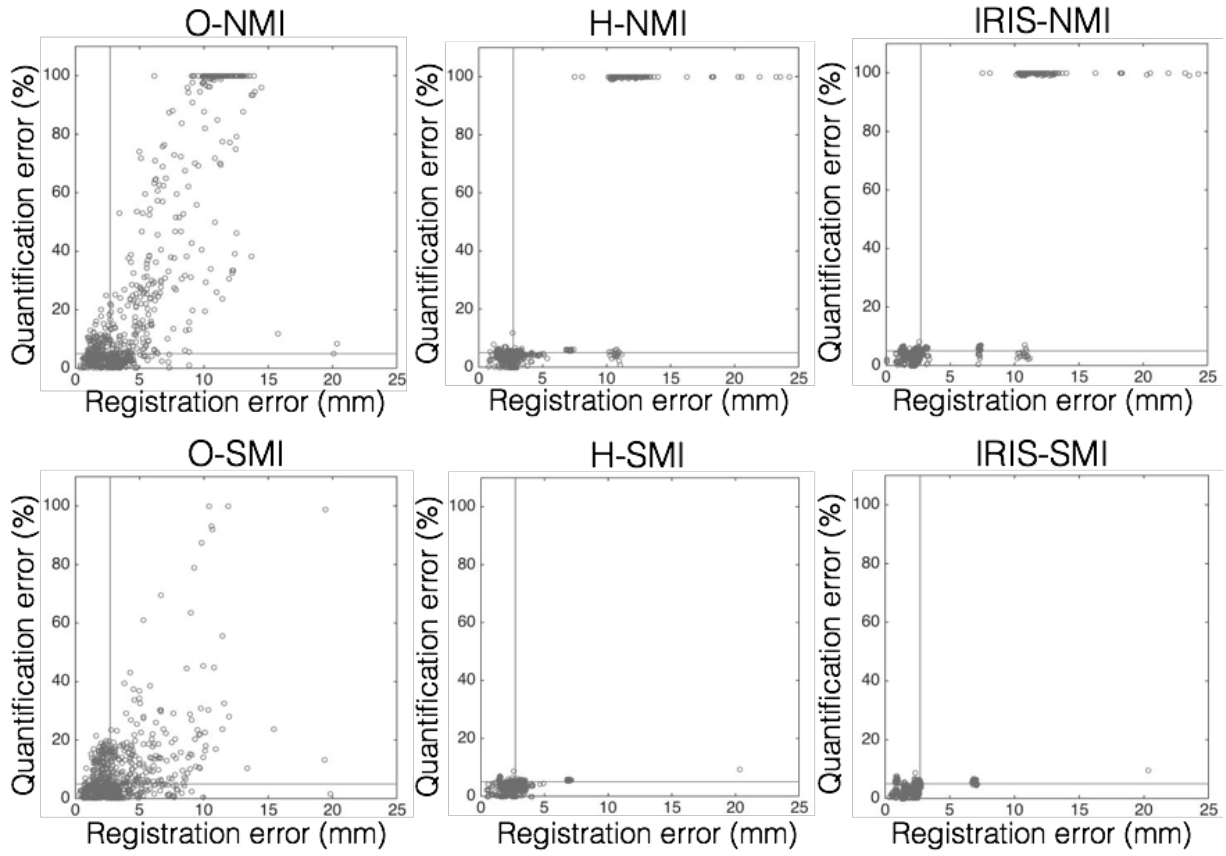

Figure 33. Scatter plots showing PET quantification error vs registration error for all evaluated strategies. The vertical solid line is located at 2.70 mm (Ω), the limit established to determine registration success. The horizontal solid line is located at a 5% quantification error as the limit for accurate quantification.

Fig. 34 shows scatter plots to find correspondences between quantification results of NMI and SMI registrations of real IIH-artifacted images (O-NMI, O-SMI), separate correction and registration methods (H-NMI, H-SMI), and the iterative approaches (IRIS-NMI, IRIS-SMI). Improved quantification results were observed with both H-NMI and H-SMI, which reduced the number of cases with quantification errors below 5% in 18.36% (202/1,100) and 34.09% (375/1,100), respectively. Nonetheless, in 11.55% (127/1,100) of cases H-NMI produced quantification errors of 100% for O-NMI errors below 5%. Again, these registrations responded to complete misalignments of brain FOVs, which could not be successfully registered by means of IRIS-NMI either, and that led to a 6.81% (75/1,100) net quantification improvement of H-NMI with respect to O-NMI. H-SMI registrations accomplished high FOV-overlap in all cases, which explains that all quantification errors were below 10%. With IRIS-NMI and IRIS-SMI, quantification errors were shifted to lower values as observed by a denser cloud of points below the symmetry line in (Fig. 34, right plots), and as represented by the median differences of the quantification errors of each method: 4.18% (H-NMI) vs 3.97% (IRIS-NMI), 3.68% (H-SMI) vs 3.48% (IRIS-NMI).

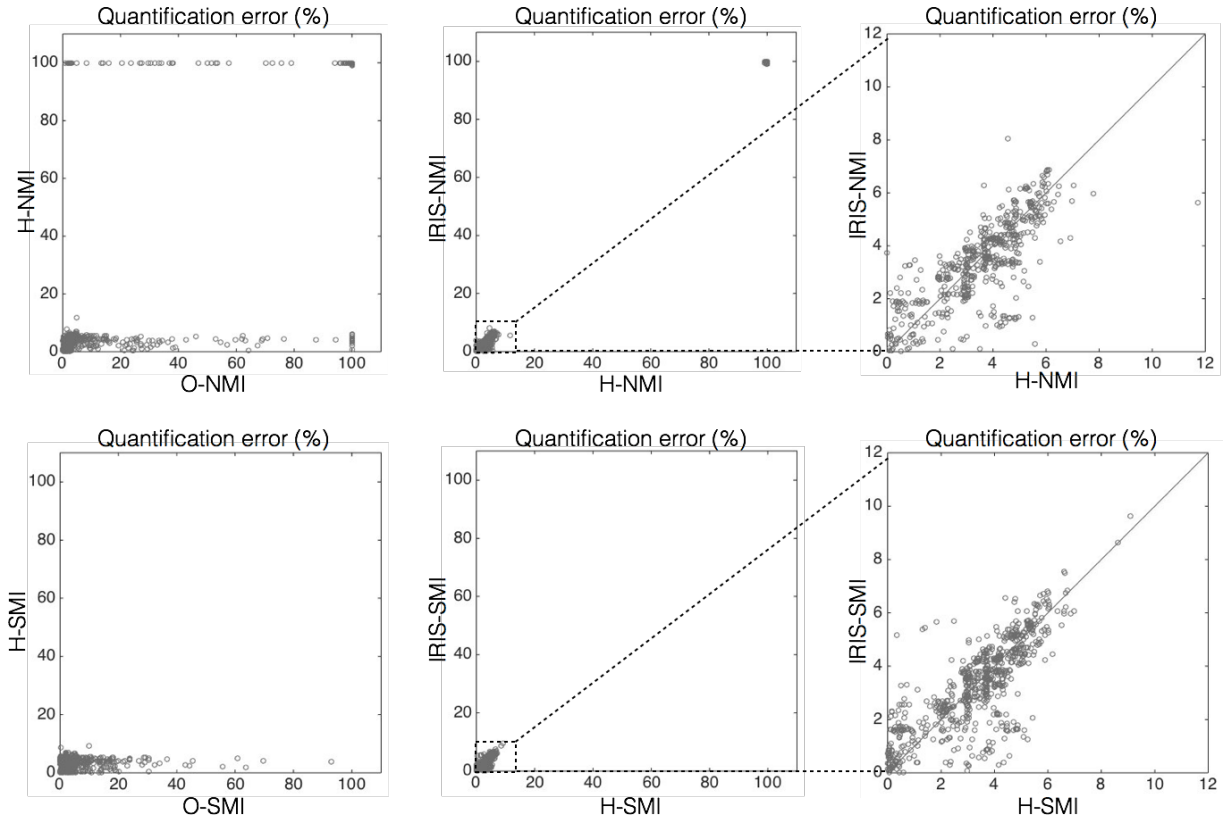

Figure 34. Scatter plots showing PET quantification error correspondences between NMI and SMI registrations of IIH-artifacted, IIH-corrected and IRIS-corrected images. The unity function is represented by the solid line.

4.4. Discussion

MR images are inherently affected by intensity inhomogeneities (IIH) that do not generally affect interpretation but that may affect posterior registration, segmentation and quantitative analysis. This type of artifact is more severe in small-animal imaging using higher field magnitudes and is also more detrimental, particularly, in mice brain imaging due to the lower structural information of this organ compared to humans. Hence, the direct application of IIH correction methods in mice brain MR datasets is neither straightforward nor fully effective since they do not guarantee, for instance, successful registration after correction. Registration accuracy is an essential prior step in most segmentation methods and absolutely necessary for automatic quantification. For this reason, the major contribution of this work is a strategy to effectively correct IIH to secure accurate registration of small-animal brain MRI datasets. An iterative IIH correction and registration strategy (IRIS) is presented that unifies the optimization parameter of both correction and registration stages. The method exploits the shared information between the images to be registered to accomplish intensity corrections that favour registrations performance.

In this study, the image entropy-minimization correction method proposed by (Likar et al. 2001) was implemented for being largely generalizable to a wide range of modalities (Manjón et al. 2007; Knops et al. 2006). And two information-based registration methods were compared, the NMI (Studholme, D. L. G. Hill, et al. 1999), the reference for multimodal human brain registration (Piotr J Slomka & Baum 2009) and small-animal imaging of the brain (Vaquero et al. 2001), and the FOV-insensitive SMI previously presented in section *3. Registration of multi-modal neuroimaging datasets by considering the non-overlapping field of view into the NMI calculation*. However, because strategies do not rely on specific algorithms, methods of different nature than those used herein may be used for correction and registration.

IIH correction by means of H minimization produced visually satisfactory results and similar (<1% difference) entropy and CV results than the iterative strategy. Nonetheless, the iterative strategy translated such small variations in an average 16.00% and 43.55% success rate improvement of real data NMI and SMI registrations (Table 8), respectively. These improvements are explained by the fact that iterative IIH correction accomplishes a higher intensity correspondence between the images that smooths the registration cost function. The observed superior performance of IRIS-SMI can be accounted for the superior capture range of SMI, which secured rough alignment of the images in all cases after IIH correction. Inevitably and due to its reduced capture range, NMI found solutions with exclusively background overlap between the images, therefore, far from the true solution and sterilizing the effect of correction in registration accuracy.

IRIS-SMI correction generated CV values marginally worse than IRIS-NMI (Table 5-6). The fact that NMI relies solely on FOV voxel correspondences makes it more sensitive to entropy changes within regions of interest, here the brain, usually located at the FOV centre in medical imaging, and may explain the better correction results yielded by IRIS-NMI. IRIS-SMI uses the full FOV of the images for correction and, therefore, also includes background voxels that do not necessarily overlap between image volumes. While this strategy is essential to secure rough registration alignment, it reduces the sensitivity of the joint entropy to intensity changes in FOV voxels.

The impact of registration accuracy in quantification was evaluated in a real mice brain dataset. Whole brain masks were used to quantify average glucose uptake which were related to measurements obtained from manually registered 18F-FDG PET images to their T2-weighted MRI pair, constituting the ground truth data. It was observed that quantification errors exceeding 10% were associated to registration errors larger than 5 mm, about four times the voxel diagonal of PET images (Ω: 1.35) mm and twice the threshold set to define registration accuracy (2Ω: 2.70 mm). However, rotational misalignments yielding inaccurate registration results do not necessarily yield inaccurate quantification results, i.e. above 5%. Should the study have involved masks of regions within the brain, larger quantification errors would have been associated to smaller

registration errors. In this scenario, the performance of IRIS-SMI would presumably be more relevant since it has been the correction-registration strategy producing the most accurate correction and registration results. Such analysis should be done in conjunction with an impact assessment study of the strategies presented in this study regarding automatic segmentation accuracy of brain tissues, which deserves special attention.

The superior performance of IRIS over separate correction and registration alternatives comes at the expense of larger computation times. IRIS correction-registration was performed in an average of three iterations (5 min/each) or the equivalent of 15 minutes for the real dataset in a MacBook Pro with 2.6 GHz processor and 8GB of RAM memory, which contrasted with the 2-minutes separate H-minimization correction and registration alternatives. The correction stage demanded most of the computational time since optimization involves building a 2D images joint histogram to compute either the NMI or the SMI cost function as opposed to the 1D image histogram needed in image entropy minimization (and both alternatives using the Nelder-Mead optimization algorithm (Nelder & Mead 1965)). Such computation time may be reasonable for research purposes but should be reduced for its applicability in the clinical setting.

4.5. Conclusions

A novel iterative mice brain MR intensity inhomogeneity correction-registration strategy (IRIS) was presented. IRIS unifies the cost function of the correction and the registration stages producing improved correction, registration and quantification results of a mice brain 18F-FDG PET PET-MR dataset. The reference method proposed by Likar based on MR image entropy minimization was used to maximize the NMI between the images to be registered, which was also used as the registration method. IRIS provides a solution to small-animal brain MRI datasets suffering from higher-magnitude intensity artefacts than those observed and broadly addressed in human brain MRI.

5. Partial volume correction using an energy multiresolution analysis

5.1. Introduction

The fundamentals of partial volume effect (PVE) inherent to Positron Emission Tomography (PET) were describred in section *1.6.2.b. Partial Volume Effect in PET*. PVE implies a loss of image resolution and a cross-contamination of the activity concentration in neighbouring voxels and regions that hinders accurate quantification. PVE correction (PVC) becomes most necessary in quantification studies of thin or small-volume structures, such as the human cerebral cortex, only ~2 mm thick (Kruggel et al. 2003). As an example of the detrimental impact of PVE on the interpretation of imaging studies, it can be pointed out that the cortex hypometabolism was observed in a sample of healthy elder subjects studied with 18F-FDG PET (Curiati et al. 2011). Before PVC low glucose uptake was associated to reduced cerebral blood flow (CBF). However and after PVC, hyometabolism was attached to cortical atrophy, a normal effect in aged people. A true glucose metabolism reduction was instead observed in Alzheimer's disease (AD) patients after PVE correction (Ibanez et al. 1998).

A myriad of PVC techniques have been devised and several classification schemes exist. The classification followed in (Erlandsson et al. 2012) discriminates between region-based and voxel-based methods and is the one used here. Region-based methods aim solely at correction for quantification of a certain area and, therefore, do not produce PVC images. Voxel-wise methods aim at both correction and resolution recovery of the entire image.

5.1.1. Region-based methods

5.1.1.a. Recovery Coefficient

The Recovery Coefficient (RC) is that numerical factor that corrects the average true activity of a delineated region (Hoffman et al. 1979). RCs are first obtained from phantoms of known geometry and object-to-background (OTB) activity. Implicitly, this method can only correct for spill out activity. However, spill in activity can be corrected in phantoms with "hot" background surrounding "hot" or "cold" objects. Generally, RCs are calculated over spherical structures that can be later found in human anatomy, such as small-volume spherical tumors or cancer nodules. Because tumors can be of different sizes and of different OBTs, RC curves can be drawn for different OTBs with respect to object, i.e. tissue, diameter. Notwithstanding its simplicity, RCs are hardly applicable in clinical practice due to the limited reproducibility of phantom results in clinical data. First, it is impracticable to obtain RCs of any size and OTB. Second, the method is user-dependent with the RC being dependent on the accuracy of the ROI delineation in the patient data. And third,

accurate tissue ROI delineation is impossible in the absence of an anatomical reference, not always available in clinical settings using stand-alone PET systems.

5.1.1.b. The Geometric Transfer Matrix method

When an anatomical reference or atlas with pre-determined ROIs is available, the RC method can be extended to obtain coefficients from multiple anatomical regions that also take the spill-in effect into account. The system PSF is estimated and used to simulate real spill over effects, ω_{ij}, between ROIs (or RSFs) and a linear model is generated that relates the contribution of true activity, T, in each ROI to each other, i.e. $M = \omega\, T$. Therefore, the true average activity of a given set of regions can be computed as the inverse of this linear model, i.e. $T = \omega^{-1}\, M$. This method is known as the Geometric Transfer Matrix (GTM) method or the method of Rousset (Rousset, Ma, et al. 1998), who first applied it to 18F-FDG PET of the brain.

5.1.1.c. Reconstruction-based methods

Reconstruction-based methods work on the forward-projected data or sinogram built from the integrated LOR registered during acquisition. A ROI delineated in an anatomical reference is forward-projected to the sinogram space and the average activity concentration is iteratively estimated in a maximum likelihood-expectation maximization (ML-EM) framework (Moore et al. 2012; Carson 1986). Correction aims at finding the *most likely* activity wihtin the ROI through maximization of a probabilistic model factored into image projections, the *expected* voxel contributions to projections, the Poisson distribution of noise, and the system PSF. This method is particularly fast given the fact that correction is only accomplished for a set of projections as well as the reduction of computation cost associated to backprojection, or reconstruction.

5.1.2. Voxel-based methods

5.1.2.a. Reconstruction-based methods

Voxel-wise reconstruction-based methods are conceptually equivalent to region-wise reconstruction-based methods differing only from the fact that correction is performed on backprojected data and that, albeit the need for registration to an anatomical image, no segmentation is required. Despite demanding a higher computational cost, these methods qualitatively and quantitatively improve the quality of PET images and, as a result, are widely-implemented and used in current PET-CT scanners (Sureau et al. 2008; Bowen et al. 2013; Orlandini et al. 2013; Andersen et al. 2013). More recently, the time-of-flight (TOF) information of the scattered photons enables anhilation localization along the LOR and enhances the correction performance during the reconstruction process (Schaefferkoetter et al. 2013; Prieto et al. 2013).

5.1.2.b. Partition-based methods

Partition-based methods can be regarded as the counterpart of the GTM region-based method. These methods also require registration to an anatomical reference and segmentation of the tissues of interest. Distinctly, correction is done at the voxel level and therefore, PVE corrected images are produced. (Videen et al. 1988) first and (Meltzer et al. 1990) next suggested that correction could be accomplished by means of dot division of the PET degraded image by the system's PSF. This method was later improved by Müller-Gärtner (MG) (Müller-Gärtner et al. 1992), who extended the correction model to include the three major segmented brain tissues GM, WM, and CSF. The MG model assumes that tissue activity concentration is homogeneus and that WM and CSF activity is known or can be obtained from PVE-free regions. A voxel-wise substraction of PSF-convolved WM and CSF activity from GM ROI corrects for spill in effects. Next, GM-corrected ROI is dot-divided by the PSF-convolved GM ROI to correct for spill-out. The method can also accommodate for the study other brain ROIs of interest within GM, e.g. basal ganglia (Meltzer et al. 1996). First, GM-corrected activity is estimated and then a fourth compartment is included in the model to produce a local voxel-wise correction and estimate the average activity of the ROI. To overcome the assumption that WM and CSF activity values are PVE-free, Rousset et al. (Rousset, Y, et al. 1998) proposed to estimate their values via the GTM method. The method proposed by Alfano (Alfano et al. 2004) differs only from MG in that WM activity is not estimated only from a point or region, but all WM voxels are used to correct for spill-in in GM. As with GTM, a multi-ROI approach with estimated cross-contamination coefficients between ROIs was developed by (Yang et al. 1996) to extend the applicability of the MG method to several GM substructures.

5.1.2.c. Deconvolution methods

A PET image can be regarded as a high-resolution image of a certain biomarker blurred by the PSF of the scanner plus additive Poisson noise. First deconvolution methods address PVE correction and PET spatial resolution recovery through minimizaton of voxel-wise differences between the original degraded PET image and the PSF-convolved true PET image in a least squares sense according to the Van Cittert algorithm (Wu et al. 1994). At each iteration, such images differences contain structural information that is reintroduced into the degraded image for restoration. The corrected image is then blurred until the voxel-wise difference with the original image is minimal. The original PET image is used as the true image for initialization and an additional blurring of the image details is included at each iteration to avoid noise amplification. The Richardson-Lucy is also a deconvolution-based method (Richardson 1972) that is conceptually similar to voxel-wise reconstruction-based methods. This method is framed in an iterative ML-EM strategy that assumes the Poisson probability distribution nature of noise and aims at finding the correction that, after PSF convolution, maximizes the probability of producing the original image.

5.1.2.d. Multiresolution approaches

An alternative to deconvolution methods to inject structural information of anatomical images (MR or CT) into registered PET images is provided by multiresolution approaches. These methods use the wavelet transform to deaggregate the low- and high-frequency information throughout arbitrary resolution levels. After decomposition, the high-frequency information at the deepest decomposition level is combined with the PET wavelet coefficients according to a pre-defined model. The mutual multiresolution analysis (MMA) proposed by (Boussion et al. 2005) establishes a linear realtionship between PET and MR registered coefficients, which is not commonly given in multimodal imaging. While the applicability of this method is limited, it set the basis to other methods seeking for a wider and more robust applicability of the strategy. (Shidahara et al. 2009) developed a more complex model with factors that accounted for the resolution difference between decomposed images at each resolution level, scaled the intensity differences between images modalities, and weighted the anatomical coefficients versus noise. The set of factors used in this method as well as the use of probabilistic tissue atlases instead of anatomical images relaxed the linearity condition of the method proposed by (Boussion et al. 2005). However, the wide applicability of this method may be questioned given the complexity of the model. A local wavelet coefficient analysis was proposed in (Le Pogam et al. 2011) to weight the anatomical information added to the high-frequency functional coefficients of the PET image. A cubic window rastered the entire wavelet coefficients space in both images and computed the median between them. An arbitrary threshold was set to prevent low coefficient values in the anatomical image to avoid extreme values. Distinctly, this method produced PVE corrected images that significantly reduced artefactual corrections caused by anatomical structures with little activity in brain PET images, e.g. bone.

5.1.3. State of the art limitations and proposed solution

PVE correction is important aspect of quantitative analysis in emission tomography, which remains an area of active research. Even though in most real-life situations correction of particle volume bias is only an estimate, as some assumptions are always needed, it is an important correction to ensure that measurements are truly quantitative and which generally improves their accuracy. As multimodality systems become more widespread accessible, the availability of PVE corrections to the end-user is expected to increase.

In the event of no surrounding activity concentration, the result of partial volume effect is that small objects appear to have lower radioactivity concentrations in comparison with larger objects with the same concentration. In this case, a Recovery Coefficient (RC) (i.e. the ratio between the apparent and true activity concentration) can be estimated as long as the object geometry is provided by a structural imaging modality and if the blurring effect resulting from the limited spatial resolution of the scanner is known. However, in

general, to accurately estimate the activity concentration is a complex problem to resolve because of potential heterogeneities in the tracer concentration in the target tissue and as it is also necessary to correct for the activity spillover from surrounding tissues.

In spite of the amount of work and accomplishments, the applicability of PVC methods is still very limited to other image modalities than those used for validation, ultimately restricting their clinical and research use. This fact may explain the numerous extensions and modifications of original methods and the different correction strategies developed so far.

In this work, a fully data-driven PET correction strategy implemented in a multiresolution wavelet framework is presented. The method exploits the resolution recovery capabilities of MMA approaches and implements correction as an energy-balance multiresolution approach to correct PET wavelet coefficients for spill over and spill in effects.

5.2. Materials and Methods

5.2.1. Wavelet transform and multiresolution image analysis

Wavelet transform

The wavelet transform decomposes the image into its frequential and spatial components by means of temporal convolution to a *wavelet* filter. There are several wavelet bases from which wavelet filters may be synthesized that, for an efficient representation of the image information in the wavelet domain, should fulfill the following properties (Ruttimann et al., 1998): (1) noise preservation; (2) shift invariance; (3) high image features decorrelation/classification capabilities; and (4) accurate features localization. S*ymmlets* are symmetric filters that fulfill conditions (1) and (2). However, a trade-off needs to be reached for the fulfillment of properties (3) and (4). On one hand, the decorrelation capabilities of a filter depend on its number of vanishing moments, i.e. derivatives. On the other hand, its support size (or length) also increases with the number of vanishing moments, which worsens the spatial localization of the signal (Mallat 1999). After a first comparison study with phantoms involving several wavelet bases (Desco et al. 2001), Desco et al. concluded that symmlet filters of order 4 provided a satisfactory trade-off between sensitivity to signal and signal localization. In (Desco et al. 2005) these filters were used to analyze the activation differences of the thalamus in simulated PET image datasets, and are the wavelet filters used herein.

Multiresolution framework

In this work, the widespread decomposition scheme proposed by (Mallat 1989) has been implemented although other multiresolution approaches may be found in (Boussion et al. 2005; Le Pogam et al. 2011;

Shidahara et al. 2009; Merlin et al. 2015). In a 3D discrete wavelet transform (DWT), low-pass and high-pass wavelet filters are synthesized from the wavelet base, or mother wavelet, to separate low-frequency and high-frequency wavelet sub-bands (Fig. 36). When implemented in a multiresolution framework, images are filtered and then subsampled at a rate 1/2 along one dimension producing one low-pass filtered ($w_{1,1}(x,y,z)$) and one high-pass filtered ($w_{1,2}(x,y,z)$) wavelet sub-bands of a lower resolution level along the filtered dimension (Mallat 1989). This process is iterated for the two wavelet sub-bands along a second dimension and again along the third dimension. At the end of the decomposition process of a 3D image, the output of the transformation consists of eight wavelet sub-bands of size $N_x/8$ x $N_y/8$ x $N_z/8$, with N_d the original image size along dimension *d*. Out of the eight wavelet sub-bands, one has been low-pass filtered along the three dimensions ($w_{1,1}(x,y,z)$) and another one high-pass filtered also along the three dimensions ($w_{1,8}(x,y,z)$). The remaining six have been filtered along one or two dimensions. In each wavelet sub-band wavelet coefficients represent local functional or structural information changes along one, two, or three dimensions at a scale half the original image, as a result of subsampling. When implemented in a multiresolution framework, the 3D-DWT is perfomed over the wavelet sub-bands until an arbitrary decomposition level (J) is reached. As a result, at deeper decomposition levels wavelet coefficients convey functional and structural information of larger structures in the original image, with $w_{J,1}(x,y,z)$ mostly bearing functional or average intensity information of the original image. For reconstruction, each of the eight wavelet sub-band sets are first zero-interleaved at a rate 1/2, and then filtered, and summed. Note that to avoid loss of any kind after reconstruction, decomposition and reconstruction filters meet orthogonality and orthonormality (Vetterli & Cormac 1992).

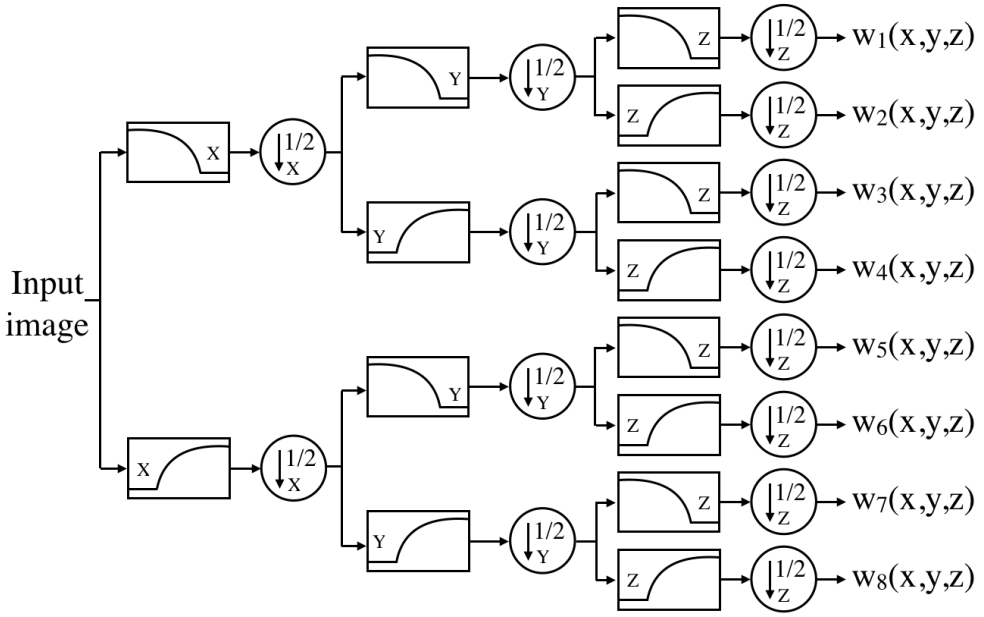

Figure 35. Diagram of the three-dimensional discrete wavelet transform (3D-DWT). Wavelet decomposition low-pass and high-pass filters and subsequent sub-sampling at a rate 1/2 are applied along dimensions x, y, and z, respectively.

5.2.2. Energy-balance multiresolution approach

Energy balance

An ideal PET image (PVC) should convey PVE-free functional information. To translate these requirements into a multiresolution analysis the corrected PET image should preserve the functional information (low-frequency sub-bands) and incorporate the structural information (high-frequency sub-bands) of its registered MR counterpart. In addition, the corrected PET image should also preserve the energy balance between the MR image low and high frequency sub-bands r_j^{MR} throughout all resolution levels:

$$r_j^{PVC} = r_j^{MR} = \frac{E_{j,1}^{MR}}{\sum_{k=2}^{K} E_{j,k}^{MR}} \quad K: number\ of\ sub-bands\ at\ level\ j \tag{21}$$

Decomposition level determination

At high resolution levels, high-frequency sub-bands $w_{j,k}(x,y,z)$ with $k>1$ confine high detail information and high frequency noise, with most of the energy being accummulated in the lowest frequency sub-band $w_{j,1}(x,y,z)$. However, as the decomposition level increases the energy distinctly deaggregates across sub-bands, now representing larger structures in the image, and a marked energy increase of high-frequency sub-bands and energy reduction of low-frequency sub-bands is observed. Such energy deaggregation is, therefore, characteristic of each image and allows identification of the relevant sub-bands at the corresponding level

(Fig. 37). Therefore and to determine the spectral signature of the image, maximum deaggregation should be accomplished and it is produced at the deepest level where all sub-band dimensions exceed twice the wavelet filters support (or length) meeting, thus, the Nyquist-Shannon theorem (Shannon 1949).

$$N_h < 2 \times N_{sb}^d \tag{22}$$

With N_h the wavelet filter length and N_{sb} the sub-band size along dimension d.

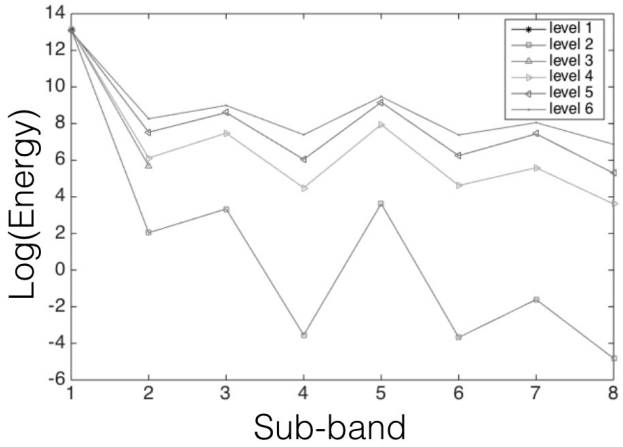

Figure 36. Sub-band energy distribution across decomposition levels. Larger energy deaggregation (or reduced energy contrast between low and high frequency sub-bands) is observed with increasing decomposition level.

Wavelet coefficients selection

Understanding that the relevance of each sub-band can be measured as its energy relative to the original image, the relevance between sub-bands of different images can be compared by means of their relative energy. Alternatively, the absoulte energy of sub-bands could be compared should the anatomical image be first scaled to the functional image previous to decomposition. Whenever the energy of the wavelet coefficients in a particular sub-band of the PET image is larger than the same sub-band in the MR image, it should be reasonable to state that the PET sub-band contains more relevant functional information than the structural information conveyed by its MR sub-band counterpart. And viceversa, an MR sub-band with higher energy than its corresponding PET sub-band indicates that there is little relevant functional information compared to the structural information conveyed in the MR sub-band. Therefore, correction can be accomplished by means of selecting the coefficients of those sub-bands with the highest energy so that the most relevant functional information is retained and the most relevant structural information is included to correct for partial volume effects. Nonetheless, the wavelet coefficients of the low frequency sub-band of the deepest decomposition level $w_{J,1}(x,y,z)$ should be those of the PET image given that they represent the mean activity values of the imaged biological process.

$$if\ E_{j,k}^{PET} >= E_{j,k}^{MR},\ w_{j,k}^{PVC} = w_{j,k}^{PET}\ else\ w_{j,k}^{PVC} = w_{j,k}^{MR},\ k > 1 \quad (23a)$$

$$w_{j,1}^{PVC} = w_{j,1}^{PET},\ J: deepest\ decomposition\ level \quad (23b)$$

This correction strategy implies a misbalance between the low and high frequency sub-bands that can be corrected by means of applying a factor to the low energy sub-band that restores the MR energy balance between low and high frequency sub-bands r_j^{MR}. This factor (eq. 24a,b) can be calculated as the cummulative sum of the amount of relative energy of high frequency sub-bands after correction over the MR high frequency sub-bands energy, as follows:

$$E_{j,1}^{PVC} = \alpha_j \times E_{j,1}^{MR},\ j: decomposition\ level \quad (24a)$$

$$\alpha_j = \frac{\sum_{k=2}^{K} E_{j,k}^{PVC}}{\sum_{k=2}^{K} E_{j,k}^{MR}} \quad (24b)$$

Decomposition tree

The number of wavelet sub-bands grows at a rate 8^j with j the decomposition level and for typical brain images with in-plane dimensions 256 x 256, the number of sub-bands at the maximum decomposition level J is of 262,144. However, most of the sub-bands have very little energy, particularly high-frequency sub-bands at low decomposition levels, and can be disregarded with negligible effects in the reconstructed image (Fig. 38). Therefore, decomposition can be limited to sub-bands exceeding a certain energy level to reduce the computational burden associated to convolution/deconvolution processes. After reconstruction with the minimim between (a) the sub-bands of highest energy in the decomposition level that accummulate 99% of the original image energy and (b) the eight sub-bands with highest energy at each decomposition level, the sum of square differences SSD of the original and reconstructed images over the original image energy produced values in the order of 1e-5 with unnoticeable differences between them (Fig. 39). As a final note, anatomical images should be resliced to their highest resolution along each dimension to reach the deepest possible decomposition level where sub-bands energy can be maximally deaggregated. Next, the functional image should be resliced to the same dimensions as the anatomical image so that they can be combined for correction.

The three-dimensional DWT procedure was coded with MATLAB software (The MathWorks Inc., Natick, MA, USA) using, in part, routines downloaded from http://taco.poly.edu/Wave- letSoftware/dt3D.html (Selesnick & Li 2003).

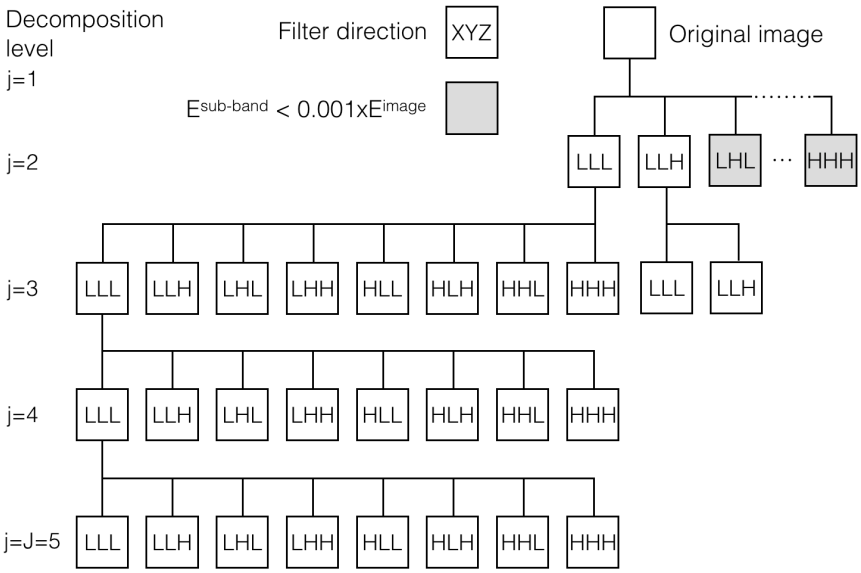

Figure 37. Diagram of a possible decomposition tree with deepest decomposition level 5. Shaded sub-bands represent less than 0.1% of the original image energy and are not used for decomposition/reconstruction. Shaded sub-bands are shown only on the first decomposition level to easy visualitzation.

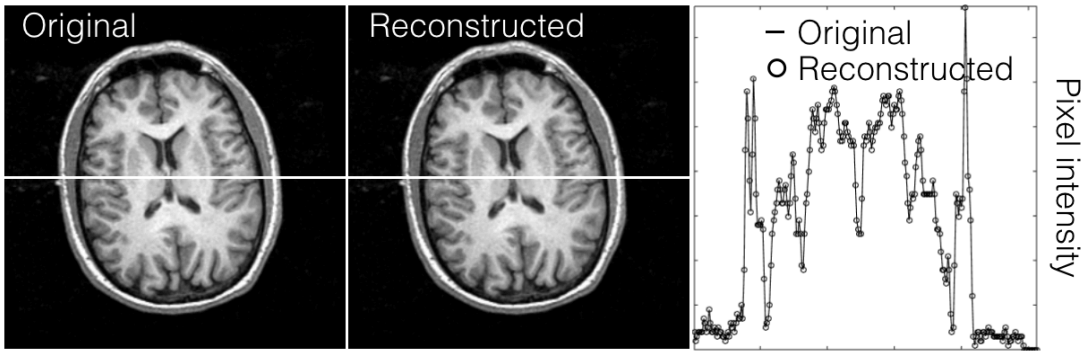

Figure 38. (Left) Brain MR image compared to the reconstructed image (middle) with only a subset of the wavelet sub-bands. On the right, a 2D plot compares the the middel row intensity profiles of an axial plane between the images.

The correction and resolution recovery algorithm can be summarized in the following steps:

1. MR-PET accurate registration.
2. MR resampling to highest resolution dimension resulting in isotropic voxels.
3. PET resampling to MR image dimensions
4. MR energy scaling to match PET image energy
5. Decomposition level (J) determination (Nyquist theorem) (eq. 22)
6. PET and MR decomposition until level J

7. Selection of coefficients with maximum sub-band energy (exception: $w_{J,l}(x,y,z) = w^{PET}_{J,l}(x,y,z)$) (eq. 23a,b)
8. Energy balance of PET wavelet sub-bands to match high-frequency sub-bands energy distribution of MR (eq. 24a,b)
9. Reconstruction

5.2.3. Evaluation

5.2.3.a. Datasets

Phantom

A set of five digital spheres placed in a circular arrangement and of decreasing diameter (50 mm, 30 mm, 20 mm, 10 mm, 5 mm) was used first to assess the performance of the method as similarly done in (Boussion et al. 2005). 50 mm-, 30 mm- and 20 mm-spheres had decreasing intensities (100, 80, 60, respectively) to study spill-over effects wheras 50 mm-, 10 mm-, and 5 mm-spheres had the same intensity (100) to consider tissue-fraction effects and the recovering of small areas. Images were 128 x 128 x 63 in size with 1mm isotropic voxel dimensions. Next, PVE effects were simulated in the phantom image following (Desco et al. 2005), as described below. Regions of interest (ROIs) of same exact dimensions were obtained for each sphere and from the background by means of binary thresholding. Average and standard deviation (SD) values were obtained from each ROI before and after correction. Recovery coefficient values were calculated by dividing average ROI values to original intensities.

Simulated data

18F-FDG PET images were created from brain tissue probability maps included in SPM package following the method described in (Desco et al. 2005) and shown in Fig. 39. Gray matter, white matter and CSF probability images were multiplied by corresponding factors and added together to create a composed tissue image with tissue contrast resembling that of normal 18F-FDG PET images. The image was the filterprojected using the Radon transform and the synogram was obtained. After the number of counts was elevated to common 18F-FDG PET counts, the synogram was decimated at a 2:1 ration and Poisson noise added. Next, the synogram was scaled back to original intensity ranges by dividing by the 18F-FDG PET scaling factor used previously. Finally, the synogram was backprojected and the resulting image smoothed in all image dimensions with a Gaussian filter with FWHM of 7.5 mm, common of human PET scanners (Fig. 40).

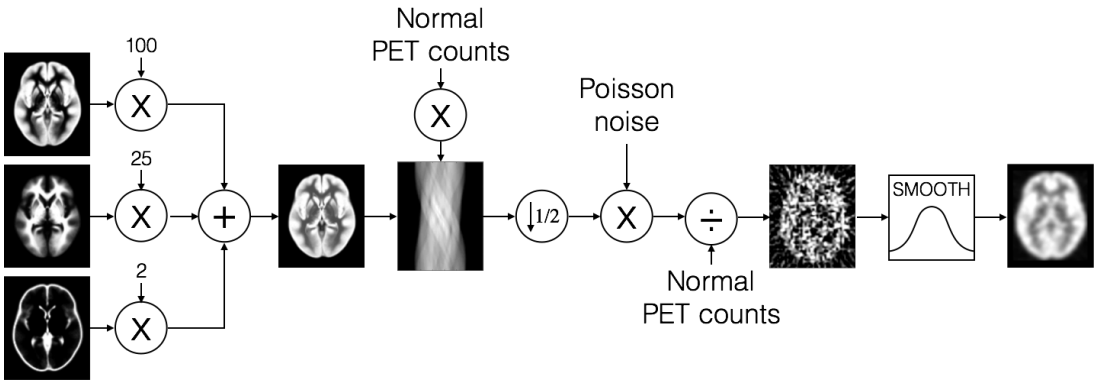

Figure 39. Diagram showing the process to simulate 18F-FDG PET images. A value of 1e6 counts was used prior to introducing Poisson noise into the image sinogram and a FWHM of 7.5 mm was used to smooth the image.

Clinical data

In order to test the robustness of the method to correction with different MR modalities, clinical PET-T1, PET-T2 and PET-PD images of patient two of the RIRE dataset who underwent tumor resection were used. MR data had a nominal voxel size of around 1.25 mm with 256 x 256 in-plane pixels with 26 4 mm-thick slices (West, J. M. Fitzpatrick, et al. 1997) and were resliced to 256 x 256 x 256 with 1.25 mm isotropic voxel dimensions. PET images had original voxel size of 2.6 x 2.6 x 8.0 mm with 128 x 128 x 15 matrix size but were resliced to MR image and voxel dimensions. Images were registered with registration errors below the voxel diagonal as externally provided by the RIRE server. The patient had brain lesions occupying significant volume of the right frontal lobe, visible in all MR modalities. This dataset can be freely downloaded from the "Retrospective Image Registration Evaluation (RIRE) project" website (http://www.insight-journal.org/rire/).

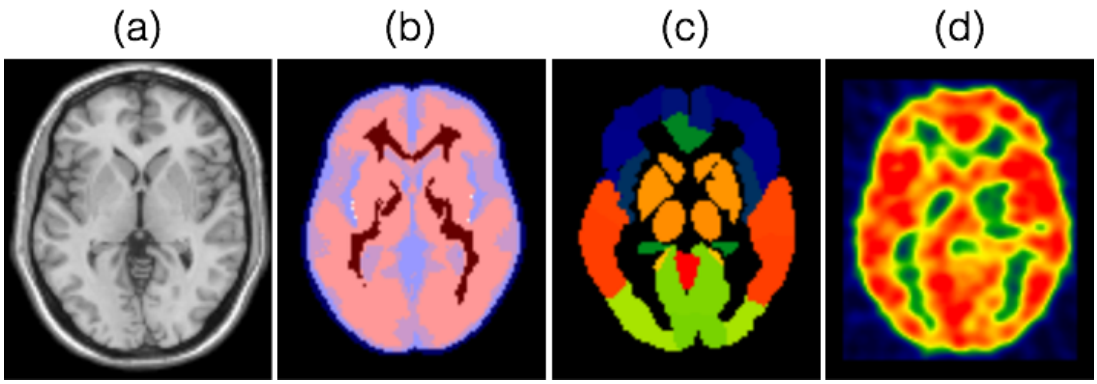

Figure 40. 2D view of same corresponding plane in (a) single-subject T1 template, (b) main tissue masks, (c) automatic anatomic labelling atlas, and (d) simulated 18F-FDG PET.

5.2.3.b. Qualitative and quantitative assessment

PET simulated image of phantom data was corrected with the phantom original image containg the true values. Binary masks were used to calculate average intensity values for each sphere in true, simulated and corrected images.

The simulated 18F-FDG PET image was corrected using the single-subject T1 template also included in SPM package. Gray matter, white matter, and CSF binary masks were generated from SPM tissue probrabilty maps, after disregarding voxels with probabilities below 5% of belonging to a certain tissue (Fig. 40c). The Automatic Anatomical Labelling (AAL) atlas also included in the SPM package contains manually segmented ROIs drawn over the single-subject T1 template and was used to calculate average ROI values in the 18F-FDG PET simulated and corrected images (Fig. 40d).

PVE correction was measured by means of the RC, which is calculated as the ratio between the intensity value at the region of interest divided by the true or theoretical value (Boussion et al. 2005; Shidahara et al. 2009; Le Pogam et al. 2011). It was applied on the phantom, synthetic and simulated data since no ground truth data is available from the rire dataset. In addition, a Bland-Altman analysis was performed for the simulated data. Instead and for the real dataset, a qualitative analysis was accomplished to examine the robustness of the method to using MR images obtained of different modalities.

5.3. Results

5.3.1. Digital phantom

True, simulated and corrected images of the digital phantom are shown in Fig. 41. Full resolution recovery for all sphere sizes as well as background noise removal was observed in the corrected image.

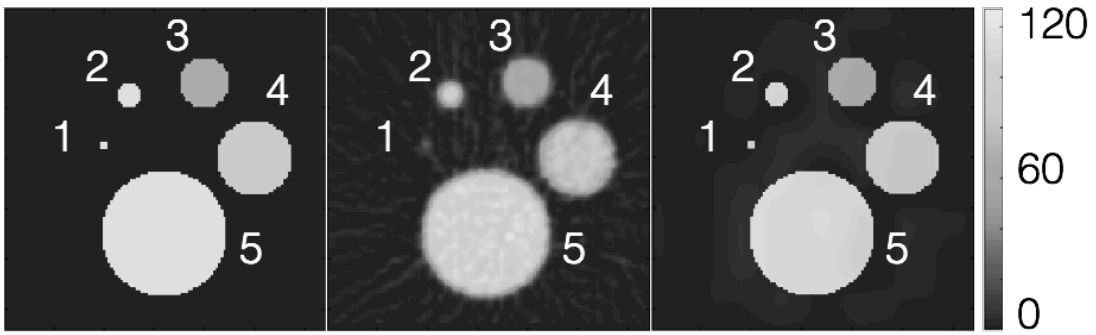

Figure 41. 2D planes showing digital phantom spheres in (left) original, (middle) simulated, and (right) corrected images.

Recovery coefficient values approached 100% for all sphere sizes in the corrected image while the partial volume effect, mostly caused by spill out effects, was more remarkable the smallest the sphere dimensions. For the largest sphere, the loss of activity after simulation was non-significant as shown in Table 9. Correction also produced more uniform values as reflected by the lower standard deviation (SD) of spheres intensities. Only sphere 1, the smallest in size, had a larger intensity variability after correction.

Table 9. Mean (SD) and recovery coefficients of synthetic image with digital spheres.

	True	Simulated		Corrected	
	Mean	Mean (SD)	RC(%)	Mean (SD)	RC(%)
Background	0	1.64 (4.67)	N.A.	1.03 (1.19)	N.A.
Sphere 1	100	20.19 (3.84)	20.19	96.67 (8.09)	96.67
Sphere 2	100	67.18 (19.34)	67.18	96.87 (5.01)	96.87
Sphere 3	60	52.09 (12.84)	86.81	59.03 (2.92)	98.39
Sphere 4	80	73.43 (14.51)	91.78	78.15 (2.92)	97.69
Sphere 5	100	98.36 (15.11)	98.36	99.73 (3.17)	99.73

5.3.2. Simulated data

Axial views of spatially aligned simulated, single-subject T1 template, and corrected images are shown in Fig. 42. T1 resolution is observed in the recovered folding patterns of cortical regions in the corrected image and the higher contrast between active and inactive regions. Correction also accounts for noise reduction, with noise peaks in white matter regions disappearing in the corrected image (Fig. 42 - column 5). Although the cranium is observed in the corrected image and is not present in the simulated image, the brain activity distribution of the simulated image is preserved after correction.

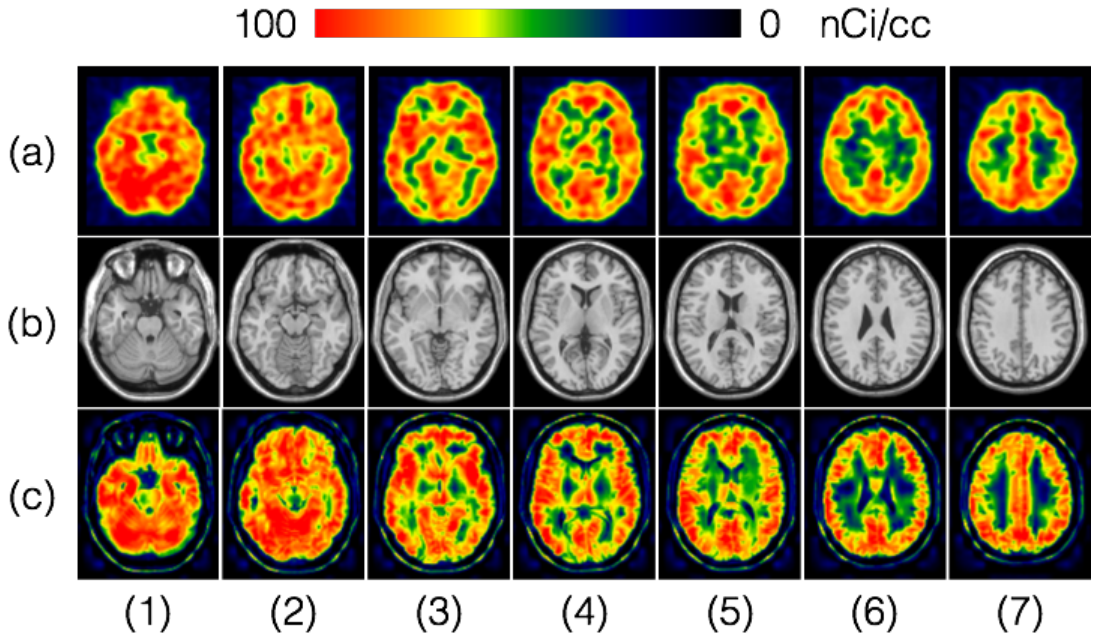

Figure 42. Axial 2D planes of (a) simulated 18F-FDG PET, (b) single-subject T1, and (c) single-subject T1-corrected PET.

Recovery coefficients for 18F-FDG simulated and corrected images are shown in Table 10. Activity corrections of 7.85%, -14.46%, and -42.57% were observed for gray matter, white matter, and CSF, respectively, with correction errors below 10%. Correction increased background noise average intensities (96.30%) and variability (63.91%) in the image, creating a more inhomogeneous pattern as compared to typical PET image background noise (Fig 42, upper and bottom rows).

Table 10. Main tissue values of simulated ground truth data, simulated 18F-FDG image, and corrected image with SPM single-subject T1 image.

Tissue	True	Simulated		Single-subject T1	
	Mean (SD)	Mean (SD)	RC(%)	Mean (SD)	RC(%)
BCK*	9.21 (22.66)	10.17 (20.06)	110.43	19.05 (32.88)	206.73
GM*	112.66 (41.17)	102.81 (28.29)	91.26	111.66 (40.47)	99.11
WM*	35.68 (35.15)	42.33 (30.49)	118.65	37.17 (38.78)	104.19
CSF*	28.52 (27.65)	39.06 (14.64)	136.95	26.92 (20.69)	94.38

*BCK: Background, GM: Gray matter, WM: White matter, CSF: cerebrospinal fluid

Individual RC values for each GM ROI were plotted against their volume (Fig. 43). A global bias close to -10% was observed in the simulated image (Fig. 43, left), as a result of the spill out effect characteristic of gray matter regions (Boussion et al. 2005). After correction the global bias approached zero but ROI paired

average intensity differences increased, as reflected by the larger confidence interval in the Bland-Altman plot in Fig. 43 (right).

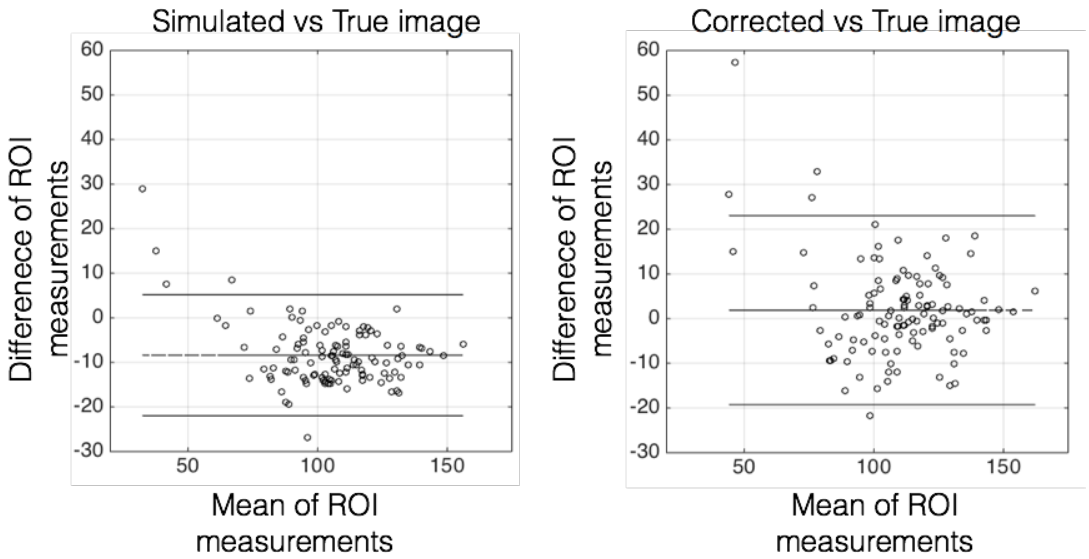

Figure 43. Bland-Altman paired-ROI measurements plot between (left) the simulated and the true image and (right) the corrected and the true image. Upper and lower boundary lines show 95% confidence intervals. Middle line shows average bias between measurements.

In addition, it was observed that ROI corrected regions were closer to perfect recovery the larger the ROI volume (Fig. 44). Similarly, RC values were more dispersed in small-volume ROIs than in larger regions of the simulated image. In a subset of small-volume regions (Pallidum, Putamen, Vermis, Frontal-Basal region of the Cerebellum) RC would actually increase exceeding 125% after correction. These regions also had intensity values in the low-end of the dynamic range of the images, therefore, for the same intensity difference the observed error was higher for these structures. These structures correspond to the subset of point beyond the confidence interval in the upper-left area of Fig. 43 (right). In particular, the regions in the Cerebellum and the Vermis are located at the boundary with CSF, hence in a region with high intensity contrast, which led to over-correction of region intensities. This effect may also occur in larger structures but is counter-balanced by inner voxels of the ROI being less affected by the sharpening of boundaries intensity contrast after correction.

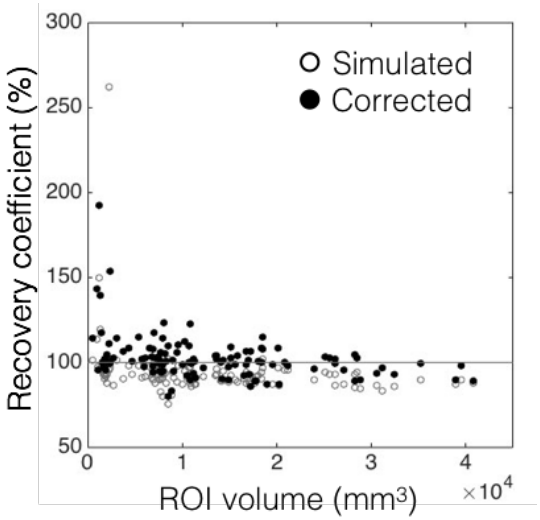

Figure 44. Recovery coefficient vs volume for each region of interest (ROI) of the AAL atlas for simulated 18F-FDG PET data (circle) and corrected (filled circle) with SPM's T1 single-subject image.

5.3.3. Clinical data

Axial 2D views of MR and corrected PET image pairs of the RIRE patient are shown in Fig. 44. Although similar resolution recovery was observed for the three MR modalities, shaper images were observed after T2 correction, and followed by T1 and PD correction. Such recovery was remarkably pronounced in the margins of the lesion located at the right and frontal area of the images. All corrections preserved the original image hypointensity in the lesion region and an increased lesion-to-no lesion intensity contrast irrespective of the intensity values of the MR images (Fig. 45 - columns 1,2). However, hot spots were observed in the CSF of T2 corrected images that where no glucose consumption takes place and were, therefore, absent in the original image. A small registration misalignment was observed in Fig. 45 (g-5) with non-visible effect in the remaining axial planes.

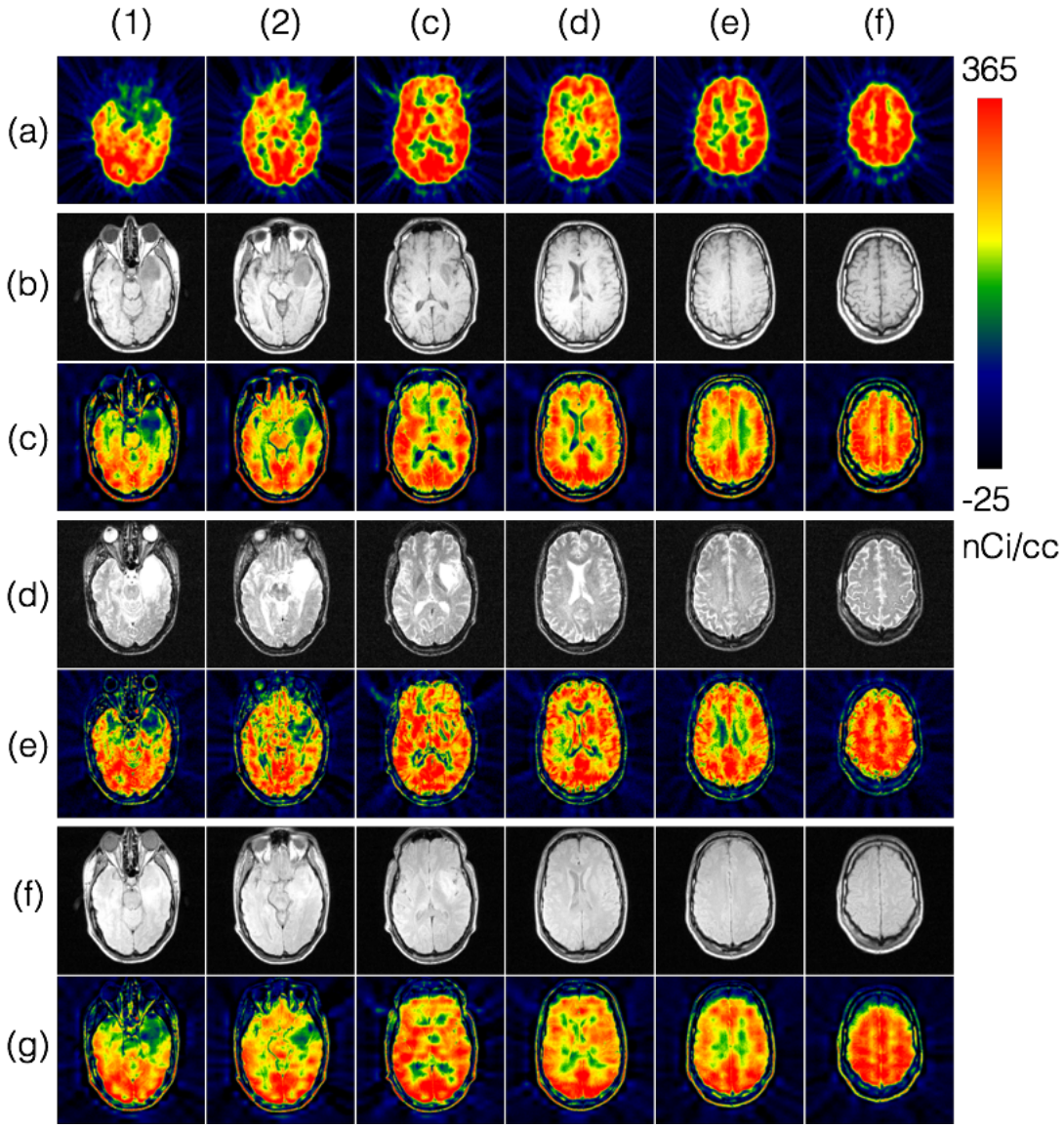

Figure 45. 2D planes of (a) 18F-FDG PET, (b) T1, (c) T1-corrected PET, (d) T2, (e) T2-corrected PET, (f) PD, and (g) PD-corrected PET images.

Resolution recovery was also apparent in intensity profile plots of frontal and occipital sections of the brain (Fig. 46). As observed in the plots, large regions affected little by PVE but not so little by noise had lower but homogeneus values after correction. In addition, smaller regions affected by both spill-out and spill-in effects (Fig. 46, arrows) recovered intensity values after correction that exceeded original intensity values. These effects were more remarkable in T2 corrected images. Besides, cranium intensities are much less pronounced in T2 images (Fig. 45d) than in T1 or PD images (Fig. 45b,f) and, consequently, have a neglible effect in brain activity correction, as observed in the two intensity peaks located around 4.7 and 18.8 cm in the profile plots (Fig. 46).

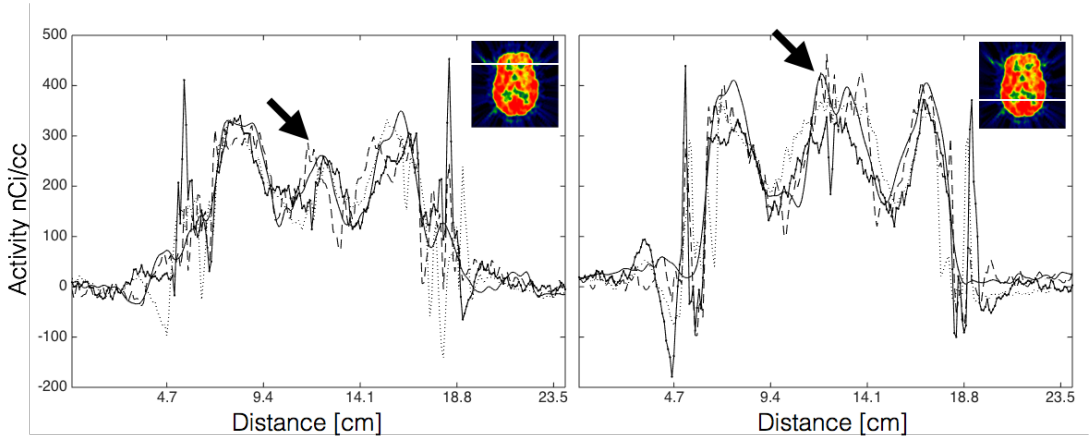

Figure 46. Intensity profiles of clinical 18F-FDG images (corresponding to third PET image in Fig. 41) in frontal (left) and temporal (right) regions: plots show original PET (solid line), T1-corrected (dot-dashed line), T2-corrected (dashed line), and PD-corrected (dotted line) images.

5.4. Discussion

Partial volume effect in PET imaging poses still today a limitation to accurate clinical diagnosis, treatment follow-up, and quantitative analysis of new research applications. Recent mutual multiresolution (MMA) approaches depart from previous PVE correction methods highly based on manual interaction and that do not produce a resolution-recovered image. MMA uses structural information absent in the functional image but present in the imaged object to correct for PVE.

In this Thesis, a novel PVE correction method was presented that is based on an energy multiresolution analysis and the energy equalization of the decomposed sub-bands. Understanding a PVE-free high-resolution PET image as a functional image with the spatial resolution of an anatomical image, e.g. an MRI, correction is accomplished by matching the energy balance between low and high frequency bands in the functional image to that of its anatomical image counterpart. In addition and besides correction, resolution recovery is also accomplished by replacing sub-bands in the functional image with low energy, i.e. of little relevance, with the analogous sub-bands in the anatomical image. As a result, the method is completely parameter independent overcoming the implementation limitations of other recent MMA methods also relying on accurate registration of functional and anatomical images. Distinctly, the method does not require any *a priori* information of the FWHM of the scanner, segmentation of the anatomical image, or thresholds of any kind.

The method produced robust results for phantom, SPM single-subject T1 template, and clinical T1, T2 and PD MR image modalities used to correct for PVE in simulated or clinical PET images. Phantom data showed almost perfect recovery coefficients and intensity variability after correction (Table 9) comparable to those

presented in (Le Pogam et al. 2011; Boussion et al. 2005; Shidahara et al. 2009). As observed in (Le Pogam et al. 2011) when the voxel dimensions of the simulated image matched those of the true phantom image, even the original intensities of the smallest regions most affected by PVE could be practically restored. However, these results were not reproduced in small-volume low-intensity regions of the simulated 18F-FDG PET data. Such regions were insensitive to correction and were observed as outliers in the Bland-Altman and RC plot (Figs. 43-44). Consequently, the method underperformed in those small-volume regions where the intensity contrast was reduced or when the global contrast of the anatomical image was poor. In Figs. 45-46 the lower contrast of PD data showed less recovery than T1 and, particularly, T2 images, a limitation that is implicit in MMA methods as pointed in (Le Pogam et al. 2011; Boussion et al. 2005; Shidahara et al. 2009). Nonetheless, when larger structures are considered, the global performance of the method is satisfactory with main tissues recovery coefficient errors below 10% for the 18F-FDG PET simulated data (Table 10). Remarkably, the method achieved reduction of WM intensities and significant reduction of CSF, both regions being commonly affected by spill-in effects (Boussion et al. 2005). Again, the amount of intensity recovery for gray and white matter, and CSF varied due to the different structural information associated to each tissue in the anatomical image, in this case the SPM single-subject T1 template.

Although a noise analysis was outside the scope of this work, significant reduction of PET noise was observed in the corrected images, with a more noticeable effect in background regions of simulated and clinical data (Fig. 42,45) but also in the spheres of the phantom data (Fig. 41). This is explained by the replacement of sub-bands in the PET image with sub-bands from the anatomical image, commonly with less noise. Notice that approaches working at a local level (Le Pogam et al. 2011; Shidahara et al. 2009) address noise by means of thresholding wavelet coefficients, a less robust strategy. However, local methods prevent the integration of uncorrelated structural information into the functional image after correction, such as the eyes or the cranium observed in Figs. 42,45. While the presence of uncorrelated anatomical information in the corrected image may question the reliability of the method in those regions, the relevance of such artefacts should also be considered within the clinical context. Therefore, the clinical interpretation of brain tissue in 18F-FDG PET corrected images in Fig. 45 should not be altered by the undue presence of the cranium and the edges of the eyes balls.

Future work should be focused on overcoming the main limitations of MMA methods. On one side, the dependency of high intensity contrast of small structures for effective correction is essential but non-ubiquitous in the image. Contrast enhancement methods that provide sufficient structural information should be incorporated in a controlled and grounded manner. On the other side, novel approaches to remove uncorrelated structural information should be devised. Different implementations are described in (Le Pogam et al. 2011; Shidahara et al. 2009) that rely on thresholding approaches and that are based on functional-to-

anatomical intensity ratios. Alternatively, information-based local or global approaches used in conjunction with the energy-based criterion may provide more robust and effective results. Further validation of this and other recent MMA methods is also necessary since the potential of these approaches is still to be discovered in a field of medical image processing with currently no widely applicable gold standard method.

5.3. Conclusions

A novel energy multiresolution for PVE correction and resolution recovery has been presented that is parameter independent and performs robustly when T1, T2 and PD MR images are used for correction of 18F-FDG PET images. The method uses an energy criterion to integrate structural information of a registered anatomical image into the PET image and equalizes the energy of low and high frequency sub-bands to match that of the anatomical image.

6. Conclusions

In this Thesis three novel methods have been developed and validated to address current registration challenges in medical imaging particularly affecting but not limited to small-animal images of the brain. The core innovation of this work resides on the exploitation of the shared information between images and has led to the main following contributions:

1. A novel information-based overlap-invariant registration method (SMI) that includes the non-overlapping images field of view (FOV) into the registration cost function as essential information of the degree of misalignment between the images. The method produces smoothly-convergent cost functions that result in a dramatically increased capture range of the gold standard registration method both for multimodal human and mice brain datasets and varying FOV.
2. A novel iterative mice brain MR intensity inhomogeneity (IIH) correction-registration strategy (IRIS) that unifies the correction and registration cost function in an optimization framework to achieve more accurate IIH corrections, registrations and quantifications than reference approaches. The method relies on maximization of intensity correspondences between images both in the correction and registration stages. When SMI is integrated in IRIS, registration success rate increases from 40-50% to practically 100%, leading to improved IIH correction and quantification as compared to reference methods.
3. A novel Energy-based Multiresolution Approach using wavelets for correction of the partial volume effect (PVE) inherent in PET images. The method is completely image-based and parameter-independent. It incorporates the anatomical information of structural images, e.g. MRI, to correct for spill over effects in an accurately registered PET image pair. Anatomical information is automatically selected according to its energy contribution or relevance with respect to the functional information conveyed in the PET image. PVE-correction and resolution-recovery is obtained through energy equalization of wavelet sub-bands in the PET image to preserve the energy balance between low and high frequency wavelet sub-bands of the anatomical image. The method was tested with a broad range of MRI modalities as compared to similar studies.

7. Future work

The impact of the methods and results presented in this Thesis depends on the robustness of the approaches to perform similarly with larger datasets, in a broader application range, and on the effective diffusion of such results and methods. To this purpose, future lines of action involve:

- Publication of current results derived from the iterative IIH correction-registration strategy and the PVE-correction and resolution-recovery method presented in this Thesis. (The results derived from the registration method SMI are currently under review in the Computer Methods and Programs in Biomedicine Journal).
- Open-source distribution of the SMI registration method as, for example, part of the SPM package, a widely-used software for the processing and analysis of human brain images. Including SMI in SPM or other open access and publicly known packages alike may escalate the use of the method and benefit research institutions globally. The research groups leading such platforms are accessible through email.
- The iterative IIH correction-registration strategy was validated with a real dataset including 12 18F-FDG PET and T2-weighted MR image pairs. It is suggested that a further validation be done with a larger sample and including other MR modalities and PET biomarkers that reinforce previous results of the IRIS-SMI combination. The breadth and robustness of such results may lead to a high impact factor publication. Our group has access to several research laboratories with small-animal imaging facilities and datasets that are appropriate to achieve this objective.
- The Energy-based Multiresolution PVE-correction method was validated with several MRI modalities but only one PET radiotracer, i.e. 18F-FDG. Further validation of several PET radiotracers will be useful to assess the robustness of the method to different biomarkers distributions. The performance of the method depends on the intensity contrast of the anatomical image. For this reason, CT images are hardly the best candidates for PVE correction with wavelet-based multiresolution approaches. However, CT imaging is an essential tool for cancer diagnosis and treatment monitoring and it is of utmost interest to adapt the method so that it can robustly perform also with CT images. Post-processing strategies that increase the intensity contrast of the image may be a possible line of research.

8. Own publications

Xavier Jimenez, Shiva K. Shukla, Isabel Ortega, Francisco J. Illana, Carlos Castro-González, Berta Marti-Fuster, Ian Butterworth, Manuel Arroyo, Brian Anthony, Luis Elvira. **Quantification Of Very Low Concentrations Of Leukocyte Suspensions In Vitro By High-Frequency Ultrasound.** Journal of Ultrasound in Medicine and Biology. January 2016.

John H. Lee, **Xavier Jimenez**, Ian R. Butterworth, Carlos Castro-González, Shiva K. Shukla, Berta Marti-Fuster, Luis Elvira, Duane S. Boning, Brian W. Anthony. **Ultrasound Image-based Absolute Concentration Measurement Technique for Materials with Low Scatterer Concentration.** IEEE International Ultrasonics Symposium. October 2015.

John H. Lee, **Xavier Jimenez**, Xiang Zhang, Duane S. Boning, Brian W. Anthony. **Measurement of Very Low Concentration of Microparticles in Fluid by Single Particle Detection using Acoustic Radiation Force Induced Particle Motion.** IEEE International Ultrasonics Symposium. October 2015.

Jimenez X., Figureiras F., Marques F., Salembier P., Herance R., Rojas S., Millán O., Pareto D., Gispert JD. **Registration of multi-modal neuroimaging datasets by considering the non-overlapping field of view into the NMI calculation.** ISBI (International Symposium on Biomedical Imaging). May 2012.

Hoekzema E, Rojas S, Herance R, Pareto D, Abad S, **Jimenez X**, Figueiras FP, Popota F, Ruiz A, Flotats N, Fernández FJ, Rocha M, Rovira M, Víctor VM, Gispert JD. **[(11)C]-DASB microPET imaging in the aged rat: frontal and meso-thalamic increases in serotonin transporter binding.** Experimental Gerontology. December 2011.

Herance R, Rojas S, Abad S, **Jimenez X**, Gispert JD, Millán O, Martín-García E, Burokas A, Serra MÀ, Maldonado R, Pareto D. **Positron Emission Tomographic Imaging of the Cannabinoid Type 1 Receptor System with [11C]omar ([11C]jhu75528): Improvements in Image Quantification Using Wild-type and Knockout Mice.** Molecular Imaging. December 2011.

Laura Igual, Joan Soliva, Antonio Hernández-Vela, Sergio Escalera, **Xavier Jimenez**, Oscar Vilarroya, Petia Radeva. **A fully-automatic caudate nucleus segmentation of brain MRI: Application in volumetric analysis of pediatric attention-deficit/hyperactivity disorder.** Biomedical Engineering Online. October 2011.

Figueiras FP, **Jimenez X**, Pareto D, Gómez V, Llop J, Herance R, Rojas S, Gispert JD. **Simultaneous dual-tracer PET imaging of the rat brain and its application in the study of cerebral ischemia.** Molecular Imaging and Biology. June 2011.

Herance R, Rojas S, Abad S, **Jimenez X**, Gispert JD, Millán O, Martín-García E, Burokas A, Serra MA, Maldonado R, Pareto D. **Positron Emission Tomographic Imaging of the Cannabinoid Type 1 Receptor System with [(11)C]OMAR ([(11)C]JHU75528): Improvements in Image Quantification Using Wild-Type and Knockout Mice.** Molecular Imaging. April 2011.

Hoekzema E, Rojas S, Herance R, Pareto D, Abad S, **Jimenez X**, Figueiras FP, Popota F, Ruiz A, Flotats N, Fernández FJ, Rocha M, Rovira M, Víctor VM, Gispert JD. **In vivo molecular imaging of the GABA/benzodiazepine receptor complex in the aged rat brain.** Neurobiology of Aging. April 2011.

Hoekzema E, Herance R, Rojas S, Pareto D, Abad S, **Jimenez X**, Figueiras FP, Popota F, Ruiz A, Torrent È, Fernández-Soriano FJ, Rocha M, Rovira M, Víctor VM, Gispert JD. **The effects of aging on dopaminergic neurotransmission: a microPET study of [11C]-raclopride binding in the aged rodent brain.** Neuroscience. December 2011.

Francisca P. Figueiras, **Xavier Jimenez**, Deborah Pareto, Juan D. Gispert. **Partial Volume Correction using an Energy Multiresolution Analysis.** IEEE Nuclear Science Symposium Conference Record. May 2009.

9. References

Aarun, K.S., Huang, T.S. & Blostein, S.D., 1987. Least-squares fitting of two 3D-point sets. *IEEE Transactions on Pattern Analysis and Machine Intelligence*, 9, pp.698–700.

Alfano, B. et al., 2004. A new method for voxel-based partial volume effect correction. In *Human brain mapping*. p. TH360.

Andersen, F.L. et al., 2013. Clinical evaluation of PET image reconstruction using a spatial resolution model. *European Journal of Radiology*, 82(5), pp.862–9.

Arata, L. et al., 1995. Three-dimensional anatomical model-based segmentation of MR brain images through Principal Axes Registration. *IEEE Transactions on Biomedical Engineering*, 42(11), pp.1069–78.

Ashburner, J., 2012. SPM: A history. *NeuroImage*, 62(2), pp.791–800.

Ashburner, J. & Friston, K.J., 2005. Unified segmentation. *NeuroImage*, 26(3), pp.839–51.

Axel, L., Constantini, J. & Listerud, J., 1987. Intensity correction in surface coil MR imaging. *American Journal of Radiology*, 148, pp.418–420.

Ballesteros-Zebadua, P. et al., 2016. Assessment of an image-guided neurosurgery system using a head phantom. *British journal of neurosurgery*, pp.1–5.

Bansal, R., Staib, L.H. & Peterson, B.S., 2004. Correcting nonuniformities in MRI intensities using entropy minimization based on an elastic model. In *Medical image computing and computer-assisted intervention*. pp. 78–86.

Barbosa, F.G., von Schulthess, G. & Veit-Haibach, P., 2015. Workflow in Simultaneous PET/MRI. *Seminars in nuclear medicine*, 45(4), pp.332–44.

Belaroussi, B. et al., 2006. Intensity non- uniformity correction in MRI: existing methods and their validation. *Medical Image Analysis*, 10(2), pp.34–46.

Besl, P.J. & McKay, N.D., 1992. A method for registration of 3-D shapes. *IEEE Transactions on Pattern Analysis and Machine Intelligence*, 14, pp.239–256.

Boussion, N. et al., 2005. Generating resolution-enhanced images for correction of partial volume effects in emission tomography: A multiresolution approach. *Physics in Medicine and Biology*, 4, pp.2423–2427.

Bowen, S.L. et al., 2013. Influence of the partial volume correction method on (18)F-fluorodeoxyglucose brain kinetic modelling from dynamic PET images reconstructed with resolution model based OSEM. *Physics in Medicine and Biology*, 58(20), pp.7081–106.

Brent, R.P., 1973. Powell's algorithm. In *Algorithms for minimization without derivatives.2025*

Brown, L.G., 1992. A survey of image registration techniques. *ACM Computing Surveys*, 24(4), pp.325–376.

Budiharto, T. et al., 2009. A semi-automated 2D/3D marker-based registration algorithm modelling prostate shrinkage during radiotherapy for prostate cancer. *Radiotherapy and Oncology*, 90(3), pp.331 – 336.

Carson, R.E., 1986. A maximum likelihood method for region-of- interest evaluation in emission tomography. *Journal Of Computer Assisted Tomography*, 10(4), pp.654–63.

Carvalho, D.D.B. et al., 2014. Joint intensity-and-point based registration of free-hand B-mode ultrasound and MRI of the carotid artery. *Medical physics*, 41(5), p.52904.

Casteels, C. et al., 2006. Construction and Evaluation of Multitracer Small-Animal PET Probabilistic Atlases for Voxel-Based Functional Mapping of the Rat Brain. *Sante*, 47(11), pp.1858–1866.

Catana, C. et al., 2008. Simultaneous in vivo positron emission tomography and magnetic resonance imaging. *Proceedings of the National Academy of Sciences of the United States of America*, 105(10), pp.3705–3710.

Chang, H. & Fitzpatrick, J.M., 1992. A technique for accurate magnetic resonance imaging in the presence of field inhomogeneities. *IEEE transactions on medical imaging*, 11, pp.319–329.

Cizek, J. et al., 2004. Fast and robust registration of PET and MR images of human brain. *NeuroImage*, 22(1), pp.434–42.

Cocosco, C.A. et al., 1997. BrainWeb: ONline Interface to a 3D MRI Simulated Brain Database. *NeuroImage*, 5(4), p.S425.

Collignon, A. et al., 1995. Automated multi-modality image registration based on information theory. In Y. Bizais, C. Barillot, & R. Di Paola, eds. *Information processing in medical imaging*. Kluwer Academic Publishers, pp. 263–274.

Collins, C.M. et al., 2005. Central brightening due to constructive interference with, without, and despite dielectric resonance. *Journal of Magnetic Resonance Imaging*, 21(2), pp.192–196.

Collins, D. & Evans, A., 1997. ANIMAL: validation and applications of non-linear registration-based segmentation. *International Journal of Patter Recognition and Artificial Intelligence*, 11(8), pp.1271–1294.

Curiati, P.K. et al., 2011. Age-related metabolic profiles in cognitively healthy elders: results from a voxel-based [18F]fluorodeoxyglucose-positron-emission tomography study with partial volume effects correction. *American Journal of Neuroradiology*, 32(3), pp.560–5.

Daga, P. et al., 2014. Susceptibility artefact correction using dynamic graph cuts: application to neurosurgery. *Medical image analysis*, 18(7), pp.1132–1142.

Das, A. & Bhattacharya, M., 2010. Affine-based registration of CT and MR modality images of human brain using multiresolution approaches: comparative study on genetic algorithm and particle swarm optimization. *Neural Computing and Applications*, 20(2), pp.223–237.

Dawant, B.M., Zijdenbos, A.P. & Margolin, R.A., 1993. Correction of intensity variations in MR images for computer-aided tissue classification. *IEEE Trans. Med. Imag*, 12(4), pp.770–781.

Desco, M. et al., 2001. Multiresolution analysis in fMRI: sensitivity and specificity in the detection of brain activation. *Hum Brain Mapp*, 14(5), pp.16–27.

Desco, M. et al., 2005. ROC evaluation of statistical wavelet-based analysis of brain activation in [15O]-H2O PET scans. *NeuroImage*, 24(3), pp.763–70.

Dhawan, P. et al., 2002. Iterative principal axes registration method for analysis of MR-PET brain images. *IEEE Transactions on Biomedical Engineering*, 42(11), pp.1079 – 1087.

Dornheim, L., Tonnies, K. & Dixon, K., 2005. Automatic segmentation of the left ventricle in 3D SPECT data by registration with a dynamic anatomic model. In *roceedings of the 8th International Conference on Medical Image Computing and Computer Assisted Intervention – MICCAI*. pp. 335–342.

Erlandsson, K. et al., 2012. A review of partial volume correction techniques for emission tomography and their applications in neurology, cardiology and oncology. *Physics in Medicine and Biology*, 57(21), pp.R119–R159.

Faber, T.L. & Stokely, E.M., 1998. Orientation of 3-D structures in medical images. *IEEE Transactions on Pattern Analysis and Machine*, 10(5).

Farnia, P. et al., 2012. On the performance of improved ICP algorithms for registration of intra-ultrasound with pre-MR images; a phantom study. *Conference proceedings : ... Annual International Conference of the IEEE Engineering in Medicine and Biology Society. IEEE Engineering in Medicine and Biology Society. Annual Conference*, 2012, pp.4390–4393.

Fischl, B., 2013. FreeSurfer. Available at: http://freesurfer.net.

Fitzpatrick, J.M., 2006. Retrospective Image Registration Evaluation Project.

Fitzpatrick, J.M., 2010. The role of registration in accurate surgical guidance. *Proceedings of the Institution of Mechanical Engineers. Part H, Journal of engineering in medicine*, 224(5), pp.607–622.

Fitzpatrick, J.M., Hill, D.L.G. & Maurer, C.R., 2000. Image Registration. In J. M. Fitzpatrick & M. Sonka, eds. *Handbook of medical imaging*. SPIE press, pp. 447–514.

Fitzpatrick, J.M., West, J. & Maurer, C.R., 1998. Predicting error in rigid-body, point-based registration. *IEEE Transactions on Medical Imaging*, 17, pp.694–702.

Foskey, M. et al., 2005. Large deformation 3D image registration in image-guided radiation therapy. *Physics in Medicine and Biology*, 50(24), pp.5869–5892.

Fouquet, M. et al., 2014. Imaging brain effects of APOE4 in cognitively normal individuals across the lifespan. *Neuropsychology Review*, 24(3), pp.290–9.

Frangi, A., Laclaustra, M. & Lamata, P., 2003. A registration-based approach to quantify flow-mediated dilation (FMD) of the brachial artery in ultrasound image sequences. *IEEE Transactions on Medical Imaging*, 22(11), pp.1458–1469.

Freeborough, P. & Fox, N., 1998. Modeling brain deformations in alzheimer disease by fluid registration of serial 3D MR images. *Journal Of Computer Assisted Tomography*, 22(5), pp.838–843.

Friston, K. et al., 1995. Statistical Parametric Maps in Functional Imaging : A General Linear Approach. *Human Brain Mapping*, 2, pp.189–210.

Gan, R., Chung, A.C.S. & Liao, S., 2008. Maximum distance-gradient for robust image registration. *Medical Image Analysis*, 12(4), pp.452–468.

Ganser, K. et al., 2004. A deformable digital brain atlas system according to Talairach and Tournoux. *Medical image analysis*, 8, pp.3–22.

Gelman, N., Silavi, A. & Anazodo, U., 2014. A hybrid strategy for correcting geometric distortion in echo-planar images. *Magnetic resonance imaging*, 32(5), pp.590–593.

Gering, D. et al., 1999. An integrated visualization system for surgical planning and guidance using image fusion and interventional imaging. In *Proceedings of the International Conference on Medical Image Computing and Computer- Assisted Intervention - MICCAI*. pp. 809–819.

Gispert, J. et al., 2004. Method for bias field correction of brain T1-weighted magnetic resonance images minimizing segmentation error. *Hum. Brain Mapp.*, 22(2), pp.133–144.

Gispert, J.D. et al., 2003. Inhomogeneity correction of magnetic resonance images by minimization of intensity overlapping. In *International Conference of Image Processing*.

Greve, D.N. & Fischl, B., 2009. Accurate and robust brain image alignment using boundary-based registration. *NeuroImage*, 48(1), pp.63–72.

Grgic, A. et al., 2009. Nonrigid versus rigid registration of thoracic 18F-FDG PET and CT in patients with lung cancer: an intraindividual comparison of different breathing maneuvers. *Journal of nuclear medicine : official publication, Society of Nuclear Medicine*, 50(12), pp.1921–1926.

Guillemaud, R. & Brady, M., 1997. Estimating the bias field of MR images. *IEEE Trans. Med. Imaging*, 16(3), pp.238–251.

Habib, A. & Ai-Ruzouq, R., 2005. Semi-automatic registration of multi-source satellite imagery with varying geometric resolutions. *Photogrammetric Engineering and Remote Sensing*, 71(3), pp.325–332.

Hahn, D.A., Daum, V. & Hornegger, J., 2010. Automatic Parameter Selection for Multimodal Image Registration. *IEEE Transactions on Medical Imaging*, 29(5), pp.1140–1155.

Hauler, F. et al., 2016. Automatic quantification of multi-modal rigid registration accuracy using feature detectors. *Physics in medicine and biology*, 61(14), pp.5198–5214.

Hill, D.L.G. et al., 2001. Medical image registration. *Physics in Medicine and Biology*, 46, pp.R1–R45.

Hoffman, E.J., Huang, S.C. & Phelps, M.E., 1979. Quantitation in positron emission computed tomography: 1. Effect of object size. *Journal Of Computer Assisted Tomography*, 3(3), pp.299–308.

Hou, Z., 2006. A review on MR image intensity inhomogeneity correction. *International Journal of Biomedical Imaging (*, 49515, pp.1–11.

Huang, X. et al., 2009. Rapid dynamic image registration of the beating heart for diagnosis and surgical navigation. *IEEE Transactions on Medical Imaging*, 28(11), pp.1802 – 1814.

Hurvitz, A. & Joskowicz, L., 2008. Registration of a CT-like atlas to fluoroscopic X-ray images using intensity correspondences. *International Journal of Computer Assisted Radiology and Surgery*, 3, pp.493–504.

Ibanez, V. et al., 1998. Regional glucose metabolic abnormalities are not the result of atrophy in Alzheimer's disease. *Neurology*, 50(6), pp.1585–93.

Isgum, I. et al., 2009. Multi-atlas-based segmentation with local decision fusion – application to cardiac and aortic segmenta- tion in CT scans. *IEEE Transactions on Medical Imaging*, 28(7), pp.1000 – 1010.

Itou, T. et al., 2011. Multimodal image registration using IECC as the similarity measure. *Medical physics*, 38(2), pp.1103–1115.

Jenkinson, M. et al., 2012. FSL. *NeuroImage*, 62(2), pp.782–790.

Ji, S. et al., 2008. Mutual-information-based image to patient re-registration using intraoperative ultrasound in image-guided neurosurgery. *Medical Physics*, 35(10), pp.4612–4624.

Joshi, S. et al., 2004. Unbiased diffeomorphic atlas construction for computational anatomy. *NeuroImage*, 23, pp.S151–S160.

Judenhofer, M.S. et al., 2008. Simultaneous PET-MRI: a new approach for functional and morphological imaging. *Nature Medicine*, 14(4), pp.459–465.

Kim, E. et al., 2013. Partial volume correction using structural-functional synergistic resolution recovery: comparison with geometric transfer matrix method. *Journal of cerebral blood flow and metabolism : official journal of the International Society of Cerebral Blood Flow and Metabolism*, 33(6), pp.914–20.

King, A. et al., 2010. Registering preprocedure volumetric images with intraprocedure 3-D ultrasound using an ultrasound imaging model. *IEEE Transactions on Medical Imaging*, 29(3), pp.924 – 937.

Klein, S. et al., 2010. Elastix: a toolbox for intensity-based medical image registration. *IEEE Transactions on Medical Imaging*, 29(1), pp.196–205.

Knops, Z.F. et al., 2006. Normalized mutual information based registration using k-means clustering and shading correction. *Medical image analysis*, 10(3), pp.432–9.

Kruggel, F. et al., 2003. Analyzing the neocortical fine-structure. *Medical image analysis*, 7(3), pp.251–264.

Lavely, W. et al., 2004. Phantom validation of coregistration of PET and CT for image-guided radiotherapy. *Medical Physics*, 31(4), pp.1083 – 1092.

Ledesma-Carbayo, M. et al., 2005. Spatio-temporal nonrigid registration for ultrasound cardiac motion estimation. IEEE Trans Med Imaging. *IEEE Transactions on Medical Imaging*, 24(9), pp.1113–1126.

Leow, A. et al., 2006. Longitudinal stability of MRI for mapping brain change using tensor-based morphometry. *NeuroImage*, 31(2), pp.627–640.

Lewis, E.B. & Fox, N.C., 2004. Correction of differential intensity inhomogeneity in longitudinal MR images. *NeuroImage*, 23(1), pp.75–83.

Li, Q. et al., 2015. Cortical thickness estimation in longitudinal stroke studies: A comparison of 3 measurement methods. *NeuroImage: Clinical*, 8, pp.526–535.

Likar, B., Viergever, M. a & Pernus, F., 2001. Retrospective correction of MR intensity inhomogeneity by information minimization. *IEEE transactions on medical imaging*, 20(12), pp.1398–410.

Lim, K.O. & Pfefferbaum, A., 1989. Segmentation of MR brain images into cerebrospinal fluid spaces, white and gray matter. *Journal Of Computer Assisted Tomography*, 13, pp.588–593.

Lin, L. et al., 2013. Intensity inhomogeneity correction using N3 on mouse brain magnetic resonance microscopy. *Journal of neuroimaging : official journal of the American Society of Neuroimaging*, 23(4), pp.502–507.

Liu, J. & Tian, J., 2007. Registration of Brain MRI/PET Images Based on Adaptive Combination of Intensity and Gradient Field Mutual Information. *International Journal of Biomedical Imaging*, 2007, p.93479.

Liu, M. et al., 2015. View-centralized multi-atlas classification for Alzheimer's disease diagnosis. *Human Brain Mapping*, 36(5), pp.1847–65.

Ma, Y. et al., 2008. In vivo 3D digital atlas database of the adult C57BL/6J mouse brain by magnetic resonance microscopy. *Frontiers in Neuroanatomy*, 2, pp.1–10.

Maes, F. et al., 1997. Multimodality image registration by maximization of mutual information. *IEEE Transactions on Medical Imaging*, 16(2), pp.187–198. Available at: http://www.ncbi.nlm.nih.gov/pubmed/9101328.

Maes, F., Vandermeulen, D. & Suetens, P., 1999. Comparative evaluation of multiresolution optimization strategies for multimodality image registration by maximization of mutual information. *Medical Image Analysis*, 3(4), pp.373–386.

Maes, F., Vandermeulen, D. & Suetens, P., 2003. Medical image registration using mutual information. *Proceedings of the IEEE*, 91(10).

Maintz, J.B. & Viergever, M.A., 1998. A survey of medical image registration. *Medical Image Analysis*, 2(1), pp.1–36.

Mallat, S., 1999. *A wavelet tour of signal processing* Second. A. Press, ed., Elsevier.

Mallat, S.G., 1989. A theory for multiresolution signal decomposition: the wavelet representation. *IEEE Transactions on Pattern Analysis and Machine Intelligence*, 11(7), pp.674–693.

Malone, I.B. et al., 2013. MIRIAD-Public release of a multiple time point Alzheimer's MR imaging dataset. *NeuroImage*, 70, pp.33–36.

Mandava, V.R. et al., 1992. Registration of multimodal volume head images via attached markers. *Medical Imaging VI: Image Processing*, Proc. SPIE, pp.271–282.

Mangin, J.F., 2000. Entropy minimization for automatic correction of intensity nonuniformity. *IEEE Workshop on Mathematical Methods in Biomedical Image Analysis*, pp.162 – 169.

Manjón, J. V et al., 2007. A nonparametric MRI inhomogeneity correction method. *Medical image analysis*, 11(4), pp.336–45.

Marcinkowski, R. et al., 2016. Sub-millimetre DOI detector based on monolithic LYSO and digital SiPM for a dedicated small-animal PET system. *Physics in Medicine and Biology*, 61(5), pp.2196–2212.

Martin, S., Daanen, V. & Troccaz, J., 2008. Atlas-based prostate segmentation using an hybrid registration. *International Journal of Computer Assisted Radiology and Surgery*, 3, pp.485–492.

Maurer, C. et al., 1997. Registration of head volume images using implantable fiducial markers. *IEEE Transactions on Medical Imaging*, 16(4), pp.447–462.

Maurer, C.R. et al., 1996. Effect of geometrical distortion correction in MR on image registration accuracy. *Journal Of Computer Assisted Tomography*, 20, pp.666–679.

Maurer, C.R. et al., 1995. The accuracy of image-guided neurosurgery using implantable fiducial markers. *Computer Assisted Radiology*, pp.1197–1202.

Maurin, B. et al., 2009. A fast and automatic stereotactic registration with a single CT-slice. *Computer vision and image understanding*, 113(8), pp.878–890.

Meier, S. et al., 2016. Pathological Tau Promotes Neuronal Damage by Impairing Ribosomal Function and Decreasing Protein Synthesis. *The Journal of Neuroscience*, 36(3), pp.1001–7.

Meltzer, C.C. et al., 1990. Correction of PET data for partial volume effects in human cerebral cortex by MR imaging. *Journal Of Computer Assisted Tomography*, 14(4), pp.561–70.

Meltzer, C.C. et al., 1996. MR-based correction of brain PET measure- ments for heterogeneous gray matter radioactivity distribution. *Journal of cerebral blood flow and metabolism*, 16(4), pp.650–8.

Merlin, T. et al., 2015. A novel partial volume effects correction technique integrating deconvolution associated with denoising within an iterative PET image reconstruction. *Medical physics*, 42(2), pp.804–819.

Moore, S.C. et al., 2012. Improved regional activity quantitation in nuclear medicine using a new approach to correct for tissue partial volume and spill over effects. *IEEE Transactions on Medical Imaging*, 31(2), pp.405–16.

Van de Moortele, P.-F. et al., 2009. T1 weighted brain images at 7 Tesla unbiased for Proton Density, T2* contrast and RF coil receive B1 sensitivity with simultaneous vessel visualization. *NeuroImage*, 46(2), pp.432–46.

Mueller, S.G. et al., 2005. Ways toward an early diagnosis in Alzheimer's disease: The Alzheimer's Disease Neuroimaging Initiative (ADNI). *Alzheimer's & Dementia*, 1(1), pp.55–66.

Müller-Gärtner, H.W. et al., 1992. Measurement of radiotracer concentration in brain gray matter using positron emission tomography: MRI-based correction for partial volume effects. *Journal of cerebral blood flow and metabolism*, 14(4), pp.571–83.

Nelder, J. & Mead, R., 1965. A simplex method for function minimization. *Computer Journal*, 7, pp.308–313.

Oliveira, F.P. & Tavares, J.M.R., 2012. Medical image registration: a review. *Computer methods in biomechanics and biomedical engineering*, 17(2), pp.73–93.

Orlandini, L.C. et al., 2013. Improvement in clinical evaluation of PET/ CT images with high resolution algorithms. *Nuclear Medicine and Molecular Imaging*, 57(2), pp.201–6.

Pascau, J. et al., 2008. Automated method for small-animal PET image registration with intrinsic validation. *Molecular imaging and biology*, 11(2), pp.107–13.

Pascau, J., 2006. *Integración de imágenes biomédicas : técnicas basadas en teoría de la información*. E.T.S.I. Telecomunicación (UPM).

Peelle, J.E., Cusack, R. & Henson, R.N.A., 2012. Adjusting for global effects in voxel-based morphometry: gray matter decline in normal aging. *NeuroImage*, 60(2), pp.1503–1516.

Pelizzari, C.A. et al., 1989. Accurate three-dimensional registration of CT, PET, and/or MR images of the brain. *Journal Of Computer Assisted Tomography*, 13, pp.20–26.

Pieper, S., Halle, M. & Kikinis, R., 2004. 3D Slicer. In *Proceedings of the IEEE International Symposium on Biomedical Imaging: From Nano to Macro*. pp. 632–635.

Pluim, J.P.W., Maintz, J.B.A. & Viergever, M.A., 2004. F-information measures in medical image registration. M. Sonka & K. M. Hanson, eds. *IEEE Transactions on Medical Imaging*, 23(12), pp.1508–1516.

Le Pogam, A. et al., 2011. Evaluation of a 3D local multiresolution algorithm for the correction of partial volume effects in positron emission tomography. *Medical Physics*, 38(9), pp.4920–4933.

Popota, F.D. et al., 2009. Comparison of NEMA NU 4-2008 vs NEMA NU 2-2001 for the performance evaluation of the microPET R4 system. *2009 IEEE Nuclear Science Symposium Conference Record (NSS/MIC)*, pp.2706–2709.

Poulin, S. et al., 2011. Amygdala atrophy is prominent in early Alzheimer's disease and relates to symptom severity. *Journal of Psychiatric Research*, 194(1), pp.7–13.

Powell, M.J.D., 1994. An efficient method for finding the minimum of a function of several variables without calculating derivatives. *Computer Journal*, 7(2), pp.155–162.

Press, W. et al., 2007. *Numerical recipes: the art of scientific computing*., New York: Cambridge University Press.

Prieto, E. et al., 2013. Impact of time-of-flight and point-spread-function in SUV quantification for oncological PET. *Clinical Nuclear Medicine*, 38(2), pp.103–9.

Rangarajan, J.R. et al., 2011. Impact of RF inhomogeneity correction on image registration of micro MRI rodent brain images. In *IEEE International Symposium on Biomedical Imaging*. pp. 570 – 573.

Reilhac, A. et al., 2005. PET-SORTEO: validation and development of database of Simulated PET volumes. *IEEE Transactions on Nuclear Science*, 52(5), pp.1321–1328.

Reuter, M., Rosas, H.D. & Fischl, B., 2010. Highly accurate inverse consistent registration: a robust approach. *NeuroImage*, 53(4), pp.1181–1196.

Richardson, W.A., 1972. Bayesian-Based Iterative Method of Image Restoration. *Journal of the Optical Society of America*, 62(1), pp.55–59.

Riola-Parada, C. et al., 2016. Simultaneous PET/MRI vs PET/CT in oncology. A systematic review. *Revista espanola de medicina nuclear e imagen molecular*.

Rousset, O.G., Y, M., et al., 1998. Pixel-versus region-based partial volume correction in PET. In *Quantitative functional brain imaging with positron emission tomography*. pp. 67–75.

Rousset, O.G., Ma, Y. & Evans, A.C., 1998. Correction for partial volume effects in PET: principle and validation. *Journal of Nuclear Medicine*, 39(5), pp.904–11.

Rueckert, D., Frangi, A.F. & Schnabel, J.A., 2003. Automatic construction of 3-D statistical deformation models of the brain using nonrigid registration. *IEEE Transactions on Medical Imaging*, 22(8), pp.1014–25.

Rusu, M. et al., 2014. Prostatome: a combined anatomical and disease based MRI atlas of the prostate. *Medical physics*, 41(7), p.72301.

Salvado, O. & Wilson, D.L., 2007. Removal of local and biased global maxima in intensity-based registration. *Medical image analysis*, 11(2), pp.183–96.

Schaefferkoetter, J. et al., 2013. Clinical impact of time-of-flight and point response modeling in PET reconstructions: a lesion detection study. *Physics in Medicine and Biology*, 58(5), pp.1465–78.

Selesnick, I. & Li, K.L., 2003. Video denoising using 2D and 3D dual-tree complex wavelet transforms: Wavelet applications in signal and image processing. In *Proceedings of SPIE*. pp. 607–661.

Serrano-Pozo, A. et al., 2016. Plaque-Associated Local Toxicity Increases over the Clinical Course of Alzheimer Disease. *The American Journal of Pathology*, 186(2), pp.375–84.

Shannon, C.E., 1949. Communication in the presence of noise. *Proceedings of IEEE*, 37(1), pp.10–21.

Shidahara, M. et al., 2009. Functional and structural synergy for resolution recovery and partial volume correction in brain PET. *NeuroImage*, 44(2), pp.340–348.

Skerl, D., Likar, B. & Pernus, F., 2006. A protocol for evaluation of similarity measures for rigid registration. *IEEE Transactions on Medical Imaging*, 25(6), pp.779–791.

Sled, J.G. & Pike, G.B., 1998. Standing-Wave and RF Penetration Artifacts Caused by Elliptic Geometry: An Electrodynamic Analysis of MRI. *IEEE Transactions on Medical Imaging*, 17(4), pp.653–662.

Slomka, P.J. & Baum, R.P., 2009. Multimodality image registration with software: State-of-the-art. *European Journal of Nuclear Medicine and Molecular Imaging*, 36(SUPPL. 1), pp.44–55.

Slomka, P.J. & Baum, R.P., 2009. Multimodality image registration with software: state-of-the-art. *European journal of nuclear medicine and molecular imaging*, 36 Suppl 1, pp.S44–55.

Sosnovik, D.E. et al., 2007. Cardiac MRI in mice at 9.4 Tesla with a transmit-receive surface coil and a cardiac-tailored intensity-correction algorithm. *Journal of magnetic resonance imaging : JMRI*, 26(2), pp.279–87.

Staring, M. et al., 2009. Registration of cervical MRI using multifeature mutual information. *IEEE Transactions on Medical Imaging*, 28(9), pp.1412–1421.

Studholme, C., Hill, D. & Hawkes, D., 1999. An overlap invariant entropy measure of 3D medical image alignment . *Pattern Recognition*, 32(1), pp.71–86. Available at: http://discovery.ucl.ac.uk/157807/.

Studholme, C., Hill, D.L.G. & Hawkes, D.J., 1999. An overlap invariant entropy measure of 3D medical image alignment. *Pattern Recognition*, 32, pp.71–86.

Sureau, F.C. et al., 2008. Impact of image-space resolution modeling for studies with the high-resolution research tomography. *Journal of Nuclear Medicine*, 49(6), pp.1000–8.

Thacker, N., Lacey, A. & Bromiley, P., 2002. Validating MRI field homogeneity correction using image information measures. *In: British Machine Vision Conference (BMVC Õ02*, pp.626–635.

Tsao, J., 2003. *Interpolation artifacts in multimodality image registration based on maximization of mutual information*.,

Vandenberghe, S. et al., 2016. Recent developments in time-of-flight PET. *EJNMMI Physics*, 3(1), p.3.

Vaquero, J.J. et al., 2001. PET , CT , and MR Image Registration of the Rat Brain and Skull. *Brain*, 48(4), pp.1440–1445.

Vetterli, M. & Cormac, H., 1992. Wavelets and Filter Banks: Theory and Design. *IEEE Transactions on Signal Processing*, 40(9), pp.2207–2232.

Videen, T.O. et al., 1988. Regional correction of positron emission tomography data for the effects of cerebral atrophy. *Journal of cerebral blood flow and metabolism*, 8(5), pp.662–70.

Vovk, U., Pernu, F. & Likar, B.T., 2004. MRI intensity inhomogeneity correction by combining intensity and spatial information. *Physics in Medicine and Biology*, 49(17), pp.4119–4133.

Vovk, U., Pernus, F. & Likar, B., 2007. A review of methods for correction of intensity inhomogeneity in MRI. *IEEE transactions on medical imaging*, 26(3), pp.405–21.

Wang, J., Qiu, M. & Constable, R.T., 2005. In vivo method for correcting transmit/receive nonuniformities with phased array coils. *Magn. Reson. Med.*, 53, pp.666–674.

Wang, M.Y. et al., 1996. An automatic technique for finding and localizing externally attached markers in CT and MR volume images of the head. *IEEE Transactions on Biomedical Engineering*, 43, pp.627–637.

Wells, W.M. et al., 1996. *Multi-modal volume registration by maximization of mutual information*., Elsevier.

West, J., Fitzpatrick, J., et al., 1997. Comparison and evaluation of retrospective intermodality brain image registration techniques. *Journal Of Computer Assisted Tomography*, 21(4), pp.554–566.

West, J., Fitzpatrick, J.M., et al., 1997. Comparison and evaluation of retrospective intermodality brain image registration techniques. *Journal of computer assisted tomography*, 21(4), pp.554–66.

Woods, R.P., Cherry, S.R. & Mazziotta, J.C., 1992. Rapid automated algorithm for aligning and reslicing PET images. *Journal Of Computer Assisted Tomography*, 16, pp.620–633.

Wu, C., Aissaoui, I. & Jacquey, S., 1994. Algebraic analysis of the Van Cittert iterative method of deconvolution with a general relaxation factor. *Journal of the Optical Society of America*, 11(11), pp.2804–2808.

Wu, C., Murtha, P. & Jaramaz, B., 2009. Femur statistical atlas construction based on two-level 3D non-rigid registration. *Computer Aided Surgery*, 14(4), pp.83–89.

Wyawahare, M. V, Patil, P.M. & Abhyankar, H.K., 2009. Image Registration Techniques : An overview. *International Journal of Signal Processing, Image Processing and Pattern Recognition*, 2(3), pp.11–28.

Xiong, Z. & Zhang, Y., 2009. A novel interest point matching algorithm for remote sensing images. *IEEE Transactions on Geoscience and Remote Sensing*, 47(12), pp.4189–4199.

Yang, J. et al., 1996. Investigation of partial volume correction methods for brain FDG PET studies. *IEEE Transactions on Nuclear Science*, 43(6), pp.3322–3327.

Yokoi, T. et al., 2004. Accuracy and reproducibility of co-registration techniques based on mutual information and normalized mutual information for MRI and SPECT brain images. *Annals of nuclear medicine*, 18(8), pp.659–67.

Young Kim, E. & Johnson, H.J., 2013. Robust multi-site MR data processing: iterative optimization of bias correction, tissue classification, and registration. *Frontiers in neuroinformatics*, 7, p.29.

Zeeman, P., 1897. The Effect of Magnetisation on the Nature of Light Emitted by a Substance. *Nature*, 55, p.347.

Zhuang, X. et al., 2010. A registration-based propagation framework for automatic whole heart segmentation of cardiac MRI. *IEEE Transactions on Medical Imaging*, 29(9), pp.1612–1625.

Zitova, B., 2003. Image registration methods: a survey. *Image and Vision Computing*, 21(11), pp.977–1000.